Combining Aerosol Aging and Data Assimilation for Improving Volcanic Aerosol Forecast

Zur Erlangung des akademischen Grades eines
DOKTORS DER NATURWISSENSCHAFTEN (Dr. rer. nat.)
von der KIT-Fakultät für Physik des
Karlsruher Instituts für Technologie (KIT)

genehmigte

DISSERTATION

von

M.Sc. Lukas Ole Muser
aus Kirchheim unter Teck

Tag der mündlichen Prüfung:	11.02.2022
Referent:	Prof. Dr. Christoph Kottmeier
Korreferent:	Prof. Dr. Roland Potthast

Abstract

The Eyjafjallajökull eruption in Iceland 2010 impressively illustrated the consequences the dispersion of volcanic aerosol can have on international air traffic. More than 100,000 flights were canceled, as volcanic aerosol is hazardous for aircraft. Therefore, air traffic control and airlines are highly interested in reliable forecasts of volcanic aerosol dispersion after future eruptions. Numerical aerosol dispersion forecast is an initial value problem. This means that, first, the forecast needs to be initialized with an as exact as possible atmospheric state and composition. Second, the numerical model needs to account for all processes and feedback mechanisms that are relevant for volcanic aerosol transport.

In this thesis, I aim to improve volcanic aerosol dispersion forecast with En-Var data assimilation and by considering the aerosol–radiation interaction of internally mixed aerosol. Therefore, aerosol dynamic processes, such as coagulation, nucleation of sulfate particles, and condensation, are implemented into the ICON-ART (ICOsahedral Nonhydrostatic - Aerosols and Reactive Trace gases) model. These microphysical processes form internally mixed particles for which I also implement optical properties, allowing their interaction with solar and terrestrial radiation. Furthermore, an En-Var data assimilation method for volcanic aerosol is developed within the data assimilation framework of DWD (Deutscher Wetterdienst). This data assimilation method provides an estimate of the initial horizontal volcanic ash distribution. The new implementations are evaluated for the first four days after the Raikoke eruption 2019, which was one of the largest volcanic eruptions during the last 30 years.

Considering aerosol dynamic processes tends to increase the particle size which increases sedimentation. My results show that the sedimentation of large particles is responsible for the removal of about 50% of volcanic ash during the first 12 h after the Raikoke eruption. A main driver of this enhanced removal in my simulations is the coagulation of coarse ash particles with secondary volcanic aerosol, i.e., sulfate particles. The interaction of short and longwave radiation with internally mixed volcanic aerosol induces a lifting to some parts of the volcanic cloud. My results suggest that after the Raikoke eruption the volcanic aerosol cloud top rises about 3 km during the first 12 h and reaches a height of around 20 km after four days. The assimilation of observational data with the ART En-Var method has the potential to omit noise in the observational data.

The results of this thesis highlight the importance of aerosol dynamic processes and the interaction of aerosol with short and longwave radiation for operational volcanic aerosol dispersion forecast. Furthermore, the use of an ensemble based assimilation method for future volcanic aerosol dispersion forecasts can be advised.

Zusammenfassung

Der Ausbruch des Eyjafjallajökull in Island 2010 zeigte eindrucksvoll, welche Folgen ein Vulkanausbruch für den internationalen Luftverkehr haben kann. Mehr als 100.000 Flüge wurden gestrichen, da vulkanisches Aerosol eine Gefahr für Flugzeuge darstellt. Aus diesem Grund sind die Flugsicherung sowie Fluggesellschaften sehr an zuverlässigen Vorhersagen der Ausbreitung dieses Aerosols nach Vulkanausbrüchen interessiert. Die numerische Aerosolausbreitungsvorhersage ist ein klassisches Anfangswertproblem. Das bedeutet erstens, dass die Vorhersage mit einem möglichst genauen atmosphärischen Zustand sowie deren Zusammensetzung initialisiert werden muss. Zweitens muss das numerische Modell alle Prozesse und Rückkopplungsmechanismen berücksichtigen, welche für den Transport vulkanischer Aerosole relevant sind.

Im Rahmen dieser Arbeit möchte ich die Ausbreitungsvorhersage vulkanischer Aerosole mit Hilfe einer En-Var Datenassimilation sowie durch die Berücksichtigung der Aerosol–Strahlung–Wechselwirkung von intern gemischtem Aerosol verbessern. Hierfür werden in das ICON-ART (ICOsahedral Nonhydrostatic - Aerosols and Reactive Trace gases) Modell aerosol–dynamische Prozesse wie die Koagulation, die Nukleation von Sulfatpartikeln und der Kondensation von gasförmigen Komponenten auf Aerosolpartikel implementiert. Diese mikrophysikalischen Prozesse bilden intern gemischte Partikel. Für diese intern gemischten Partikel bestimme ich optische Eigenschaften, welche eine Interaktion mit kurz- und langwelliger Strahlung ermöglichen. Darüber hinaus wird eine En-Var-Datenassimilationsmethode für vulkanisches Aerosol innerhalb der Datenassimilationsumgebung des DWD (Deutscher Wetterdienst) entwickelt. Die Datenassimilation liefert eine Schätzung des anfänglichen Zustands sowie der Zusammensetzung der Atmosphäre. Diese Neuentwicklungen werden für die ersten vier Tage nach dem Raikoke–Ausbruch 2019, einem der größten Vulkanausbrüche der vergangenen 30 Jahre, ausgewertet.

Die Berücksichtigung aerosol–dynamischer Prozesse führt zu einer Zunahme der Partikelgröße, was deren Sedimentationsgeschwindigkeit erhöht. Meine Ergebnisse zeigen, dass die Sedimentation großer Partikel für die Beseitigung von etwa 50% der Vulkanasche während der ersten 12 h nach dem Ausbruch des Raikoke verantwortlich ist. In meinen Simulationen ist die Koagulation von grobkörnigen (coarse mode) Aschepartikeln mit sekundärem vulkanischem Aerosol, d.h. Sulfatpartikeln, eine der Hauptursachen für diese hohe Abnahme. Die Wechselwirkung von kurz- und langwelliger Strahlung mit intern gemischtem vulkanischem Aerosol führt zu einem Anheben von Teilen der Wolke aus vulkanischen Aerosolen. Meine Ergebnisse deuten darauf hin, dass die Wolkenoberseite des vulkanischen Aerosols nach dem Ausbruch des Raikoke während der ersten 12 h etwa 3 km angehoben wird und nach vier Tagen eine

Höhe von etwa 20 km erreicht. Die Assimilation von Beobachtungsdaten mit der ART En-Var-Methode kann Rauschen in den Beobachtungsdaten herausfiltern.
Die Ergebnisse dieser Arbeit verdeutlichen die Bedeutung der aerosol–dynamischen Prozesse sowie der Wechselwirkung von Aerosolen mit kurz- und langwelliger Strahlung für die operationelle Ausbreitungsvorhersage vulkanischer Aerosole. Darüber hinaus kann die Verwendung einer ensemblebasierten Assimilationsmethode für zukünftige Ausbreitungsvorhersagen vulkanischer Aerosole empfohlen werden.

Contents

1. Introduction

In 2010, the Eyjafjallajökull volcano erupted in Iceland. The eruption lasted for 39 days during April and May with periods of higher and lower activity (Gudmundsson et al., 2012). During the initial phase of the eruption in April 2010, northwesterly winds transported the emitted volcanic ash towards central Europe. As a consequence, large areas of European airspace were closed for eight days from 15 through 22 April (as reported by EUROCONTROL[1]). The closure led to the cancellation of 100,000 flights (Schumann et al., 2011). These eight days in April resulted in a loss of approximately US$2.2 billion for the aviation sector alone (Oxford Economics, 2010) and led to further disruptions in global economy (Mazzocchi et al., 2010; Budd et al., 2011). Similar events can occur also at different volcanoes anytime again.

Since the onset of civil aviation, aircraft encountered volcanic clouds several times, which partially resulted in near accidents. Most reported encounters of aircraft with volcanic clouds occurred at a distance < 1000 km to the volcano or within 24 h after the eruption (Guffanti et al., 2010). Especially after the eruption of Mount Galunggung in 1982 and the eruption of Redoubt Volcano in 1989, volcanic ash became widely recognized as a hazard to aircraft (Guffanti et al., 2010). Volcanic clouds usually contain solid volcanic ash particles and secondary volcanic aerosol. Volcanic ash consists of tephra particles with diameters < 2 mm (Rose and Durant, 2009). Secondary volcanic aerosol are usually sulfate droplets that form from volcanic SO_2 through chemical and microphysical processes (Tabazadeh and Turco, 1993; Textor et al., 2004; Durant et al., 2010). Both can be hazardous for aircraft.

Jet engines are the most vulnerable parts affected by volcanic ash. Temperatures in modern days jet engines are high enough to melt volcanic ash particles. The molten particles can deposit on turbine components and eventually block the air flow through the engine (Casadevall, 1994; Casadevall et al., 1996). Reports on damages to other aircraft components exist as well, e.g., fogging of wind-screens, erosion of antenna surfaces, and plugging of the pitot static system (Casadevall, 1994).

Besides volcanic ash, sulfate compounds that form out of volcanic precursor gases can also damage aircraft components (Carn et al., 2008; Schmidt et al., 2014). Eliaz et al. (2002) report an increased corrosion of compressor blades in jet engines due to sulfate particles. Furthermore, sulfuric acid enhances windshield crazing (Bernard and Rose, 1990).

Airlines not only try to avoid volcanic clouds due to the potential risk of fatal damage, but also as the impact of volcanic aerosol on aircraft components shortens necessary maintenance intervals and increases maintenance costs. Due to these hazards, a strict zero tolerance criterion was in place (Cantor, 1998). Zero tolerance means, if volcanic ash was forecasted or observed somewhere the corresponding airspace

[1] European Organisation for the Safety of Air Navigation

was closed. Only since the aftermath of the Eyjafjallajökull eruption in 2010, threshold ash concentrations of 2 and 4 mg m^{-3} were defined to separate areas of low, medium, and high contamination (EASA SIB No.: 2010-17R7, 2015; Beckett et al., 2020). This new regulation is designed to prevent large-scale airspace closures in the future. However, airlines and air traffic control now rely on a quantitative, timely, correct, and reliable volcanic aerosol forecast even more than before.

The spatial and temporal distribution of volcanic aerosol in the atmosphere is not only of interest for air traffic safety. These aerosols can also have a long lasting climatic effect and influence weather (Robock, 2000; Schmincke, 2004; Mather, 2008). The connection between volcanic eruptions and weather and climate has already been suspected in the 18th century (Schmincke, 2004). Today it is known that the interaction of volcanic aerosol with solar and terrestrial radiation should be considered in climate models (Andersson et al., 2015). Similarly, on shorter time scales, i.e., in numerical weather prediction models, volcanic aerosol can play a role by changing the radiation budget of the atmosphere (Hirtl et al., 2019).

The previous examples highlight the need to adequately represent volcanic aerosol in simulations at different spatial and temporal scales. In the scope of this work, short time scales, in the order of few days after volcanic eruptions are of particular interest. Results of such simulations are especially important for volcanic aerosol dispersion forecasts for air traffic safety and can be of interest for numerical weather prediction. Furthermore, understanding the underlying physical processes of volcanic aerosol dispersion during this initial phase after an eruption, can also improve the representation of volcanic aerosols in climate models (Niemeier et al., 2009).

With this thesis, I aim to improve volcanic aerosol dispersion forecast. In general, numerical aerosol dispersion forecasting is an initial value problem. Hence, there are two requirements for a correct and reliable forecast. First, the forecast simulation must be initialized with an as exact as possible atmospheric state and composition at time t_0. As the true atmospheric state is generally not known at every model grid point, the initial atmospheric state and composition at t_0 can only be an estimation. Second, an accurate model is needed in which all relevant processes and feedback mechanisms are represented. In the following, I present the current state of (volcanic) aerosol dispersion models as well as methods for the determination of the best possible initial condition.

1.1. Current State of Volcanic Aerosol Dispersion Forecast

First numerical models, capable of simulating the dispersion of volcanic aerosol, evolved in the 1980s. They were inspired by the Mount St. Helens eruption of 1980 (Hopkins and Bridgman, 1985; Armienti et al., 1988). During the Mount Galunggung eruption in 1982 and the eruption of Redoubt Volcano in 1989 two aircraft encountered the volcanic ash cloud, which resulted in a temporary loss of all engines (Guffanti et al., 2010). As a response to these two near catastrophic encounters the Volcanic Ash Advisory Centers (VAAC) were established in the 1990s. There are a total of nine VAACs globally. Each

one is responsible to monitor volcanoes in a specific geographic region. In case of an eruption, the responsible VAAC delivers volcanic aerosol dispersion forecasts operationally.
The London VAAC is associated with the Meteorological Office of the United Kingdom (UK Met Office) and issues advisories on the Icelandic volcanoes. For this reason, it has certain importance for German and central European airspace. Details on its volcanic ash dispersion forecasting system are given in the following. It should be noted that the German meteorological service *Deutscher Wetterdienst* (DWD) and the VAAC in Toulouse are also of relevance for air traffic safety over Germany. The DWD issues advisories for *Deutsche Flugsicherung*, the German air traffic control, in addition to the advisories issued by the responsible VAAC. The Toulouse VAAC monitors volcanoes in Africa and most of Europe.
A comprehensive overview on the current state of the volcanic aerosol dispersion forecasting system at London VAAC is given by Beckett et al. (2020). The London VAAC uses the NAME (Numerical Atmospheric-Dispersion Modelling Environment) model for its atmospheric dispersion forecast (Jones et al., 2007). The model is developed by the UK Met Office. It is a Lagrangian particle trajectory model. Furthermore, it is an offline dispersion model which means that it is decoupled from the atmospheric dynamics. The transport of particles is only driven by pre-calculated meteorological fields. In an offline dispersion model, no feedback from aerosol–radiation interaction on meteorological variables is possible, e.g., on temperature or cloud properties. Nevertheless, this offline particle trajectory approach is pursued in many models for volcanic aerosol dispersion forecast. For example, the U.S. National Oceanic and Atmospheric Administration (NOAA) runs the HYSPLIT (Hybrid Single-Particle Lagrangian Integrated Trajectory) model (Stein et al., 2015). Another well know Lagrangian aerosol dispersion model is the FLEXPART (FLEXible PARTicle dispersion model) model (Stohl et al., 1998; Pisso et al., 2019). Similarly, the French meteorological service *Météo–France* develops and uses the offline MOCAGE (Modèle de Chimie Atmosphérique à Grande Echelle) model (Sič et al., 2015), which is operational at Toulouse VAAC.
Another type of aerosol dispersion models are Eulerian models. They are usually online coupled to the underlying atmospheric model. That means, the aerosol and gas transport is computed together with the atmospheric variables. Hence, the feedback of aerosol or gas processes can change the atmospheric state. Examples are the NMMB/MONARCH (Marti et al., 2017), WRF-Chem (Weather Research and Forecasting – Chemistry; Grell et al., 2005; Skamarock et al., 2008), and ICON-ART (more details in Sect. 3; Zängl et al., 2015; Rieger et al., 2015).
Any aerosol dispersion model relies on an adequate representation of all relevant processes. Figure 1.1 illustrates these processes for volcanic aerosol dispersion simulations.

Emission

A crucial process is the emission of volcanic aerosol and gases. Without the correct emission rate and height of particle or gas release, volcanic aerosol dispersion forecast cannot succeed. Extensive research on the representation of eruption source parameters in models has been done (e.g. Mastin et al., 2009;

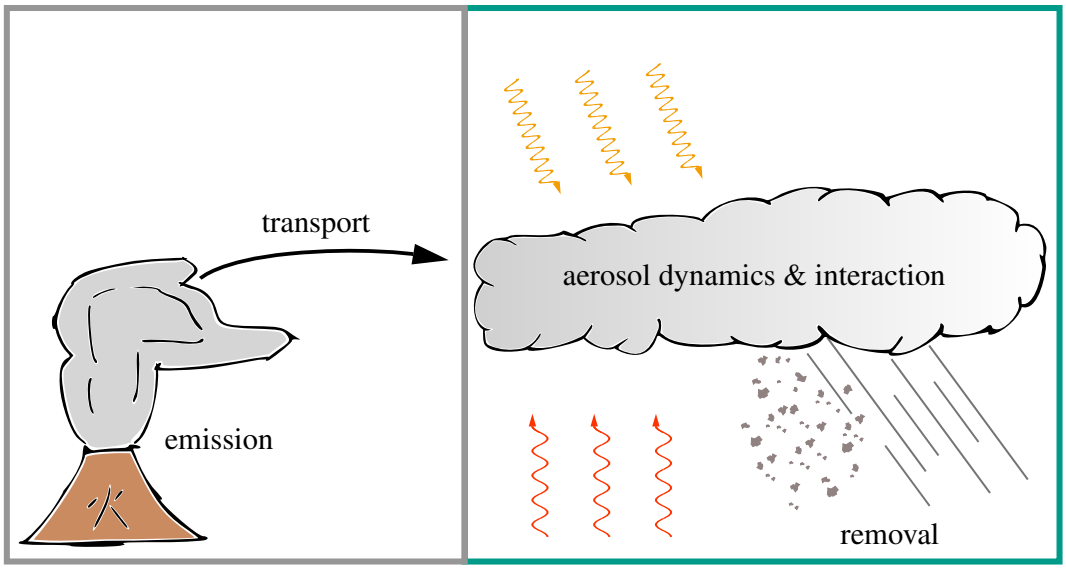

Figure 1.1: Important processes during the atmospheric lifetime of volcanic aerosols. The gray box includes processes on which most studies focus. Processes that are of particular importance in the scope of this thesis are highlighted by the green box.

Harvey et al., 2018; Gouhier et al., 2019). Important quantities are the mass of emitted particles and gases as well as the vertical distribution of mass release.

For the parametrization of the ash emission rate, often the empirical relation by Mastin et al. (2009) is used, e.g., at London VAAC for operational ash dispersion forecast (Beckett et al., 2020). The relation by Mastin et al. (2009) only depends on the observed plume height, a quantity that is often known shortly after an eruption. Therefore, it allows a timely response. However, the relation by Mastin et al. (2009) does not account for atmospheric conditions. On the one hand, latent heat release by humid air that is entrained into the plume can increase the plume height significantly. On the other hand, strong horizontal winds can bend the plume and, consequently, reduce the observed plume height (Beckett et al., 2020).

There exist more advanced approaches to determine the emitted mass by considering more variables, e.g., atmospheric and volcanic vent conditions. 1D plume models such as Plumeria (Mastin, 2007) or FPLUME (Folch et al., 2016) take these into account. There also exist approaches to couple these emission models to dispersion models (Marti et al., 2017; Bruckert et al., 2021). However, some of the necessary input parameters might not be available shortly after an eruption. This can restrict their application from use in operational volcanic aerosol dispersion forecasts.

Besides the total emitted mass, its vertical distribution in the atmosphere also needs to be represented. It is represented by the emission profile. In numerical models, such emission profiles are usually parameterized by either a uniform profile or more complex vertical profiles. Many studies (e.g., Flemming and Inness, 2013; Schmidt et al., 2014) use a uniform emission between a bottom and top height. The London VAAC also applies such a uniform profile as its default method (Beckett et al., 2020). More complex vertical distributions can be used at London VAAC if the necessary information is available

(Beckett et al., 2020) or are used in recent studies (e.g., Marti et al., 2017; Bruckert et al., 2021). These studies show promising results with a good agreement between modeled and observed volcanic aerosol concentrations. I present more details on volcanic emissions in Sect. 2.1.

Emissions of volcanic SO_2 are not represented in operational volcanic aerosol dispersion forecast currently (Beckett et al., 2020). Nevertheless, its dispersion is part of research in regards to air traffic safety (Schmidt et al., 2014) and even public health (Heaviside et al., 2021). Emission parameters for SO_2 dispersion simulations are often derived from remote sensing retrievals (e.g., Flemming and Inness, 2013; Dingwell et al., 2016; de Leeuw et al., 2021). The emission profile is either assumed to follow the ash emission in the simulation (Bruckert et al., 2021), it is derived from remote sensing retrievals (Carboni et al., 2016; de Leeuw et al., 2021) or it is determined by inverse modeling (Flemming and Inness, 2013; de Leeuw et al., 2021).

Some studies suggest that SO_2 can be used as a proxy for volcanic ash (Sears et al., 2013; Flemming and Inness, 2013). However, volcanic ash and SO_2 can be emitted during different phases of an eruption and be released at different altitudes. Additionally, wind shear and the different densities of ash and SO_2 in combination with gravity can lead to a separation of the two plumes (Kerminen et al., 2011; Grainger et al., 2013).

Despite the extensive research, large uncertainties remain in the formulation of eruption source parameters (Prata et al., 2019; von Savigny et al., 2020).

Transport

Following the schematic in Fig. 1.1, the transport of particles and gases is another crucial process. The correct transport is more determined by the dynamical core of the atmospheric model, i.e., how accurate the atmospheric state is captured in terms of wind speed and direction. As the focus of this thesis is on aerosol dynamics and interaction, the dynamical core of models is not further elaborated here. Some information can be found in Sect. 3 and literature (e.g., Zängl et al., 2015; Rieger et al., 2015).

The gray box in Fig. 1.1 highlights two processes, emission and transport. Operational volcanic aerosol dispersion forecast systems typically incorporate these processes. In contrast to that, processes depicted in the green box of Fig. 1.1 are usually not considered or receive less attention in recent studies (Beckett et al., 2020).

Within a volcanic cloud aerosol dynamic processes occur that change the physico-chemical properties of volcanic aerosol. Furthermore, due to aerosol–radiation interaction volcanic aerosol can influence the surrounding atmosphere. Both processes have the potential to alter the spatial distribution and the atmospheric lifetime of the aerosol, hence, influence the removal of particles.

Aerosol Dynamics

Kipling et al. (2016) show that the vertical distribution of aerosol in general depends strongly on aerosol dynamic processes such as nucleation, condensation, and coagulation.
Coagulation is a term that is used to describe the process of particles adhering to each other (Smoluchowski, 1927). In volcanic research, the term ash aggregation is often used to describe the same process. In the scope of this thesis I stick to the term coagulation. Brownian motion of particles and electromagnetic forces are the main driver for coagulation. Ultimately, coagulation forms larger particles. During the past three decades, coagulation of volcanic ash has been part of research (Brown et al., 2012, and references therein). If coagulation is ignored in numerical ash dispersion models, they tend to underestimate the ash fallout and overestimate atmospheric ash concentrations at distances > 1000 km from the volcano (Brown et al., 2012). However, even state-of-the-art models only consider coagulation within the eruption plume, if at all (Textor et al., 2006b; Van Eaton et al., 2015; Folch et al., 2016; Marti et al., 2017; Beckett et al., 2020). In other words, coagulation effects are usually only considered during the emission of volcanic aerosol, but not during its transport.
Volcanic ash size and shape influence the dispersion. At a given distance from the volcano, particles found on ground are larger than the one airborne. Further, particles on ground tend to be more spherical then airborne ones (Pardini et al., 2016). Particle size and shape change over time due to aerosol dynamic processes such as nucleation, condensation, and coagulation. These processes lead to the chemical aging of volcanic aerosol. The chemical aging of volcanic ash, i.e., sulfate, water, and other substances adhere to the surface of ash particles, increases their size and reduces their non-sphericity. O'Dowd et al. (2012) found chemically aged ash particles over Ireland after the Eyjafjallajökull eruption. It consisted of a mixture of 15% ash coated by 25% sulfate and 55% water. Zhu et al. (2020) show that the lifetime of volcanic SO_2 and sulfate particles in the stratosphere is reduced in the presence of volcanic ash. They state that "43% more volcanic sulfur is removed from the stratosphere in 2 months" due to aerosol dynamic processes, i.e., uptake of sulfur components on ash. Despite these studies, operational volcanic aerosol dispersion forecast systems ignore the chemical aging of volcanic aerosol (Beckett et al., 2020).

Aerosol–Radiation Interaction

The aerosol–radiation interaction can result in a vertical movement of aerosol that is different from large scale atmospheric dynamics (Khaykin et al., 2017; Walter, 2019). However, large uncertainties remain in the description of aerosol optical properties (Randall et al., 2007; Boucher et al., 2013). Moreover, the aerosol feedback to radiation interaction is expected to be nonlinear (Palacios-Peña et al., 2020).
There are few modeling studies on historic volcanic eruptions that investigate the influence of aerosol–radiation interaction on the dispersion of SO_2 together with volcanic ash (e.g., Niemeier et al., 2009; Pitari et al., 2016; Niemeier and Schmidt, 2017). Niemeier et al. (2009) show that fine ash particles absorb shortwave and longwave radiation, which results in a heating and cooling of ± 20 K per day. This

temperature change modifies the transport of the ash and SO_2 cloud. Especially on short time scale and at local scale this effect can be substantial. The effect depends strongly on the optical properties of volcanic aerosol particles (Niemeier et al., 2009; Timmreck, 2012; Vernier et al., 2016).
Offline models generally ignore aerosol–radiation interaction, i.e., operational volcanic aerosol dispersion forecast systems (Beckett et al., 2020). Not representing this feedback mechanism in dispersion models can lead to compensating measures to account for observed volcanic cloud lifting. For example, de Leeuw et al. (2021) performed a model study in which aerosol–radiation interaction is neglected. They compensate the lifting of the SO_2 cloud after the Raikoke eruption in 2019 by emissions into higher altitudes. On the contrary, Bruckert et al. (2021) show that the SO_2 cloud is lifted by aerosol–radiation interaction induced heating of upper tropospheric layers.

Combining Aerosol Dynamics and Interaction

Besides the modification of the aerosol size distribution and composition, nucleation, condensation, coagulation, and sedimentation, they also alter the optical properties of the particles involved (Delmelle et al., 2007; Durant et al., 2010; Ayris and Delmelle, 2012; Bagnato et al., 2013; Hoshyaripour et al., 2015; Seinfeld and Pandis, 2016; Vogel et al., 2017). Studies show that these changes influence the dispersion of the aerosol (e.g., Abdelkader et al., 2017; Peterson et al., 2017; Yu et al., 2019). Abdelkader et al. (2017) simulated the chemical aging of mineral dust particles during transatlantic transport. Their results show an increased aerosol optical depth (AOD) in regions of subsaturation due to water uptake of aged dust. This can result in local feedback on surface wind and dust emissions. Furthermore, the increased hygroscopicity of aged dust results in larger particles which are removed more efficiently by wet and dry deposition (Abdelkader et al., 2017). An observational study on the chemical aging of atmospheric pollutants in the Arctic near-surface atmosphere is presented by Peterson et al. (2017). They identify heterogeneous reactions on aerosol particle surfaces as the cause for the large spatial extent of bromine components beyond their source region. Yu et al. (2019) studied the smoke plume after forest fires in Canada in August 2017 in a combined approach of model simulations and satellite observations. They show that the radiation heating of chemically aged black carbon is a key ingredient for the long atmospheric lifetime observed. In their study, aerosol–radiation interaction results in a plume lifting from 15 to 20 km within 10 days.
There still remain large uncertainties in numerical dispersion models with respect to aerosol dynamic processes and aerosol–radiation interaction (Prata et al., 2019; von Savigny et al., 2020). The question remains how aerosol dynamic effects influence optical properties and the dispersion of aged volcanic aerosol. In this thesis, I aim to shed light on this gap by extending the ICON-ART modeling system. A new aerosol dynamic module called AERODYN (AEROsol Dynamics) is implemented. It allows to account for secondary aerosol formation and aerosol dynamic processes.

Improve Initial State

It was mentioned above that volcanic aerosol dispersion forecast is an initial value problem and that there are two requirements for a correct and reliable forecast. First, a correct initial state from which the forecast is started and, secondly, the accurate representation of all relevant processes in the model. As the true initial state is generally not known, a best estimate is required. This best estimate is derived with the help of data assimilation.

Data assimilation has been used in operational weather forecast for a long time. Carrassi et al. (2018), for example, give a review on different methods. In recent years, data assimilation became more and more available in atmospheric chemistry models (Bocquet et al., 2015), e.g., for air quality forecast (Montoya et al., 2020). Especially for volcanic aerosol dispersion forecast, data assimilation can be a useful tool to overcome the large uncertainties with respect to eruption source parameters, aerosol dynamic processes and aerosol–radiation interaction.

There exist several approaches to use data assimilation for the simulation of volcanic aerosol dispersion. These approaches range from simple data insertion techniques (Wilkins et al., 2015, 2016) over variational assimilation approaches (Schmehl et al., 2011; Lu et al., 2016; Plu et al., 2021) to ensemble based Kalman filters (Fu et al., 2016; Osores et al., 2020; Pardini et al., 2016). The assimilation of observational data for volcanic aerosol dispersion forecast relies mainly on the remote sensing of satellite instruments. Wilkins et al. (2016) suggest the use of data insertion techniques for remote and little monitored volcanoes. In cases when little or nothing is known about the eruption source parameters, data assimilation is crucial for a correct forecast. Wilkins et al. (2016) tested their setup for the case of the Eyjafjallajökull eruption in 2010 and proved its potential. However, they also highlight, that special care should be given to the quality control of the observational data that is used. Often, the remote sensing of ash clouds can be difficult when the volcanic cloud is too dense or obscured by water clouds (Prata and Lynch, 2019).

Plu et al. (2021) used a 3D variational (3D-Var) approach to test data assimilation within the MOCAGE model. They found a rather small and only local effect of the assimilation on the forecast. They assimilated AOD from the polar orbiting MODIS instrument. The use of data from a geostationary platform might overcome some of the deficiencies (Plu et al., 2021).

Fu et al. (2016), Osores et al. (2020), and Pardini et al. (2020) emphasize that an ensemble based approach can be useful for the assimilation of volcanic ash. All three studies were done with a different dispersion model, a different assimilation system, and for a different volcanic eruption.

An important unresolved issue remains the problem of missing information on the volcanic cloud height and cloud thickness (Pardini et al., 2020). Typical satellite retrievals such as AOD or column integrated mass do not contain any of these information. Incorporating other observational data, such as in-situ aircraft measurements of aerosol concentrations (Fu et al., 2016), proofed to be valuable. Fu et al. (2016) suggest that this kind of in-situ measurements can be very helpful for monitoring and forecasting distal

parts of the volcanic cloud. However, aircraft measurements might not be available for a timely response shortly after an eruption.
For an operational system, such as at London VAAC, the assimilation method should be computationally fast and the observations must be of good quality (Beckett et al., 2020). That also means, a sufficient spatial and temporal coverage is needed. I mentioned already that satellite retrievals on volcanic ash clouds can be difficult, as the cloud might be obscured (Prata and Lynch, 2019). Additional uncertainties arise due to the unknown size, shape, composition, and porosity of volcanic ash particles. Satellite retrievals are quite sensitive to these properties (Kylling et al., 2014; Stevenson et al., 2015; Western et al., 2015). The missing height information in most satellite retrievals remains a problem. Ground based vertical Lidar profiles or profiles of the polar orbiting CALIOP instrument can provide some of the missing information. However, the spatial and temporal resolution of such instruments is low.

1.2. Thesis Objectives

The aim of this thesis is the improvement of volcanic aerosol dispersion forecasts. I pursue this goal in two ways. First, the formation of secondary volcanic aerosol, the chemical aging of volcanic aerosol, and the interaction of the resulting internally mixed particles with radiation is implemented in ICON-ART. Both processes are currently missing in most atmospheric dispersion models (compare Fig. 1.1). Secondly, I develop a data assimilation method for volcanic aerosol to improve the initial state and overcome deficiencies of the volcanic emission parametrization as well as other model uncertainties. I make this development within the DWD data assimilation framework, which is a step towards the operational use of data assimilation for volcanic aerosol dispersion forecasts at DWD.
With these new developments, I address the following research questions:

1. How do aerosol dynamic processes influence the volcanic aerosol dispersion?
2. Which of the aerosol dynamic processes is most relevant and has the largest effect on aerosol dispersion?
3. What is the influence of the interaction between radiation and volcanic aerosols on their transport?
4. Is the combined representation of aerosol dynamic processes and aerosol–radiation interaction beneficial for volcanic aerosol dispersion forecast?
5. What is the potential of an En-Var method for the assimilation of column integrated ash mass?

I investigate these questions in the context of the Raikoke eruption 2019. Raikoke is a stratovolcano which is located on one of the central Kuril islands in the Sea of Okhotsk (48.29° N, 153.24° E). On 21 June 2019 at 18:05 UTC the Raikoke volcano started to erupt (Sennert, 2019). In a series of several individual, short outbursts and one longer, continuous eruption (Bruckert et al., 2021) approximately

190 Tg of tephra and 1.5 Tg SO_2 were emitted (Muser et al., 2020). The eruption column rose to altitudes between 8–14 km and released aerosol and gases in both the troposphere and stratosphere. It was one of the largest volcanic eruptions during the last 30 years. Due to its remote location, the eruption only caused the rerouting of 40 airplanes (Sennert, 2019). During and after the Raikoke eruption, several satellite instruments were in place to sense the volcanic cloud at a high spatial and temporal resolution. Due to the good observational data availability, the strength of the eruption, and the temporal proximity of this thesis to the eruption, the Raikoke eruption of 2019 is well suited as a case study to validate my new implementations and to answer the posed research questions.

1.3. Thesis Outline

This thesis contains basic information on volcanic aerosol formation and their physico-chemical properties in Sect. 2. Section 3 describes the modeling system ICON-ART together with the new implementations regarding aerosol dynamic processes and the optical properties of internally mixed particles. Section 4 contains a short summary on the observational data that I use to validate the model results. The methods and tools that are used to evaluate the model results are presented in Sect. 5. Furthermore, the data assimilation method is explained here. I present and discuss results of the model simulations of the Raikoke eruption in 2019 in Sect. 6. These results show the influence of aerosol dynamic effects and aerosol–radiation interaction on the dispersion of volcanic aerosols. The potential of data assimilation for volcanic aerosol forecast is presented in Sect. 7, also for the case of the Raikoke eruption 2019. Section 8 provides a summary of the thesis.

2. Volcanic Aerosol – Origin and Properties

Volcanic eruptions are one of the most impressive, but also most hazardous natural phenomena on Earth. There exist a variety of different eruption types ranging from effusive eruptions with only local effects to large explosions which have global impacts that are detectable for several years after the eruption. This section contains fundamentals about volcanic eruptions and the emission of volcanic aerosol in Sect. 2.1. Section 2.2 explains the formation of secondary volcanic aerosol. The physico-chemical properties of the different volcanic particles are presented in Sect. 2.3. I provide an introduction to the concept of aerosol aging in Sect. 2.4. Finally, Sect. 2.5 contains details on the interaction of aerosol with radiation. More detailed information on all these topics can be found in classical textbooks, e.g., in Schmincke (2004) and Seinfeld and Pandis (2016).

2.1. Volcanic Emissions and How to Describe Them

A volcanic eruption is accompanied by the emission of lava, tephra, and volcanic gases. Lava describes molten rock that has reached the (Earth's) surface, whereas, the term magma is used for molten rock below surface. Tephra describes all ejected solid materials that can range in size from large boulders to very fine volcanic ash particles. The mixture of volcanic gases depends strongly on the volcanic activity and the tectonic setting, however, the most abundant components usually are water, carbon dioxide CO_2, and sulfuric compounds such as sulfur dioxide SO_2. There exist three different mechanisms that drive the ejection of these materials during eruptions (Schmincke, 2004). First, so-called magmatic eruptions are driven by gas release from magma under decompression. Dissolved gases in the magma can form bubbles and propel the magma up the volcanic vent. This principle can easily be pictured by opening a shaken bottle of sparkling water. The second mechanism is based on the interplay between magma and water. The rapid heat exchange between magma and water leads to a high level of magma fragmentation and steam explosions. These eruptions are called phreatomagmatic. The third mechanism does not include the ejection of magmatic material. For this eruption mechanism magma only evaporates water, leading to steam explosions. Together with the steam, solid materials can be ejected by these so-called phreatic eruptions.

A volcanic eruption can be driven by a mix of these mechanisms during different phases of the eruption. As an example, the initial phase of the Eyjafjallajökull eruption 2010 was phreatomagmatic as the glacier cap was melting. Over time, less water reached the vent area, hence, magmatic effects dominated the final phase (Dellino et al., 2012; Gudmundsson et al., 2012).

Table 2.1: Volcanic Explosivity Index by Newhall and Self (1982) and the two major distinction criteria together with a representative (historic) example. The plume height for VEIs 0 – 2 is measured in height above crater, for VEIs ≥ 3 in height above sea level.

VEI	Ejected volume	Plume height	Example
0	$< 10^4$ m^3	< 100 m	Kilauea
1	$> 10^4$ m^3	$100 - 1000$ m	Stromboli
2	$> 10^6$ m^3	$1 - 5$ km	Whakaari (2019)
3	$> 10^7$ m^3	$3 - 15$ km	Eyjafjallajökull (2010)
4	$> 10^8$ m^3	$10 - 25$ km	Raikoke (2019)
5	$> 10^9$ m^3	> 25 km	St. Helens (1980)
6	$> 10^{10}$ m^3	> 25 km	Pinatubo (1991)
7	$> 10^{11}$ m^3	> 25 km	Tambora (1815)
8	$> 10^{12}$ m^3	> 25 km	Taupo (26500 BC)

Whether a magmatic eruption is rather effusive or explosive mainly depends on the viscosity of the magma. Volcanic activity with a low-viscous magma tends to be effusive, as it can be observed for example on Hawaii or Stromboli. More destructive explosive eruptions occur at volcanoes which usually contain more viscous magma. Only these explosive volcanic eruptions generate very fine volcanic ash particles in great amounts. Such an explosion ejects the particles up to several kilometers into the atmosphere from where these particles can be transported over large distances. This is the reason why in the scope of this thesis only explosive eruptions are of interest.

In order to compare the strength of different volcanic eruptions objectively, Newhall and Self (1982) proposed the Volcanic Explosivity Index (VEI). The index is based on an open-ended, logarithmic scale and classifies the eruption strength according to the ejected volume and the plume height. As shown in Table 2.1, values for VEI range from 0 to 8. For VEI ≥ 2, an increase in VEI by one translates to a ten times higher ejected volume. Furthermore, Table 2.1 lists prominent historic eruptions for each corresponding VEI.

The particle size of tephra during explosive eruptions can range over several orders of magnitude. Schmincke (2004) describes two main boundary conditions that control the fragmentation of magma into particles. The first one is the formation of a magmatic foam. This magmatic foam is generated due to the degassing of magma in the magma chamber and conduit. The thin and unstable walls of the melt in the foam are then torn apart. The second boundary condition is the brittle fracture of magma when the tensile stress of the melt is exceeded (Schmincke, 2004).

During explosive eruptions the mixture of hot gases and tephra leaves the volcanic vent at high velocities. The region in which the upward motion is dominated by the remaining momentum of particles and gases is called gas thrust or jet region. Due to turbulent mixing at the sides of the plume, up to four times its mass of (cold) ambient air can be entrained (Schmincke, 2004). The successive expansion of the

entrained air reduces the density of the volcanic plume significantly. In case the density of the plume is reduced to a level below that of the surrounding air, further lifting of the volcanic plume occurs due to convection. The convective region stretches up to a height at which the plume reaches neutral buoyancy. The continuing entrainment of ambient air in the convective region and the successive cooling brings the density of the plume in equilibrium with the ambient air at neutral buoyancy level. At this level the emitted material starts spreading horizontally. This region is called the umbrella of the plume. The schematic in Fig. 2.1 illustrates these different plume regions, however, the heights are not to scale.
Additionally, there exists another mechanism that has the potential to emit very fine volcanic ash particles high into the atmosphere. This mechanism does not depend on direct emissions by the volcanic vent. Instead, it is based on convective systems that develop around the volcano over hot deposits of ejected material. These deposits are called ignimbrite and reach temperatures of several hundred centigrade. Due to their high temperature, convective systems form over the ignimbrite. These convective systems can carry large amounts of very fine ash which are visible as so-called co-ignimbrite plumes (also known as co-PDC plumes). They can add substantially to the total emission of very fine volcanic particles into the atmosphere (Perrotta and Scarpati, 2003).

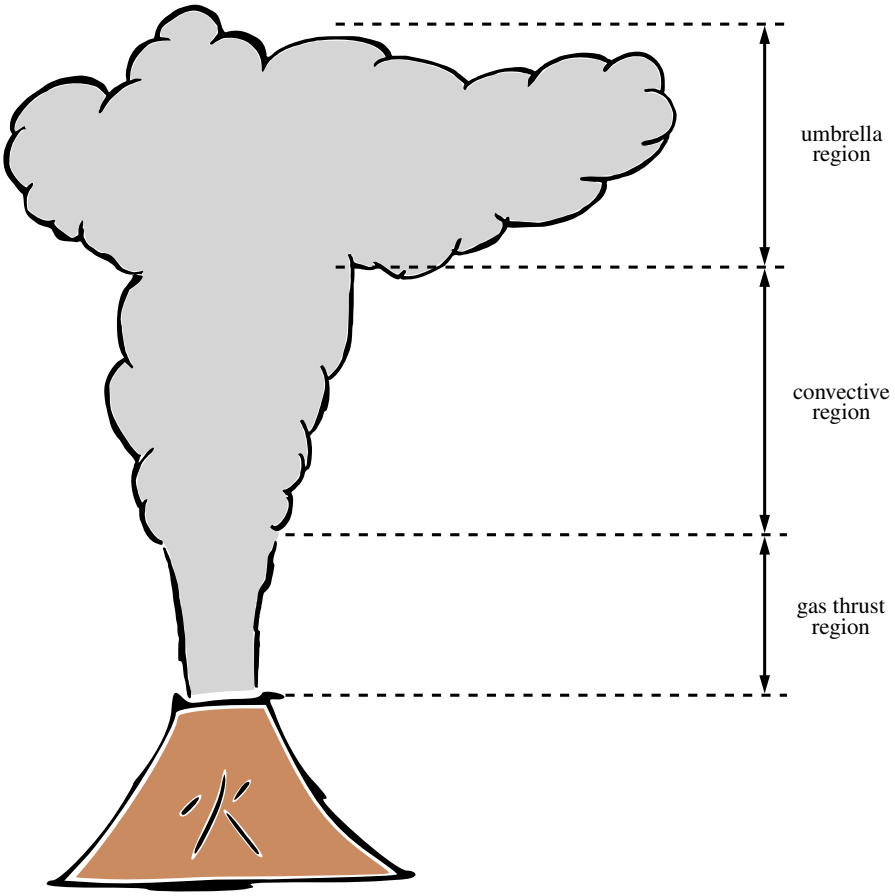

Figure 2.1: Volcanic plume regions for large volcanic eruptions. The lengths are not to scale.

The total flux of tephra through the volcanic vent is called mass eruption rate (MER). It is an important quantity when it comes to volcanic aerosol dispersion forecast. There exist multiple approaches on how to obtain the MER at different levels of complexity. A rather simple approach is the empirical relation by Mastin et al. (2009)

$$MER = \left(\frac{1}{0.3035}h\right)^{\frac{1}{0.241}} . \tag{2.1}$$

It is simple in a way, that only the emission height h in km above vent is needed to determine the MER in $\mathrm{kg\,s^{-1}}$. This relation is used in operational volcanic ash forecast (Beckett et al., 2020) and is also available for simulations in ICON-ART (Rieger et al., 2015).

More sophisticated approaches to determine the MER are given by one-dimensional plume models such as Plumeria (Mastin, 2007) or FPLUME (Folch et al., 2016). They consider more physical processes for the calculation of the MER, e.g., the atmospheric state and vent conditions. Such one-dimensional plume models have successfully been applied in simulations of volcanic aerosol dispersion (Marti et al., 2017; Bruckert et al., 2021), however, the amount of input data can restrict their use for operational volcanic aerosol dispersion forecast.

As the MER comprises all emitted tephra, it also contains material that is too large and heavy to stay in the atmosphere for long. Only the smallest particles are injected high enough and remain in the atmosphere long enough in order to being transported over large distances. These small particles with diameters $d_p < 32$ µm are classified as *very fine ash* by volcanologists (Rose and Durant, 2009).

Gouhier et al. (2019) studied the partitioning very fine ash from all tephra during historic volcanic eruption in detail. They show that eruptions with higher VEI, hence, more explosive eruptions, produce a smaller fraction of very fine ash f_{lrt} that is small enough for long-range transport. Furthermore, they state a statistical model that allows to estimate f_{lrt} based on MER. Typically, the fraction of very fine ash of the total MER is $f_{lrt} < 5\%$. However, a fix value $f_{lrt} = 5\%$ is often used in operational volcanic ash forecast (Beckett et al., 2020).

Volcanic aerosols and gases are not released at one point at a height h above the volcano, but over a vertical profile. This profile is needed to fully describe the emission. If an umbrella cloud exists, most of the very fine ash is released in the umbrella region as indicated by the schematic in Fig. 2.1. However, it is difficult to formulate a generally applicable profile that describes the ash release over height for all volcanic eruptions. The vertical distribution of ash release is sometimes modeled by so-called Suzuki profiles (e.g., Marti et al., 2017; Bruckert et al., 2021). In operational forecasts done by VAACs a uniform profile is used (Beckett et al., 2020).

2.2. Secondary Volcanic Aerosol Formation

Secondary aerosols are particles that are not directly emitted into the atmosphere, but form out of gaseous precursor substances. This formation process is called nucleation.

Volcanoes can emit large amounts of SO_2. Sulfur dioxide undergoes chemical reactions in both gas- (homogeneous) and aqueous-phase (heterogeneous), whereby it is depleted. Another sink for SO_2 is the dry and wet deposition of the gas (Seinfeld and Pandis, 2016). The gas-phase reaction in the troposphere is dominated by the reaction with the OH radical as described by Stockwell and Calvert (1983). They propose a three step reaction chain. In the first two steps,

$$SO_2 + OH + M \longrightarrow HOSO_2 + M \qquad \text{[R 1]}$$

and

$$HOSO_2 + O_2 \longrightarrow HO_2 + SO_3 \qquad \text{[R 2]}$$

SO_2 is transformed into SO_3. Finally, in the presence of water vapor, SO_3 reacts rapidly to sulfuric acid (H_2SO_4)

$$SO_3 + H_2O + M \longrightarrow H_2SO_4 + M \qquad \text{[R 3]}$$

Sulfuric acid is a precursor gas that tends to either condense on existing particles, e.g., volcanic ash, or it nucleates and forms particles. In general, nucleation describes a process that transforms a phase A to phase B. It can be observed in many connections, e.g., formation of droplets in a vapor phase, formation of crystals in a liquid phase, and formation of bubbles in a liquid phase. For this work, the nucleation of sulfate (SO_4^{2-}) droplets out of gaseous H_2SO_4 is of relevance. This is why in the following only the terms droplets and gas are used. Details about the physics of the nucleation process can be found in textbooks, e.g., Seinfeld and Pandis (2016).

There exist two main nucleation processes, homogeneous and heterogeneous. Homogeneous nucleation describes the formation of droplets out of the gaseous phase without any foreign material, solid or liquid, present. In the presence of foreign material at which surface droplets can form, heterogeneous nucleation takes place. For both processes, there can be a single species (homomolecular) or a mix of multiple species (heteromolecular) involved. The nucleation of H_2SO_4 in the atmosphere is a binary, i.e., heteromolecular, homogeneous nucleation system. It is called binary as there are two species involved, water and sulfuric acid. The resulting particles are then a solution of sulfate and water. The nucleation of sulfuric acid has been studied by several authors. Details can be found for example in Doyle (1961), Kulmala and Laaksonen (1990), and Noppel et al. (2002).

A prerequisite for nucleation is a supersaturation $s = p_A/p_A^s(T) > 1$ of H_2SO_4 vapor. The partial pressure of a substance A is denoted by p_A and its saturation vapor pressure by p_A^s. For a binary system, it is sufficient that the participating vapor species are supersaturated with respect to a liquid solution droplet. Nucleation is a gas kinetic process during which gas molecules stick to each other and form clusters. These clusters must reach a critical size, before they grow further at the expense of the supersaturation into liquid particles. Resulting sulfate (SO_4^{2-}) particles have a diameter $d_p \approx 0.01$ µm (Whitby, 1978).

2.3. Physico-Chemical Properties of Volcanic Aerosols

For this work, only volcanic particles that have the potential to remain in the atmosphere for at least several hours to days are important. Only such particles are transported over large distances and jeopardize air traffic or influence weather and climate. That is why the following properties are restricted exclusively to such particles, i.e., very fine ash and sulfate particles.

Particle sizes in atmospheric aerosols range over several orders of magnitude (Whitby, 1978; Boucher, 2015). The different size ranges are also called modes. The diameter range 0.01 µm $< d_p <$ 0.1 µm is classified as the Aitken mode, in the range 0.1 µm $< d_p <$ 1 µm as the accumulation mode, and between 1 µm $< d_p <$ 10 µm as the coarse mode. Larger particles are sometimes classified as supercoarse (Boucher, 2015) or giant mode particles (in this work). The name accumulation mode already indicates that particles tend to accumulate in this mode due to aerosol dynamic processes (compare Sect. 2.4). Typically, Aitken mode particles exist in great numbers, but account for little mass. The opposite is true for coarse mode particles. The large particles sediment fast, hence, are removed quickly from the atmosphere.

Sulfate particles that nucleate from sulfuric acid are in the size range of Aitken mode particles. Volcanic ash particles are typically larger and are emitted in the size range of the accumulation, coarse, and giant mode. Figure 2.2 displays ash size distributions for five historic eruptions (Bonadonna and Scollo, 2013). The markers indicate the fraction of particles with a diameter d_p of the total very fine ash mass emitted by the volcano.

Volcanic ash consists of different minerals depending on the tectonic setting of the volcano. The particles' density can range between $800 - 2800\ \mathrm{kg\,m^{-3}}$ (Wilson and Huang, 1979; Textor et al., 2006a,b; Schumann et al., 2011). Many authors typically assume a value of $\rho_p \approx 2600\ \mathrm{kg\,m^{-3}}$. Sulfuric acid has a density of $1800\ \mathrm{kg\,m^{-3}}$. However, atmospheric sulfate droplets are usually in a solution with water. Rosen (1971) measured a H_2SO_4 content of 75% in stratospheric sulfate aerosol. In the troposphere lower H_2SO_4 contents can be expected. After the Eyjafjallajökull eruption 2010, O'Dowd et al. (2012) found volcanic aerosol particles over Ireland. These particles were emitted into and transported in the troposphere. They consisted of a mixture of 15% volcanic ash, 25% sulfate, and 55% water. Processes that lead to such a mixing state are explained in the following section.

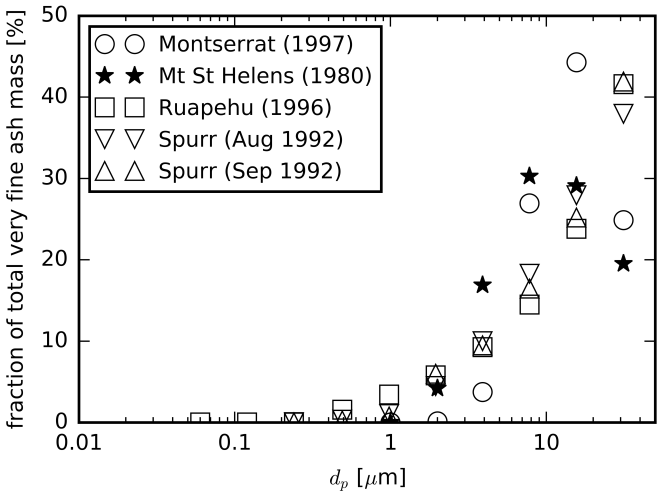

Figure 2.2: Volcanic ash size distribution of very fine ash particles for historic eruptions. Data available from Bonadonna and Scollo (2013).

2.4. The Concept of Aerosol Aging

Particles in the atmosphere exist in sizes that range from several nanometers to tens of microns. Due to microphysical processes these particle sizes can change over time. Figure 2.3 depicts typical size ranges and their related source and sink processes.

Secondary aerosol particles, e.g., SO_4^{2-}, form due to nucleation, as explained above, and rapidly grow to the size of Aitken mode particles, as indicated by the arrows in Fig. 2.3. Depending on their source, primary particles can be emitted in all modes. Very fine volcanic ash particles are usually emitted in the size range of the accumulation and coarse mode. Further details on the particle sizes are given in Sect. 2.3. The dominant microphysical processes that alter the size of single particles are condensation, coagulation, evaporation, and activation. Detailed descriptions of these processes can be found in textbooks, e.g., Seinfeld and Pandis (2016). During condensation gaseous substances, e.g., H_2SO_4, condense on already existing particles, such as volcanic ash or sulfate particles. Coagulation is a process during which particles interact with and stick to each other. The cause for coagulation is the Brownian motion of particles or electromagnetic forces.

Activation is the process when aerosol particles act as INP and CCN for ice and liquid clouds, respectively. The reverse process is called evaporation, which means that the water of the cloud droplet evaporates and leaves the remaining aerosol particle.

Gravitational settling, i.e., sedimentation, brings aerosol particles to lower altitudes. Dry deposition finally removes these particles and atmospheric trace gases at the Earth's surface. Wet deposition, as the name suggests, incorporates liquid water. Aerosol particles either act as INP or CCN and are removed by precipitation. Or the particles are scavenged by falling rain droplets.

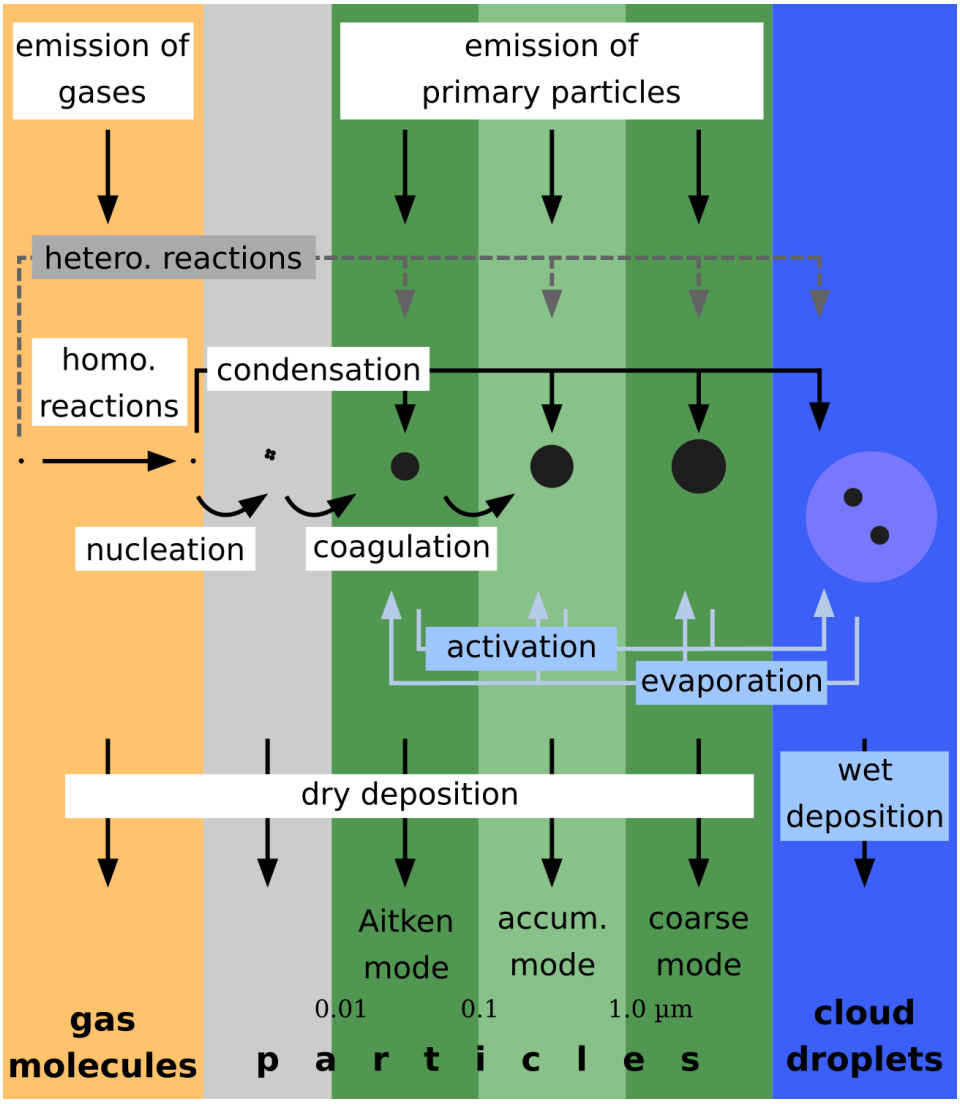

Figure 2.3: Typical microphysical processes that generate, transform, and remove atmospheric constituents. (Adapted from Raes et al. (2000))

Homogeneous reactions describe chemical reactions in which reactants and products are all in the same phase, i.e., in Fig. 2.3 gas phase reactions. On the contrary, in the context of atmospheric chemistry heterogeneous reactions incorporate liquid water.

Black arrows in Fig. 2.3 indicate processes that are of particular interest in the scope of this thesis. Condensation and coagulation have the potential to form internally mixed particles. As sketched in the top left of Fig. 2.4, an external mixture consists of different particles for which single particles consist of one substance. On the contrary, in an internal mixture single particles consist of more than one substance. In volcanic plumes, condensation and coagulation form a coating on ash particles that consists for example of water or sulfate. The top right of Fig. 2.4 shows such coated particles that are also called aged particles. This leads to a state in which coated and uncoated particles are externally mixed, as depicted in the lower panel of Fig. 2.4.

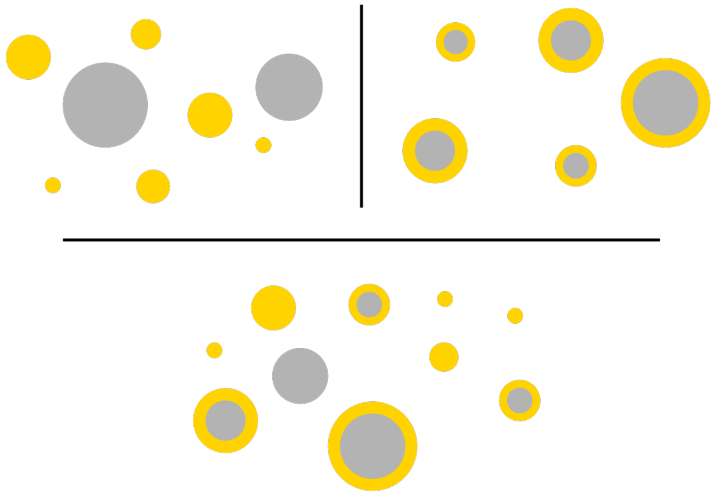

Figure 2.4: Different types of aerosol mixtures: Top left shows externally mixed volcanic ash and sulfate particles. The top right shows internally mixed particles on the example of sulfate coated volcanic ash. The bottom schematic displays an external mixture of internally mixed particles as it is used in this thesis.

2.5. Interaction of Volcanic Aerosols with Radiation

A rainbow nicely visualizes the interaction of solar radiation with small, airborne water droplets. In general, every particle in the atmosphere interacts with electromagnetic waves. Usually, however, with less visual effects for human eyes. Depending on the material of the particle and the wavelength of radiation, incident photons are either absorbed, scattered or transmitted. Comprehensive explanations about the basics of atmospheric radiation and its interaction with particles can be found in literature, e.g., in Petty (2006) or Mishchenko (2014). Here, only the necessary basics are replicated.
An important quantity that describes the optical properties of a particle is the complex refractive index

$$B_\lambda = \mathrm{Re}(B_\lambda) + i\,\mathrm{Im}(B_\lambda)\,. \tag{2.2}$$

The complex refractive index is a material property that varies for different wavelengths. From its real part $\mathrm{Re}(B_\lambda)$ we can determine the effective phase speed of the electromagnetic wave traveling through the material. The imaginary part $\mathrm{Im}(B_\lambda)$ gives the rate of absorption of the wave in the material. For a given wavelength λ, the volume absorption coefficient

$$\beta_a = \frac{4\pi\,\mathrm{Im}(B_\lambda)}{\lambda} \tag{2.3}$$

can be determined. It has the dimensions of an inverse length. The reciprocal of β_a can be interpreted as the distance the electromagnetic wave needs to travel at which $e^{-1} \approx 37\%$ of its original value is absorbed.

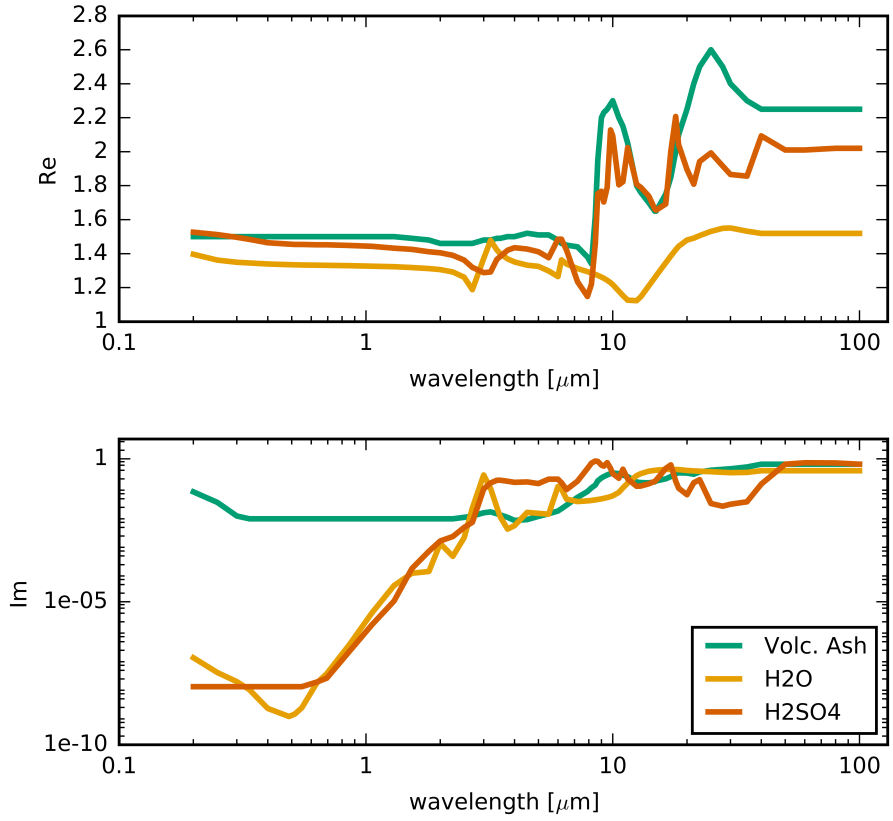

Figure 2.5: Complex refractive indeces of volcanic ash, water, and sulfuric acid. The ash data is from Walter (2019). The data for water and sulfuric acid is taken from the HITRAN database (Gordon et al., 2017).

Figure 2.5 displays the refractive indices of volcanic ash, water, and sulfuric acid. The data for volcanic ash is taken from Walter (2019). Values for water and sulfuric acid are listed in the HITRAN2016 database (Gordon et al., 2017).

Absorption is not the only process that removes photons from their path of travel. Another possibility is the scattering of photons out of their original trajectory. Comparable to β_a we can describe the removal of photons from their path of travel due to scattering with the volume scattering coefficient β_s. The sum of absorption and scattering is called extinction. Consequently,

$$\beta_e = \beta_a + \beta_s \tag{2.4}$$

is the volume extinction coefficient.

When it comes to the interaction of radiation with an aerosol particle, not only its material is of importance, but also its size. That is why we define the extinction efficiency

$$Q_e = \frac{\sigma_e}{A_p}. \tag{2.5}$$

It is a non-dimensional quantity that relates the extinction cross section σ_e to the area of particle cross section $A_p = \frac{\pi}{4} d_p^2$. Note that for wavelengths in the order of the particle diameter d_p, σ_e can be larger than A_p, hence, $Q_e > 1$ (Petty, 2006).
Knowing the extinction cross section σ_e of a single particle and the number concentration N of these particles, we can derive

$$\beta_e = \sigma_e N \,. \tag{2.6}$$

Knowing the extinction coefficient, the attenuation of incident radiation along a path between z_1 and z_2 can be determined with Lambert-Beer's law:

$$I_\lambda(z_2) = I_\lambda(z_1) \exp\left(- \int_{z_1}^{z_2} \beta_e(z) dz \right) = I_\lambda(z_1) \exp\left(-\tau(z_1, z_2)\right) . \tag{2.7}$$

For a constant extinction coefficient between z_1 and z_2, the optical thickness (optical depth) τ can simply be derived by

$$\tau(z_1, z_2) = \beta_e \left(z_1 - z_2\right) . \tag{2.8}$$

Analogously to Eq. 2.6 the scattering coefficient

$$\beta_s = \sigma_s N \tag{2.9}$$

is derived. A relative measure that relates scattering to total extinction is the single scattering albedo ω. The non-dimensional quantity ω is defined as

$$\omega = \frac{\beta_s}{\beta_e} = \frac{\beta_s}{\beta_s + \beta_a} . \tag{2.10}$$

Values for ω range between 0 and 1. Zero indicates that all extincted photons are extincted due to absorption. A one would show that all extincted photons are extincted due to scattering.
Scattering of radiation is a rather complex physical process. Detailed explanations can be found in literature, e.g., Mishchenko (2014). In principle, radiation can be scattered in any direction. That said, it can be removed from its path of travel, but can also be scattered back into its path. For the macroscopic radiation budget in a global circulation model, such as ICON-ART, it is not feasible to calculate the exact scattering behavior of each particle. However, we can reduce the complexity to the relation of forward and backward scattering. This behavior is represented by the dimensionless asymmetry parameter g. Its values range between

$$-1 \leq g \leq 1 \tag{2.11}$$

whereas the lower and upper extreme value are rather hypothetical. For $g = -1$ all photons would be scattered in backward direction and for $g = 1$ in forward direction, respectively.

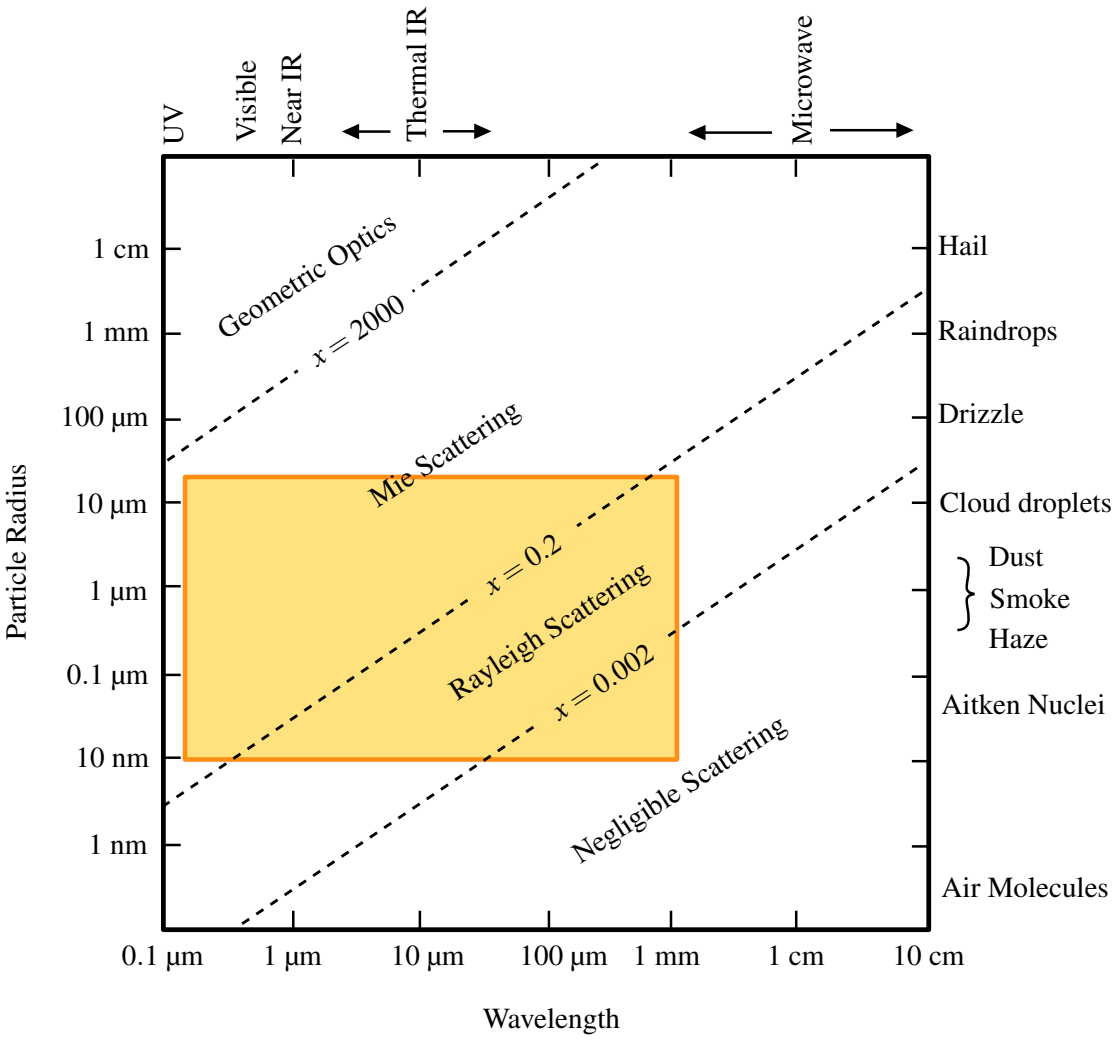

Figure 2.6: Scattering regimes as a function of particle size and wavelength for typical atmospheric particles and wavelengths. The orange box highlights the wavelengths and particle sizes of volcanic aerosols that are relevant in this work. Adapted from Petty (2006).

The interaction of particles of different size with radiation can be characterized with the nondimensional size parameter

$$x = \frac{\pi d_p}{\lambda}. \tag{2.12}$$

Different regimes for typical particle sizes and wavelengths are displayed in Fig. 2.6. For very small particles, such as air molecules, scattering can be neglected for most wavelengths of atmospheric radiation. Volcanic aerosols, however, typically lie within the Rayleigh Scattering and Mie Scattering regime. Typical sizes of volcanic aerosols and wavelengths relevant in the scope of this work are highlighted by the orange box.

The scattering behavior of particles has first been described in a comprehensive manner by Mie (1908). Mie assumed spherical, isotropic, homogeneous, and non-magnetic particles. He was able to derive the optical properties of these particles from the Maxwell equations. His solution also contains the earlier proposed, but only for special cases applicable, Rayleigh scattering. Hence, Mie's theory covers both regimes in Fig. 2.6, Mie and Rayleigh scattering.

There exist extensions to the classical Mie theory for concentric stratified spheres. These extensions are not replicated at his point, due to their complex structure. The reader is referred to literature, e.g., Toon and Ackerman (1981) or Tarcea (2004). Such extensions for concentric stratified spheres allow to compute the scattering behavior of internally mixed particles, i.e., ash particles coated with a mixture of sulfate and water.

So far, the scattering behavior was explained for spherical particles. Volcanic aerosol, volcanic ash specifically, are highly non-spherical particles (Johnson et al., 2012). Hoshyaripour et al. (2019) suggest that the effect of non-sphericity is rather low on the atmospheric radiation budget. However, they stress that the backscattering behavior and derived measurands, e.g., total attenuated backscatter measured by Lidar instruments, can differ significantly between spherical and non-spherical particles. Mishchenko et al. (1995, 1997); Mishchenko (2014) extensively studied the scattering behavior of non-spherical particles. A quantity that describes the scattering behavior of particles is the phase function. It describes the intensity of the scattered light at a specific scattering angle. Figure 2.7 shows phase functions for spherical and non-spherical particles at two different wavelengths (Mishchenko et al., 1997). The black line indicates the phase function for a polydisperse population of spherical particles. The colored lines present the phase functions for prolate (green), oblate (blue), and a mix of both (red) particles. The populations of non-spherical particles contain a mix of particles with different aspect ratios (Mishchenko et al., 1997). Figure 2.7 shows that the phase functions of the different particle populations significantly deviate at large scattering angles. Of particular interest is the value of the phase function at 180°, as this represents the intensity of the backscattered light. Both panels in Fig. 2.7 indicate that the intensity of backscattered light is much higher for spherical particles compared to non-spherical ones. This has implications for the comparison of model results with Lidar signals as discussed in Sect. 6.4.

As volcanic ash undergoes chemical aging, liquid components condense onto it. This coating reduces the highly irregular shape of volcanic ash particles and makes them more spherical.

Generally, the aerosol–radiation interaction can have three different effects, a direct, a semi-direct, and an indirect effect. The direct effect due to absorption or scattering of solar and terrestrial radiation, directly changes the radiation budget, by the mechanisms described above. On the one hand, volcanic aerosols reduce the incoming shortwave radiation that reaches ground level due to extinction of solar radiation. Hence, it can result in a cooler temperature at the surface. On the other hand, volcanic aerosols absorb shortwave and longwave radiation and heat the surrounding air. The absorption induced heating of atmospheric layers can lead to the semi-direct effect. These local temperature changes influence the formation and lifetime of clouds (Lohmann and Feichter, 2001). The indirect effect is related to the

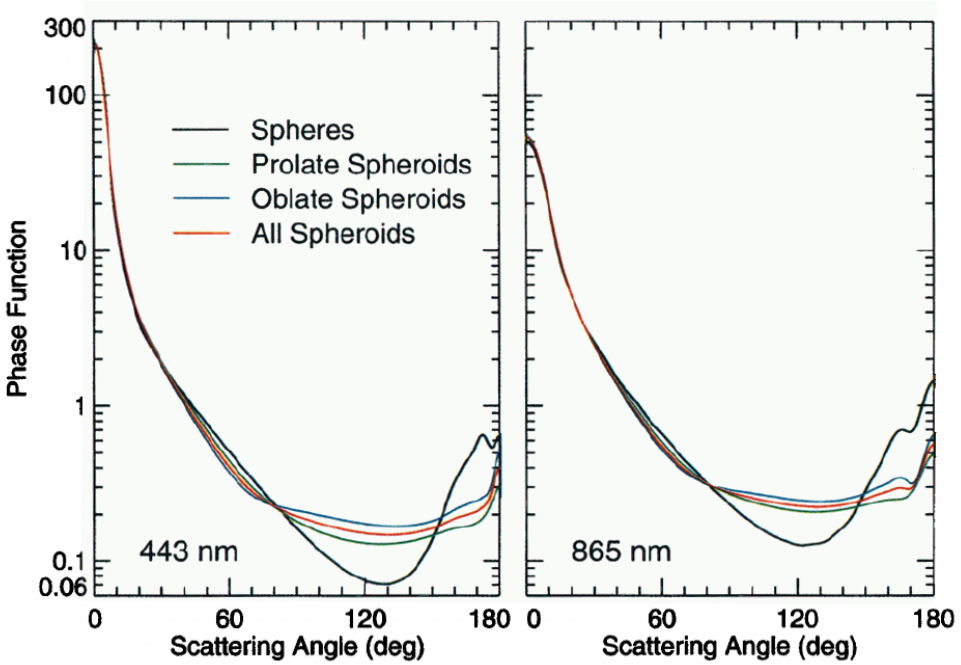

Figure 2.7: Phase functions for polydisperse spherical and spheroidal particles at two wavelengths, $\lambda = 443$ and $\lambda = 865$ nm in the left and right panel, respectively. The spheroid populations consist of particles with different aspect ratios. The figure is taken from Mishchenko et al. (1997).

activation of volcanic aerosols as cloud condensation nuclei (CCN) or ice nucleating particles (INP). The water-soluble sulfate particles are well known to act as CCN (Pruppacher and Klett, 2010). In contrast to that, volcanic ash have the ability to act as INP (Steinke et al., 2011; Hoyle et al., 2011). The resulting change of cloud properties, e.g., droplet size distribution, indirectly leads to a change in the radiation budget (Twomey, 1974; Albrecht, 1989).

3. The Modeling System ICON-ART

The improvement of volcanic ash dispersion forecast is attempted by extensions to the ICON-ART modeling system. ICON-ART consists of the ICOsahedral Nonhydrostatic weather and climate model (ICON) and the Aerosols and Reactive Trace gases (ART) module. The modeling system is developed jointly by DWD, the Max Planck Institute for Meteorology (MPI-M), the Institute of Meteorology and Climate Research (IMK) at Karlsruhe Institute of Technology (KIT), and the German climate computing center *Deutsches Klimarechenzentrum* (DKRZ). ICON is the state-of-the-art numerical weather prediction (NWP) model that is operationally used at DWD. It can be applied for seamless simulations of various processes across local to global scales (Zängl et al., 2015; Heinze et al., 2017; Giorgetta et al., 2018). The ART extension accounts for emission, transport, physico-chemical transformation, and removal of trace gases and aerosols in the troposphere and stratosphere (Rieger et al., 2015; Schröter et al., 2018). This thesis is based on extensions that I implemented into the ICON-ART modeling system to include aerosol dynamic effects and aerosol–radiation interaction.

3.1. Basics of the ICON Model

ICON solves the full three-dimensional non-hydrostatic and compressible Navier-Stokes equations on a horizontally unstructured triangular grid.

The horizontal grid is a triangular Arakawa C grid (Arakawa and Lamb, 1977) that is based on the successive refinement of a spherical icosahedron. The resulting grid with n_{cell} cells has an average spatial resolution of

$$\overline{\Delta x} = \sqrt{\frac{4\pi}{n_{cell}}} r_e \tag{3.1}$$

with the mean radius of the Earth r_e.

In the vertical, the model atmosphere is resolved by n_{lev} levels. For the vertical coordinate the terrain-following formulation (smooth level vertical coordinate) by Leuenberger et al. (2010) is used. Grid cells of one vertical column have all the same surface area.

The system of conservation equations is based on Gassmann and Herzog (2008) and was applied by Zängl et al. (2015). Equations for the conservation of mass, momentum, and energy are solved. The prognostic variables are the horizontal wind component normal to grid cell vertices v_n, the vertical wind component w, the air density ρ (including liquid and solid hydrometeors), and the virtual potential temperature θ_v.

3.2. Basic ART Equations

ART consists of an aerosol module (Rieger et al., 2015) and a gas-phase chemistry module (Weimer et al., 2017; Schröter et al., 2018).
For each species, either aerosol or chemical, a transport equation needs to be solved in ICON-ART. These transport equations are formulated in a Hesselberg averaged manner (also known as Favre averaged). Any variable Ψ can be decomposed into

$$\Psi = \widehat{\Psi} + \Psi'' \tag{3.2}$$

with $\widehat{\Psi}$ being the Hesselberg mean and Ψ'' fluctuations from the latter. The Hesselberg mean is a density weighted time average and is formulated as

$$\widehat{\Psi} = \frac{\overline{\rho_a \Psi}}{\overline{\rho_a}}. \tag{3.3}$$

The overline denotes Reynolds averaged (classical time averaged) quantities and ρ_a is the density of dry air.

3.2.1. Gas Phase Chemistry in ART

For a chemical tracer Ψ the transport equation reads

$$\frac{\partial \overline{\rho_a} \widehat{\Psi}}{\partial t} = -adv + prod - loss + emiss, \tag{3.4}$$

as described by Weimer et al. (2017). Hence, the change in tracer concentration is determined by an advection (*adv*) and production (*prod*) term as well as the loss (*loss*) and emission (*emiss*) rate. A predictor-corrector method, as described by Seinfeld and Pandis (2016) and implemented by Weimer et al. (2017), is used to solve Eq. 3.4. The chemical production and the loss rate are determined based on a simplified OH-chemistry scheme. This chemistry scheme is extensively described by Weimer et al. (2017) and the references therein. The simplified OH-chemistry scheme assumes that the main sink for gaseous species in the atmosphere is their reaction with the OH radical. It is valid for gas phase reactions in the troposphere and UTLS region. The described chemistry scheme is relevant for the depletion of volcanic SO_2 and its transformation into H_2SO_4.
The production of OH in ICON-ART depends only on the photolysis of O_3 and the available concentrations of H_2O, CH_4, and CO. The photolysis rate is calculated by the Cloud-J module (Prather, 2015). Reasonable results of the simplified OH-chemistry scheme can be expected as long as the concentration of CH_4 is above a threshold of 1 ppmv. This threshold is reached at altitudes that are clearly above the tropopause (Weimer et al., 2017).

3.2.2. Aerosols in ART

The transport of aerosols in ICON-ART is slightly more complex compared to the transport of gaseous species.

As described in Sect. 2.3, a particle size distribution (for volcanic aerosols) consists of several size modes. Each of these modes is represented by a two-moment, modal formulation of the particle size distribution in ART. "Two-moment" denotes that two prognostic variables, number concentration and mass mixing ratio, are transported per mode. The Hesselberg averaged specific number concentration $\widehat{\Psi}_{0,l}$ represents the zeroth moment of the size distribution of mode l and the mass mixing ratio $\widehat{\Psi}_{3,l}$, derived from the third moment, respectively. They are given by

$$\widehat{\Psi}_{0,l} = \frac{\overline{\rho_a \frac{N_l}{\rho_a}}}{\overline{\rho_a}} = \frac{\overline{N_l}}{\overline{\rho_a}} \tag{3.5}$$

and

$$\widehat{\Psi}_{3,l} = \frac{\overline{\rho_a \frac{M_l}{\rho_a}}}{\overline{\rho_a}} = \frac{\overline{M_l}}{\overline{\rho_a}}. \tag{3.6}$$

The particle size distribution of aerosols in ART is described by log-normal distributions. The log-normal distribution for the mass specific number concentration and mass mixing ratio are given as functions of particle diameter d_p by

$$\psi_{0,l}(\ln d_p) = \frac{\widehat{\Psi}_{0,l}}{\sqrt{2\,\pi}\,\ln\sigma_l}\,\exp\left(-\frac{(\ln d_p - \ln d_{0,l})^2}{2\,\ln^2\sigma_l}\right) \tag{3.7}$$

and

$$\psi_{3,l}(\ln d_p) = \frac{\widehat{\Psi}_{3,l}}{\sqrt{2\,\pi}\,\ln\sigma_l}\,\exp\left(-\frac{(\ln d_p - \ln d_{3,l})^2}{2\,\ln^2\sigma_l}\right), \tag{3.8}$$

respectively. The shape of such a size distribution is defined by $\widehat{\Psi}_{0,l}$ ($\widehat{\Psi}_{3,l}$), the standard deviation σ_l, and the median diameter $d_{0,l}$ ($d_{3,l}$). With a fix standard deviation σ_l, the median diameter $d_{0,l}$ with respect to the mass specific number concentration can be derived from the two prognostic variables $\widehat{\Psi}_{0,l}$ and $\widehat{\Psi}_{3,l}$ by

$$d_{0,l} = \sqrt[3]{\frac{\widehat{\Psi}_{3,l}}{\frac{\pi}{6}\rho_p \exp\left(\frac{9}{2}\ln^2\sigma_l\right)\widehat{\Psi}_{0,l}}}\,. \tag{3.9}$$

The particle density is denoted by ρ_p. The median diameter $d_{3,l}$ with respect to the mass mixing ratio is given by

$$\ln d_{3,l} = \ln d_{0,l} + 3\ln^2\sigma_l. \tag{3.10}$$

Finally, the transport equations for the Hesselberg averaged specific number concentration and mass mixing ratio can be formulated as

$$\begin{aligned}\frac{\partial(\overline{\rho_a}\widehat{\Psi}_{0,l})}{\partial t} =& -\nabla\cdot(\widehat{\mathbf{v}}\overline{\rho_a}\widehat{\Psi}_{0,l}) - \nabla\cdot\overline{(\rho_a\mathbf{v}''\Psi''_{0,l})} \\ &- \frac{\partial}{\partial z}(\upsilon_{sed,0,l}\overline{\rho_a}\widehat{\Psi}_{0,l}) - W_{0,l} - Ca_{0,l} + Nu_{0,l} + E_{0,l}\end{aligned} \tag{3.11}$$

and

$$\begin{aligned}\frac{\partial(\overline{\rho_a}\widehat{\Psi}_{3,l})}{\partial t} =& -\nabla\cdot(\widehat{\mathbf{v}}\overline{\rho_a}\widehat{\Psi}_{3,l}) - \nabla\cdot\overline{(\rho_a\mathbf{v}''\Psi''_{3,l})} \\ &- \frac{\partial}{\partial z}(\upsilon_{sed,3,l}\overline{\rho_a}\widehat{\Psi}_{3,l}) - W_{3,l} - Ca_{3,l} + Nu_{3,l} + Co_{3,l} + E_{3,l}.\end{aligned} \tag{3.12}$$

Here, $\nabla\cdot(\widehat{\mathbf{v}}\overline{\rho_a}\widehat{\Psi}_{k,l})$ represents the advective term and $\nabla\cdot\overline{(\rho_a\mathbf{v}''\Psi''_{k,l})}$ the turbulent flux of the k^{th} moment of mode l. The wind vector is given by $\mathbf{v}$. The sedimentation velocity of the k^{th} moment of mode l is denoted by $\upsilon_{sed,k,l}$. $W_{k,l}$ represents the removal of particles due to wet deposition and $Ca_{k,l}$ due to coagulation. In ICON-ART wet deposition describes scavenging by raindrops below clouds. The coagulation term can be split into an intra- and inter-modal term which is discussed in more detail in Sect. 3.4. Nucleation of new particles $Nu_{k,l}$ only affects the Aitken mode ($l = Ait$). Condensation of gaseous matter on existing particles $Co_{3,l}$ is only a source term for the 3$^{\text{rd}}$ moment. $E_{k,l}$ denotes emissions into the k^{th} moment of mode l.

A more comprehensive description of the advection scheme can be found in Rieger (2017) or in the original publications of Miura (2007) and Colella and Woodward (1984). The parametrization of the turbulent flux is described by Rieger et al. (2015); Rieger (2017) and the references therein. Rieger et al. (2015) implemented a parametrization for the sedimentation velocity $\upsilon_{sed,k,l}$ following Riemer (2002) which is explained in detail in Rieger (2017). The parametrization of the wet deposition is described by Rieger (2017) and the references therein. Details on the parametrization of coagulation, condensation, and nucleation in ICON-ART are given in the following.

3.3. New Aerosol Modes in ICON-ART

This thesis is based on simulations run with the new aerosol dynamics module AERODYN in ICON-ART. The aerosol dynamic processes, condensation and coagulation, generate internally mixed aerosols. Therefore, a new set of modes was introduced compared to previous studies (Rieger et al., 2015; Gasch et al., 2017; Gruber et al., 2019; Hoshyaripour et al., 2019).

As introduced by Muser et al. (2020), the AERODYN module in ICON-ART includes 10 log-normal modes. These modes not only consider the different size ranges Aitken, accumulation, coarse, and giant, but also three different mixing states. There exist so-called soluble, insoluble, and mixed modes. The mixing states are distinguished based on their solubility with respect to water. A list of available

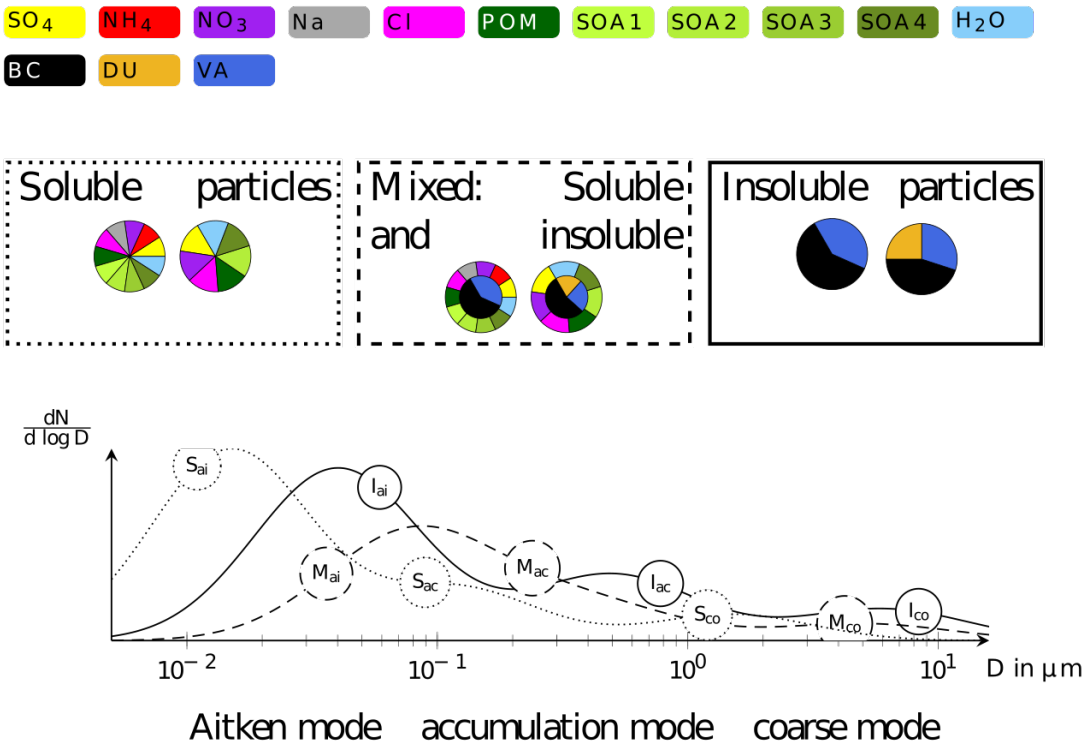

Figure 3.1: Chemical composition of the soluble (first row) and insoluble (second row) modes, mixing state of the modes (third row) and particle size distribution (giant mode is not shown). The dotted line represents a particle size distribution of soluble particles, the dashed line of mixed particles, and the solid line of insoluble particles, respectively. POM: primary organic matter, SOA: secondary organic aerosols, BC: black carbon. DU: desert dust, VA: volcanic ash. Upper panel adopted from Kaiser et al. (2014). In the current work, insoluble mode contains volcanic ash only while soluble mode contains only SO_4^{2-} and H_2O. Figure taken from Muser et al. (2020).

substances is displayed in the upper two rows of Fig. 3.1. Soluble substances comprise sulfate (SO_4^{2-}), ammonium (NH_4^+), nitrate (NO_3^-), sea salt components (Na^+ and Cl^-), primary organic matter, secondary organic aerosols, and water. Insoluble components are black carbon, dust, and volcanic ash. Mixed particles consist of an internally mixture of an insoluble core coated by soluble substances. Examples of arbitrary particles in different mixing states are shown in the three rectangular boxes of Fig. 3.1.

For each of the size distributions the prognostic number concentration together with the prognostic mass mixing ratios of the individual substances are computed. The standard deviation and median diameter are initialized in each simulation with values listed in Table 3.1. The median diameter of a mode can change due to aerosol dynamic processes, whereas the standard deviation is kept constant.

Single size distributions are superimposed to represent the whole range of particle sizes and mixing states. An example for the number concentration of 9 modes (giant mode not shown) is displayed in the lower panel of Fig. 3.1.

The AERODYN module and its processes were designed in a flexible way. This means, the user can decide which aerosol modes should participate in which processes. For the simulation of volcanic aerosol

Table 3.1: Median diameter with respect to 0^{th} moment and standard deviation of AERODYN modes at initialization. The variables are given for the 10 different modes as combination of their size and mixing state.

State/Size	Aitken		Accumulation		Coarse		Giant	
	$d_{0,l}$ [µm]	σ_l [−]	$d_{0,l}$ [µm]	σ_l [−]	$d_{0,l}$ [µm]	σ_l [−]	$d_{0,l}$ [µm]	σ_l [−]
Insoluble	0.01	1.7	0.2	2.0	2.0	2.2	12.0	2.0
Soluble	0.01	1.7	0.2	2.0	2.0	2.2	–	–
Mixed	0.01	1.7	0.2	2.0	2.0	2.2	–	–

Table 3.2: The coagulation matrix shows the participating aerosol modes and indicates the resulting mode. The abbreviations are: soluble (s), insoluble (i), mixed (m), Aitken (Ait), accumulation (acc), and coarse (coa).

	s_Ait	s_acc	i_acc	m_acc	i_coa	m_coa
s_Ait	s_Ait	s_acc	i_acc	m_acc	i_coa	m_coa
s_acc		s_acc	i_acc	m_acc	i_coa	m_coa
i_acc			i_acc	m_acc	i_coa	m_coa
m_acc				m_acc	i_coa	m_coa
i_coa					i_coa	m_coa
m_coa						m_coa

dispersion only a subset of the available substances and modes are necessary. Details about the considered species are given in Sect. 6.1.

3.4. Parametrization of Coagulation

The parametrization of the coagulation terms $Ca_{0,l}$ and $Ca_{3,l}$ of Eq. 3.11 and Eq. 3.12, respectively, is based on the work of Riemer (2002) and references therein (mainly Whitby et al., 1991). Here, only the basic equations are replicated.

Table 3.2 lists the modes that participate in coagulation in the scope of this thesis. Furthermore, the table displays the resulting mode in which the coagulation product is placed in. For example, when two insoluble accumulation mode particles coagulate, the resulting particle remains in the insoluble accumulation mode. An insoluble accumulation mode particle with a soluble Aitken mode particle results in an insoluble accumulation mode particle. Of course, the resulting particle will contain a higher soluble mass than before. In ICON-ART it is technically allowed to have soluble substances in an insoluble mode. Once the mass of soluble species reaches a specific threshold, the particles are shifted into the mixed mode, as described in detail in Sect. 3.6.

The two examples illustrate the concept of intra- and inter-modal coagulation. For intra-modal coagulation the resulting particle remains in the same mode. The new particle resulting of inter-modal coagu-

lation is assigned to the mode with the larger diameter. Hence, the coagulation rates for the zeroth and third moment in Eq. 3.11 and Eq. 3.12 consist of

$$Ca_{0,l} = Ca_{0,ll} + Ca_{0,lj} \tag{3.13}$$

$$Ca_{3,l} = Ca_{3,lj}\,. \tag{3.14}$$

The intra-modal coagulation term is denoted by $Ca_{k,ll}$ and the inter-modal by $Ca_{k,lj}$, respectively. Here, j indicates the coagulation partner to mode l. Depending on the mixing state of mode l and j and also on whether particles of mode j are larger or smaller than particles of l, the inter-modal terms can either be 0, source or sink terms for mode l. The zeroth moment generally decreases due to intra-modal coagulation or due to inter-modal coagulation. However, for the latter only in the partner mode of smaller particles. The zeroth moment of the larger mode stays constant. The third moment changes only due to inter-modal coagulation. In contrast to the zeroth moment, the third moment not only decreases in the smaller mode, but also increases in the larger mode. In the following, the parametrization of the coagulation is explained with a system of two modes, i and j. Here, I adapt the notation of Riemer (2002) with i and j indicating the coagulation partners of smaller and larger particles, respectively.

In ICON-ART the coagulation is restricted to the coagulation due to Brownian motion. For this case, Whitby et al. (1991) formulate the coagulation rate for log-normally distributed aerosol modes

$$\widetilde{Ca}_{0,ij} = \int_0^\infty \int_0^\infty \beta(d_i, d_j)\,\psi_{0,i}(d_i)\,\psi_{0,j}(d_j)\mathrm{d}d_i\mathrm{d}d_j\,. \tag{3.15}$$

Equivalent formulations can be written for $\widetilde{Ca}_{0,ii}$ and $\widetilde{Ca}_{3,ij}$. Note that $\widetilde{Ca}_{k,ij}$ is in units $\mathrm{m^k m^{-3} s^{-1}}$ which need to be converted before receiving $Ca_{k,ij}$. The coagulation coefficient β depends on the particle size. An analytical solution is only known for certain particle size ranges, as the motion of aerosol depends on the mean free path of the surrounding fluid.

Small aerosol particles can be of comparable size as the mean free path of the surrounding air. A quantity that is used to distinguish between different motion regimes is the dimensionless Knudsen number Kn. In this thesis the Knudsen number

$$\mathrm{Kn}_{gl} = \frac{2\lambda_{air}}{d_{0,l}} \tag{3.16}$$

is dependent on the median diameter $d_{0,l}$ of the particle size distribution with respect to the zeroth moment. Under standard conditions, the mean free path of air is $\lambda_{air} = 0.065$ µm. However, it gets larger at lower pressure levels (higher altitudes). Table 3.3 lists typical regimes with their corresponding Knudsen numbers. For $\mathrm{Kn} > 10$ aerosol particles are considered as free moving particles, comparable to air molecules. A small Knudsen number ($\mathrm{Kn} < 0.1$) indicates that the flow of the surrounding fluid around the aerosol particle can be considered as a continuum flow. Hence, the particle is suspended in the surrounding fluid.

Table 3.3: Regimes for different values of the Knudsen numbers.

Kn	Knudsen regime
> 10	free-molecular regime (fm)
$1 - 10$	transitional regime
$0.1 - 1$	near continuum regime (nc)
< 0.1	continuum regime

Whitby et al. (1991) solve Eq. 3.15 for the free-molecular (fm) and the near continuum regime (nc) separately. To cover the full size range, the harmonic mean of the two formulations is used. Using the harmonic mean for the full size range, proved to be fairly accurate. Riemer (2002) summarizes studies (e.g., Pratsinis, 1988; Kazakov and Frenklach, 1998) that show good agreement of this method compared to the reference method by Fuchs and Sutugin (1971). Additionally, the coagulation formulation of Whitby et al. (1991) is much faster than the one by Fuchs and Sutugin (1971). This makes it applicable for global transport models such as ICON-ART.

In the **near continuum** regime, the coagulation coefficient is given by

$$\beta_{\mathrm{nc}}(d_i, d_j) = 2\pi(D_i + D_j)(d_i + d_j)\,. \tag{3.17}$$

Here, D_l denotes the diffusion coefficient of particles in mode l with $l = i, j$. It depends on air temperature T, the dynamic viscosity μ of air, the Cunningham correction factor C_l, and the particle diameter d_l:

$$D_l = \frac{k_B T C_l}{3\pi\mu d_l}\,, \tag{3.18}$$

$$C_l \approx 1 + a_l \mathrm{Kn}_l\,, \tag{3.19}$$

$$\mathrm{Kn}_l = \frac{2\lambda_{air}}{d_l}\,. \tag{3.20}$$

The Boltzmann constant is denoted by k_B. The linearized Cunningham correction factor in Eq. 3.19 is approximated with a constant $a_l = 1.246$ following Binkowski and Shankar (1995). Knowing β_{nc}, the coagulation rate in the near continuum regime can be written as

$$\begin{aligned}
\widetilde{C}a^{\mathrm{nc}}_{0,ij} &= \int_0^\infty \int_0^\infty \beta_{\mathrm{nc}}(d_i, d_j)\,\psi_{0,i}(d_i)\,\psi_{0,j}(d_j)\,\mathrm{d}d_i\mathrm{d}d_j \\
&= \Psi_{0,i}\Psi_{0,j}\rho_a^2 K_{\mathrm{nc}} \left[2 + a_i \mathrm{Kn}_{gi} \left(e^{\frac{4}{8}\ln^2(\sigma_i)} + \frac{d_{0,j}}{d_{0,i}} e^{\frac{16}{8}\ln^2(\sigma_i)} e^{\frac{4}{8}\ln^2(\sigma_j)} \right) \right. \\
&\qquad + a_j \mathrm{Kn}_{gj} \left(e^{\frac{4}{8}\ln^2(\sigma_j)} + \frac{d_{0,i}}{d_{0,j}} e^{\frac{16}{8}\ln^2(\sigma_j)} e^{\frac{4}{8}\ln^2(\sigma_i)} \right) \\
&\qquad \left. + \left(\frac{d_{0,i}}{d_{0,j}} + \frac{d_{0,j}}{d_{0,i}} \right) e^{\frac{4}{8}\ln^2(\sigma_j)} e^{\frac{4}{8}\ln^2(\sigma_i)} \right]\,.
\end{aligned} \tag{3.21}$$

Here, the factor K_{nc} is defined as

$$K_{\mathrm{nc}} = \frac{2k_B T}{3\mu}. \tag{3.22}$$

The rates for intra-modal coagulation, $\widetilde{Ca}^{\mathrm{nc}}_{0,ii}$ and $\widetilde{Ca}^{\mathrm{nc}}_{0,jj}$, are derived analogously.
The coagulation rate for the third moment in the near continuum regime is given by

$$\begin{aligned}
\widetilde{Ca}^{\mathrm{nc}}_{3,ij} &= \int_0^\infty \int_0^\infty d_i^3 \beta_{\mathrm{nc}}(d_i,d_j)\psi_{0,i}(d_i)\psi_{0,j}(d_j)\mathrm{d}d_i\mathrm{d}d_j \\
&= \Psi_{0,i}\Psi_{0,j}\rho_a^2 K_{\mathrm{nc}} d_{0,i}^3 \left[2e^{\frac{36}{8}\ln^2(\sigma_i)} + a_i \mathrm{Kn}_{gi} \left(e^{\frac{16}{8}\ln^2(\sigma_i)} + \frac{d_{0,j}}{d_{0,i}} e^{\frac{4}{8}\ln^2(\sigma_i)} e^{\frac{4}{8}\ln^2(\sigma_j)} \right) \right. \\
&\quad + a_j \mathrm{Kn}_{gj} \left(e^{\frac{36}{8}\ln^2(\sigma_i)} e^{\frac{4}{8}\ln^2(\sigma_j)} + \frac{d_{0,i}}{d_{0,j}} e^{\frac{64}{8}\ln^2(\sigma_i)} e^{\frac{16}{8}\ln^2(\sigma_j)} \right) \\
&\quad \left. + \frac{d_{0,j}}{d_{0,i}} e^{\frac{16}{8}\ln^2(\sigma_i)} e^{\frac{4}{8}\ln^2(\sigma_j)} + \frac{d_{0,i}}{d_{0,j}} e^{\frac{64}{8}\ln^2(\sigma_i)} e^{\frac{4}{8}\ln^2(\sigma_j)} \right].
\end{aligned} \tag{3.23}$$

In the **free-molecular** regime, the coagulation coefficient has a more complex form (Riemer, 2002, and the references therein). To enable an analytical integration of the coefficient, an approximation is used. The approximation of the coagulation coefficient is given by

$$\beta_{\mathrm{fm}}(d_i,d_j) = \sqrt{\frac{6k_B T}{\rho_{p,i}+\rho_{p,j}}} \left(\sqrt{d_i} + 2\frac{d_j}{\sqrt{d_i}} + \frac{d_j^2}{d_i^{\frac{3}{2}}} + \frac{d_i^2}{d_j^{\frac{3}{2}}} + 2\frac{d_i}{\sqrt{d_j}} + \sqrt{d_j} \right). \tag{3.24}$$

The coefficient depends on the particle's density ρ_p. In ICON-ART the particle density can differ between coagulation partner i and j. That is why the average density is used here. With the given coagulation coefficient the coagulation rate in the free-molecular regime results to

$$\begin{aligned}
\widetilde{Ca}^{\mathrm{fm}}_{0,ij} &= \int_0^\infty \int_0^\infty \beta_{\mathrm{fm}}(d_i,d_j)\psi_{0,i}(d_i)\psi_{0,j}(d_j)\mathrm{d}d_i\mathrm{d}d_j \\
&= \Psi_{0,i}\Psi_{0,j}\rho_a^2 K_{\mathrm{fm}} b_0 \sqrt{d_{0,i}} \left[e^{\frac{1}{8}\ln^2(\sigma_i)} + \sqrt{\frac{d_{0,j}}{d_{0,i}}} e^{\frac{1}{8}\ln^2(\sigma_j)} \right. \\
&\quad + 2\frac{d_{0,j}}{d_{0,i}} e^{\frac{1}{8}\ln^2(\sigma_i)} e^{\frac{4}{8}\ln^2(\sigma_j)} + \frac{d_{0,j}^2}{d_{0,i}^2} e^{\frac{9}{8}\ln^2(\sigma_i)} e^{\frac{16}{8}\ln^2(\sigma_j)} \\
&\quad \left. + \left(\sqrt{\frac{d_{0,i}}{d_{0,j}}} \right)^3 e^{\frac{16}{8}\ln^2(\sigma_i)} e^{\frac{9}{8}\ln^2(\sigma_j)} + 2\sqrt{\frac{d_{0,i}}{d_{0,j}}} e^{\frac{4}{8}\ln^2(\sigma_i)} e^{\frac{1}{8}\ln^2(\sigma_j)} \right].
\end{aligned} \tag{3.25}$$

Here, the factor K_{fm} is defined as

$$K_{\mathrm{fm}} = \sqrt{\frac{6k_B T}{\rho_{p,i}+\rho_{p,j}}}. \tag{3.26}$$

For the third moment, the coagulation rate in the free-molecular regime is written as

$$\begin{aligned}\widetilde{Ca}^{\mathrm{fm}}_{3,ij} &= \int_0^\infty \int_0^\infty d_i^3 \beta_{\mathrm{fm}}(d_i,d_j)\psi_{0,i}(d_i)\psi_{0,j}(d_j)\mathrm{d}d_i\mathrm{d}d_j \\ &= \Psi_{0,i}\Psi_{0,j}\rho_a^2 K_{\mathrm{fm}} b_3 (d_{0,i})^{\frac{7}{2}} \left[e^{\frac{49}{8}\ln^2(\sigma_i)} + \sqrt{\frac{d_{0,j}}{d_{0,i}}} e^{\frac{36}{8}\ln^2(\sigma_i)} e^{\frac{1}{8}\ln^2(\sigma_j)} \right. \\ &\quad + 2\frac{d_{0,j}}{d_{0,i}} e^{\frac{25}{8}\ln^2(\sigma_i)} e^{\frac{4}{8}\ln^2(\sigma_j)} + \frac{d_{0,j}^2}{d_{0,i}^2} e^{\frac{9}{8}\ln^2(\sigma_i)} e^{\frac{16}{8}\ln^2(\sigma_j)} \\ &\quad \left. + \left(\sqrt{\frac{d_{0,i}}{d_{0,j}}}\right)^3 e^{\frac{100}{8}\ln^2(\sigma_i)} e^{\frac{9}{8}\ln^2(\sigma_j)} + 2\sqrt{\frac{d_{0,i}}{d_{0,j}}} e^{\frac{64}{8}\ln^2(\sigma_i)} e^{\frac{1}{8}\ln^2(\sigma_j)} \right] .\end{aligned} \tag{3.27}$$

Values for the two factors b_0 and b_3 are given by Whitby et al. (1991). For inter-modal coagulation the values are $b_0 = 0.9$ and $b_3 = 0.9$, for intra-modal $b_0 = 0.8$. Again, the rates for intra-modal coagulation, $\widetilde{Ca}^{\mathrm{fm}}_{0,ii}$ and $\widetilde{Ca}^{\mathrm{fm}}_{0,jj}$, are derived analogously.
As stated earlier, the coagulation rate for all Knudsen regimes is approximated by the harmonic mean. This results in

$$\widetilde{Ca}_{0,ij} = \frac{\widetilde{Ca}^{\mathrm{nc}}_{0,ij}\,\widetilde{Ca}^{\mathrm{fm}}_{0,ij}}{\widetilde{Ca}^{\mathrm{nc}}_{0,ij} + \widetilde{Ca}^{\mathrm{fm}}_{0,ij}} \tag{3.28}$$

$$\widetilde{Ca}_{3,ij} = \frac{\widetilde{Ca}^{\mathrm{nc}}_{3,ij}\,\widetilde{Ca}^{\mathrm{fm}}_{3,ij}}{\widetilde{Ca}^{\mathrm{nc}}_{3,ij} + \widetilde{Ca}^{\mathrm{fm}}_{3,ij}} \tag{3.29}$$

and can be done for $\widetilde{Ca}_{0,ii}$ and $\widetilde{Ca}_{0,jj}$ analogously. Together with Eq. 3.13 and Eq. 3.14 the coagulation rate for the zeroth $\widetilde{Ca}_{0,l}$ and third moment $\widetilde{Ca}_{3,l}$ of mode l are determined. In ICON-ART, these are transformed to

$$Ca_{0,l} = \frac{1}{\rho_a}\widetilde{Ca}_{0,l} \tag{3.30}$$

$$Ca_{3,l} = \frac{\rho_{p,l}}{\rho_a}\widetilde{Ca}_{3,l}\,. \tag{3.31}$$

3.5. From Gas to Particles

The interaction of gaseous species with aerosols in ICON-ART is modeled in three different routines. A gas–particle phase equilibrium is determined by the ISORROPIA II module (Sect. 3.5.1). Furthermore, the condensation of H_2SO_4 on particles (Sect. 3.5.2) and the nucleation of H_2SO_4 to sulfate particles (Sect. 3.5.3) are taken into account in ICON-ART.

3.5.1. Coupling of the ISORROPIA II Module for Gas – Particle Partitioning

Muser et al. (2020) coupled the ISORROPIA II model by Fountoukis and Nenes (2007) to ICON-ART. ISORROPIA II has been coupled to general circulation models before (e.g., Guth et al., 2016; Deetz

et al., 2018). ISORROPIA II is an extension of ISORROPIA by Nenes et al. (1998). For simplification, in this thesis the term ISORROPIA always refers to ISORROPIA II (Fountoukis and Nenes, 2007) if not stated otherwise.
ISORROPIA computes the gas–particle partitioning based on the thermodynamic equilibrium state. It can be applied for inorganic tropospheric K^+ - Ca^{2+} - Mg^{2+} - NH_4^+ - Na^+ - SO_4^{2-} - NO_3^- - Cl^- - H_2O aerosols. The equilibrium state for these species is determined in gas, liquid, and solid phase.
Besides the thermodynamic equilibrium, several assumptions are made as stated in Fountoukis and Nenes (2007). For this work, two should be mentioned, as they are relevant for volcanic aerosols.

1. Sulfuric acid has a very low vapor pressure. Hence, it remains in the aerosol phase once it condensed on existing or nucleated to new particles.

2. For sulfate rich cases, $NH_{3(g)}$, $NO_{3(aq)}$, and $Cl_{(aq)}$ are assumed to not perturb the equilibrium significantly.

ISORROPIA is usually applied for gas-particle partitioning in the troposphere and lower stratosphere up to around 20 km altitude (C. Fountoukis, personal communication, 26 August 2021).

3.5.2. Parametrization of Condensation

Condensation of gaseous species onto existing aerosol particles leads to a growth of these particles. Hence, condensation influences the third moment or mass mixing ratio of the particle size distribution. As no new particles are generated, the zeroth moment is not affected. In ICON-ART, only a parametrization for the condensation of sulfuric acid is used. Other substances are treated by the ISORROPIA module (see Sect. 3.5.1). The parametrization of the condensation of sulfuric acid is based on Whitby et al. (1991) and was adapted from Riemer (2002). The condensation rate of the third moment of mode l is given by

$$\widetilde{Co}_{3,l} = \frac{6}{\pi}\chi_T \int_0^\infty \chi(d_l)\,\psi_{0,l}(d_l)\,\mathrm{d}d_l = \frac{6}{\pi}\chi_T I_l\,. \tag{3.32}$$

It can be separated into a term χ_T that is independent of the particle size and a size dependent term $\chi(d)$, respectively. The integral is abbreviated by I_l. An expression for χ_T can be found in literature (e.g., Riemer, 2002). The size dependent χ is formulated differently in the near continuum and the free-molecular regime:

$$\chi_{\mathrm{nc}}(d_l) = 2\pi D_{\mathrm{H_2SO_4}} d_l\,, \tag{3.33}$$

$$\chi_{\mathrm{fm}}(d_l) = \frac{\pi\alpha\bar{c}}{4} d_l^2\,. \tag{3.34}$$

In the near continuum regime, the diffusion coefficient of sulfuric acid $D_{\mathrm{H_2SO_4}}$ is needed. In the free-molecular regime, the condensation rate depends on the accommodation coefficient α and the mean

molecular velocity $\bar{c} = \sqrt{\frac{8\Re T}{\pi M_{H_2SO_4}}}$. $\Re$ denotes the universal gas constant and $M_{H_2SO_4}$ the molar mass of H_2SO_4. With these two formulations (Eq. 3.33 and 3.34) the integral I_l can be evaluated for the two regimes separately:

$$I_l^{\mathrm{nc}} = 2\pi D_{H_2SO_4} M_{1,l} \tag{3.35}$$

$$I_l^{\mathrm{fm}} = \frac{\pi \alpha \bar{c}}{4} M_{2,l}\,. \tag{3.36}$$

$M_{k,l}$ denotes the k-th moment of the particle size distribution. The integral I_l which is valid for all Knudsen regimes is composed of the harmonic mean

$$I_l = \frac{I_l^{\mathrm{nc}} I_l^{\mathrm{fm}}}{I_l^{\mathrm{nc}} + I_l^{\mathrm{fm}}}\,. \tag{3.37}$$

With this, the condensation rate of the third moment is formulated as

$$\widetilde{Co}_{3,l} = \frac{6}{\pi}\chi_T I_l = \frac{6}{\pi}\chi_T \frac{I_l^{\mathrm{nc}} I_l^{\mathrm{fm}}}{I_l^{\mathrm{nc}} + I_l^{\mathrm{fm}}}\,. \tag{3.38}$$

To eliminate χ_T, it is assumed that the condensation is fast compared to the production of gaseous H_2SO_4. Therefore, an equilibrium state is reached in which the production rate of gaseous H_2SO_4 equals the total condensation rate

$$\widetilde{Co}_3 = \sum_l \widetilde{Co}_{3,l} = \dot{M}_3\,. \tag{3.39}$$

In this case, $\dot{M}_3$ is the production rate of the third moment of gaseous H_2SO_4. This assumption allows the formulation of the dimensionless coefficient

$$\Omega_l = \frac{\widetilde{Co}_{3,l}}{\widetilde{Co}_3} = \frac{\widetilde{Co}_{3,l}}{\dot{M}_3} = \frac{I_l}{\sum_l I_l}\,. \tag{3.40}$$

This coefficient Ω_l does not depend on χ_T anymore. Hence, the condensation rate

$$\widetilde{Co}_{3,l} = \dot{M}_3 \Omega_l \tag{3.41}$$

only depends on the integral I_l and the production rate of sulfuric acid. In ICON-ART the condensation rate is needed for the mass mixing ratio. It is given by

$$Co_{3,l} = \frac{\pi}{6}\frac{\rho_{H_2SO_4}}{\rho_a}\dot{M}_3 \Omega_l\,. \tag{3.42}$$

The production rate of the third moment of gaseous H_2SO_4 is not available in ICON-ART. That is why the production rate is approximated by the mass mixing ratio $c_{H_2SO_4}$ and the model time step Δt resulting in

$$Co_{3,l} = \frac{c_{H_2SO_4}}{\Delta t}\Omega_l \,. \tag{3.43}$$

3.5.3. Parametrization of Nucleation

The parametrization of the nucleation of sulfate particles follows the formulation of Kerminen and Wexler (1995). A detailed summary can be found in Riemer (2002). Kerminen and Wexler (1995) formulate a critical concentration c_{crit} of H_2SO_4. In case of higher atmospheric H_2SO_4 concentrations new particles nucleate. The critical concentration is given by the empirical relation

$$c_{crit} = 0.16 \exp\left(0.1T - 3.5\frac{RH}{100} - 27.7\right) . \tag{3.44}$$

The temperature T is in K and the relative humidity RH in percent. The result (c_{crit}) is given in µg m^{-3}. Eq. 3.44 is based on measurements taken by Jaecker-Voirol and Mirabel (1989). For $c_{H_2SO_4} > \frac{c_{crit}}{\rho_a}$ the nucleation rate in ICON-ART is determined by

$$Nu_{3,Ait} = \frac{c_{H_2SO_4} - \frac{c_{crit}}{\rho_a}}{\Delta t} \tag{3.45}$$

Freshly nucleated sulfate particles are assigned to the Aitken mode of soluble particles. As the introduced parametrization only returns a rate for the nucleation mass, the resulting number concentration needs to be calculated based on an assumed size distribution. Therefore, in ICON-ART it is assumed that freshly nucleated particles follow a size distribution with $d_{0,sol\_Ait} = 0.01$ µm and $\sigma_{sol\_Ait} = 1.7$. These values are close to observed ones such as $d_{0,nucl} \approx 0.01$ µm and $\sigma_{nucl} \approx 1.6$ (Whitby, 1978).

3.6. Shifting Particles to Mixed Mode

Coagulation, condensation, and ISORROPIA bring soluble substances on insoluble particles. Once more and more soluble mass accumulates on the insoluble core, the physico-chemical properties of the particle change. The resulting particles are internally mixed which are represented by the mixed modes in ICON-ART. Shifting particles from an insoluble mode to the corresponding mixed mode follows the implementation of Riemer (2002). Once the mass of soluble substances reaches a threshold of 5% of the total aerosol mass in this mode, the mode is shifted to the mixed mode. This assumption is based on Weingartner et al. (1997). Their measurements showed that hydrophobic (insoluble) soot particles change the hygroscopic properties once a minimum of soluble material is present on the surface of these soot particles.

3.7. Aerosol–Radiation Interaction in ICON-ART

In ICON-ART, the Rapid Radiative Transfer Model (RRTM) by Mlawer et al. (1997) is used to compute the radiative fluxes in the model atmosphere. A detailed description about the coupling of ART with RRTM is given by Gasch (2016), Gasch et al. (2017), and Walter (2019). The RRTM model computes the radiative fluxes for 30 spectral bands. These bands cover wavelengths between $0.2 - 1000$ µm. Fourteen of these 30 bands represent short wave radiation with wavelengths up to 3.846 µm. The other 16 cover long wave radiation (Morcrette et al., 2008).

To account for prognostic ART aerosol in the radiative budget we need to know the optical properties of the particles in form of extinction coefficient, single scattering albedo and asymmetry parameter, as described in Sect. 2.5. Additionally, the mass mixing ratio of the particles $\Psi_{3,l}$ is needed. For calculations in ICON-ART it is more convenient having the extinction coefficient (Eq. 2.6) formulated not with respect to the distance between two points, but with respect to the aerosol mass between these two points. Therefore, the mass extinction coefficient

$$k_e = \frac{\beta_e}{\rho_p} \tag{3.46}$$

can be derived from β_e with the density ρ_p of the particle. So far, we assumed that all particles that interact with radiation have the same size and consist of the same substance. In ICON-ART, however, we account for different particle sizes and mixing states. Therefore, for each mode l an extinction coefficient $\beta_{e,l}$ needs to be determined. The total extinction coefficient sums up to

$$\beta_e = \sum_l \beta_{e,l} = \sum_l \rho_{p,l} k_{e,l} \,. \tag{3.47}$$

Thus, in ICON-ART the mass extinction coefficient $k_{e,l}$ for each mode l is used. Also the mode specific single scattering albedo ω_l and asymmetry parameter g_l are needed. In the scope of this work, I assume that the volcanic aerosol particles are spherical. With this assumption the optical properties can be computed following classical Mie theory by

$$Q_e = \frac{2}{x^2} \sum_{n=1}^{\infty} (2n+1)\,\mathrm{Re}\,(a_n + b_n)\,, \tag{3.48}$$

$$Q_s = \frac{2}{x^2} \sum_{n=1}^{\infty} \left(|a_n|^2 + |b_n|^2\right), \tag{3.49}$$

$$g = \frac{4}{x^2 Q_s} \sum_{n=1}^{\infty} (2n+1) \left[\frac{n(n+2)}{n+1}\mathrm{Re}\left(a_n a_{n+1}^* + b_n b_{n+1}^*\right) + \frac{2n+1}{n(n+1)}\mathrm{Re}\left(a_n b_n^*\right)\right] \tag{3.50}$$

as stated by Boucher (2015).

The quantities a_n and b_n are Mie scattering coefficients which are dependent on particle diameter d_p, wavelength λ, and the complex refractive index B_λ. They are complex numbers and composed of Riccati-Bessel functions. The complex conjugate of a_n and b_n are denoted by a_n^* and b_n^*, respectively. Expressions

for a_n and b_n can be found in Boucher (2015). The nondimensional size parameter is denoted by x and was defined earlier in Eq. 2.12.

Knowing the extinction efficiency, the volume specific extinction coefficient β_e of a log-normal mode l is determined by

$$\beta_e(l,\lambda,B_\lambda) = \int_0^\infty \frac{\pi d_p^2}{4} Q_e(d_p,\lambda,B_\lambda)\psi_{0,l}(d_p)dd_p\,. \tag{3.51}$$

Analogously, the volume specific scattering coefficient β_s is determined. The mass specific extinction coefficient k_e is derived by combining Eq. 2.5 and Eq. 3.46

$$k_e(l,\lambda,B_\lambda) = \frac{\int_0^\infty \frac{\pi}{4} d_p^2 Q_e \psi_{0,l} dd_p}{\int_0^\infty \psi_{3,l} dd_p} \tag{3.52}$$

$$= \frac{\int_0^\infty \frac{\pi}{4} d_p^2 Q_e \psi_{0,l} dd_p}{\int_0^\infty \rho_p \left[\frac{\pi}{6} d_p^3\right] \psi_{0,l} dd_p}\,. \tag{3.53}$$

In this work, a Mie code for coated spheres was used to derive the optical properties of volcanic aerosols. The code has been developed by Mätzler (2002) and Bond et al. (2006) whose work is based on Bohren and Huffman (1983). As these Mie calculations are computationally expensive, they must be run offline. The results for each mode l for each of the 30 RRTM wave bands are stored in form of look-up tables. In order to calculate the optical properties of each aerosol mode, the composition of the particles and their diameter are needed. As for each mode only one set of optical properties is determined, the composition and the diameter should be representative for this mode in the whole volcanic cloud. These representative values are derived from literature, ICON-ART simulations on the Pinatubo eruption 1991 (Muth, 2019), and own simulations on the Eyjafjallajökull eruption 2010.

The composition of the particles defines the refractive indices. In this work, insoluble particles are treated as spherical ash particles with no coating. Soluble particles are treated as a volume averaged mixture of water and sulfate. Particles in the mixed modes are considered as ash particles coated with a water-sulfate shell. The Mie calculations are done with wavelength dependent refractive indices of volcanic ash (Walter, 2019), water, and sulfuric acid (Gordon et al., 2017). Therefore, soluble particles and the shell of mixed particles are assumed to consist of a 50% sulfate-water mixture. This assumption is based on Gordon et al. (2017) and measurements of Rosen (1971). Rosen (1971) measured a sulfuric acid content of 75% in stratospheric aerosols. However, volcanic aerosols in this study reside also in the troposphere where lower H_2SO_4 contents can be expected. Also the Pinatubo and Eyjafjallajökull

Table 3.4: Particle diameter and coating ratio of each mode for the calculation of the optical properties. The abbreviations are: soluble (s), insoluble (i), mixed (m), Aitken (Ait), accumulation (acc), and coarse (coa).

mode	s_Ait	s_acc	i_acc	m_acc	i_coa	m_coa	giant
d_t [µm]	0.03	0.12	0.644	0.08	3.454	2.00	12.0
coating ratio	0	0	0	0.2	0	0.2	0

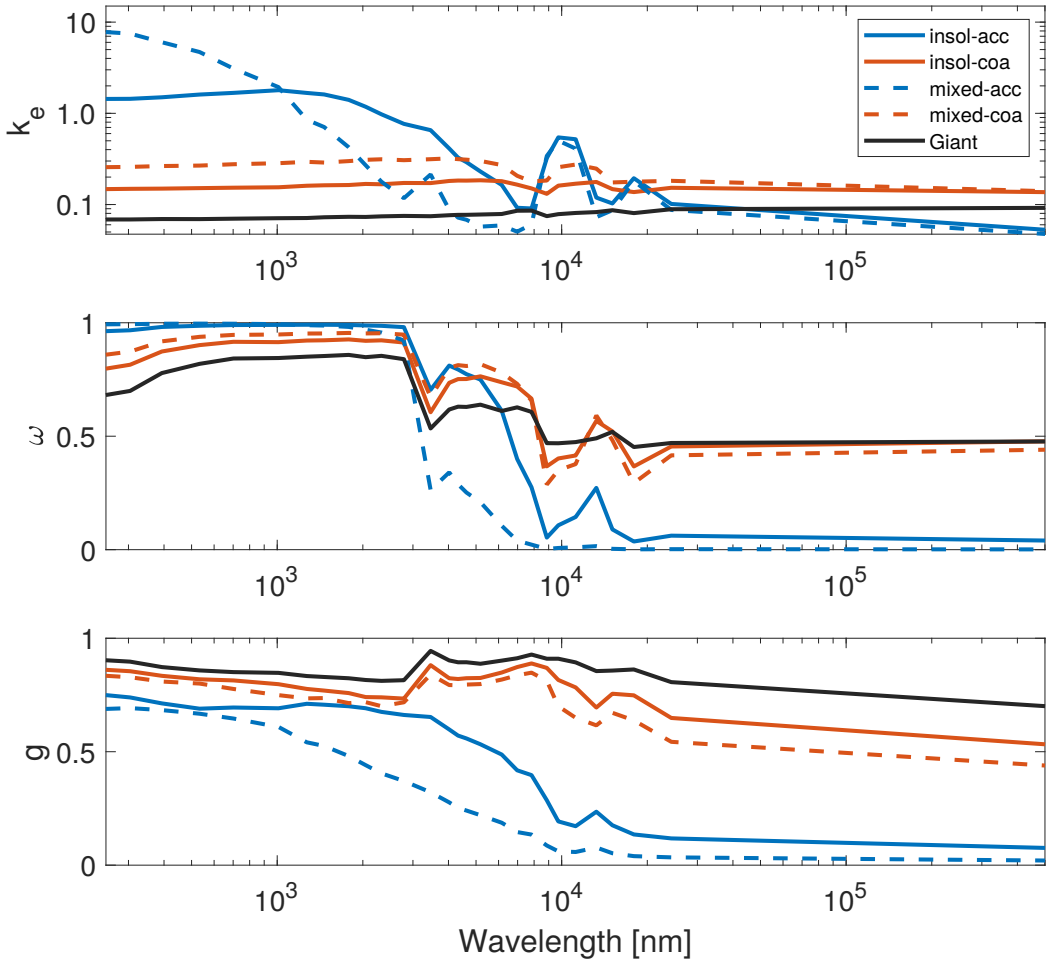

Figure 3.2: Optical properties of ash containing modes at different wavelengths. Upper panel shows the extinction coefficient k_e, central panel the single scattering albedo ω, and the lower panel the asymmetry parameter g. Solid lines indicate insoluble modes and dashed lines mixed modes, respectively. (Muser et al., 2020)

eruption simulations indicate a lower sulfate content in soluble particles. That is why the lower H_2SO_4 content of 50% is assumed.

For each of the aerosol modes, the optical properties are determined for one representative diameter. Values for this diameter are listed in Table 3.4. These values are derived from ICON-ART simulations on the Pinatubo eruption (Muth, 2019).

The coating ratio of mixed particles is here defined as the fraction of the shell diameter to the total particle diameter. It has been determined analogously to the representative diameter, by evaluation of the Pinatubo simulation (Muth, 2019). The values are given in Table 3.4.

The results of the Mie calculations are visualized in Fig. 3.2. It displays the optical properties of ash containing modes at different wavelengths, as they are used for simulations in this thesis. The full set of look-up tables with the optical properties of aerosol modes for each RRTM waveband are summarized in

Appendix A. The influence of the particle size on the extinction coefficient is visible in the upper panel of Fig. 3.2. Especially for short wavelengths (in the visible and near IR range), smaller particles lead to significantly higher k_e. For longer wavelengths differences become less pronounced. Furthermore, it becomes evident that the mixing state influences the extinction coefficient. Coated coarse mode ash particles have slightly higher k_e than uncoated ash. For accumulation mode ash particles the difference between coated and uncoated particles is more pronounced, with a higher extinction for coated particles in the visible range and a lower extinction in the near IR range.

To interpret the aerosol–radiation interaction, the single scattering albedo ω is also of interest. Low values for ω indicate that absorption is the main driver for extinction. Absorbing particles heat up on incident radiation and, consequently, also heat the surrounding air. The middle panel in Fig. 3.2 shows that coated accumulation mode ash particles are significantly more absorbing in the near and mid IR range compared to uncoated.

The asymmetry parameter g in the lower panel of Fig. 3.2 is somewhat lower for coated particles compared to uncoated. As g is closer to 0, this results in a more uniform scattering for coated particles. The slightly different scattering behavior won't affect the budget of radiation fluxes in ICON-ART, but is relevant for a comparison with backscatter measurements by remote sensing.

The assumptions made for the determination of the optical properties of aerosol modes can introduce errors into the ICON-ART simulations. That is why the deficiencies of these assumptions are shortly mentioned here.

The complex refractive index for volcanic ash depends in the mineralogy of the particles. Laboratory measurements can give values for ash of historic events. The values that are used here, are taken from Walter (2019) and the references therein. However, the mineralological composition of the volcanic ash of the Raikoke eruption might differ from these historic ones.

Furthermore, particles are assumed to be spherical. Liquid particles such as sulfate aerosols fulfill this assumption, but it is generally not true for volcanic ash. However, the coating of soluble substances on ash particles leads to a more spherical shape which justifies the assumption. In order to be consistent for all aerosol modes, volcanic ash is also treated as spherical particles. Also, randomly oriented non-spherical particles can justify the spherical assumption if only the radiation heating is of interest. In that case, only minor errors can be expected to be introduced (Mishchenko et al., 1995, 1997).

Last, but not least, a fix particle diameter and a fix mixing state is assumed. However, both can differ significantly within the volcanic cloud and over time. Due to particle aging, particle diameters tend to increase over time. These larger particles then tend to sediment faster. This leads to a vertical separation of smaller and larger particles, also within one mode.

4. Observational Data

During and after the Raikoke eruption in 2019, several satellite instruments were in place to sense the volcanic cloud. In this section some details about the instruments are explained. These explanations are taken from *Particle aging and aerosol–radiation interaction affect volcanic plume dispersion: evidence from the Raikoke 2019 eruption* published in *Atmospheric Chemistry and Physics* (Muser et al., 2020). The text contributions for the observational data were mainly provided by co-authors of Muser et al. (2020). The contributing authors are indicated in each of the following sections with the corresponding text highlighted in quotation marks.

4.1. SO_2 Measurement by TROPOMI

The TROPOMI data was provided by Sandra Wallis who contributed to Muser et al. (2020): "The spread of the SO_2 plume ejected by the Raikoke eruption in June 2019 as well as the amount of released SO_2 mass was investigated by analyzing SO_2 total vertical column densities from the hyperspectral nadir-viewing TROPOspheric Monitoring Instrument (TROPOMI) aboard the Sentinel-5 Precursor satellite. TROPOMI provides daily global coverage completing 14.5 orbits every day (van Kempen et al., 2019) with a pixel size of 7 km $\times$ 3.5 km (Theys et al., 2019). TROPOMI SO_2 (daylight only) offline level 2 data were downloaded from the Copernicus website (https://s5phub.copernicus.eu). The total vertical SO_2 column densities used, assume a SO_2 profile described by a 1 km thick box at 15 km altitude to account for explosive volcanic eruptions (Theys et al., 2017).

A self-defined geographic grid including the area from 30° N – 75° N and 135° E – 120° W with a resolution of $0.1^\circ \times 0.1^\circ$ was created. The SO_2 cloud expansion for every TROPOMI orbit was visualized by first averaging all vertical SO_2 column densities inside a single grid segment and multiplying the result by the SO_2 molar mass in order to obtain a mass loading in units of $\mathrm{g\,m^{-2}}$. Only data with a quality value larger than 0.5 (as recommended in the TROPOMI product user manual) and total vertical column density with values less than 1000 $\mathrm{mol\,m^{-2}}$ were used.

The SO_2 mass loading for each grid segment was multiplied subsequently with the associated grid segment area to obtain the SO_2 mass in units of g. The total SO_2 mass for the observed area was determined for the observed area over time periods of approximately 24 h, i.e., by averaging batches of 14 consecutive orbits for every single grid segment. Finally, the mass is summed up over the entire grid. The described data averaging was applied because consecutive orbits partially overlap. This method suggests a total emitted SO_2 mass of $(1.37 \pm 0.07) \times 10^9$ kg over the course of the Raikoke eruption 2019. Since

the air mass factor used in the retrieval of the vertical column densities depends on the SO_2 vertical distribution, the choice of the assumed SO_2 profiles seems to be the most important source of error. It remains, however, a non-trivial challenge to estimate the associated uncertainty of the SO_2 mass calculation. The uncertainty stated above reflects the average absolute difference between the SO_2 mass calculated from an assumed SO_2 profile peak in 15 km and 7 km altitude, respectively. SO_2 masses from 20 June, 16:41 UTC to 6 July, 10:08 UTC were included in the averaging."

4.2. Volcanic Cloud Height Measurement by OMPS-LP

The OMPS-LP data was provided by Elizaveta Malinina and Alexei Rozano who contributed to Muser et al. (2020): "The volcanic cloud top height on 22 June 2019, was determined by visual analysis of the stratospheric aerosol extinction coefficient profiles from the OMPS-LP instrument. Here, the aerosol extinction coefficient product at 869 nm (V1.0.9) retrieved at the University of Bremen is used. The OMPS aerosol extinction coefficient was retrieved on a 1 km grid from 10.5 to 33.5 km with the algorithm adapted from the SCIAMACHY V1.4 (Rieger et al., 2018). The retrieval is done under the assumption that stratospheric aerosol is represented by spherical sulfuric droplets with a unimodal log–normal particle size distribution ($r_{med} = 80$ nm, $\sigma = 1.6$). Due to uncertainties in pointing and vertical sampling the measurement error is estimated with ± 0.7 km. Detailed information on the retrieval algorithm can be found in Malinina (2019) and Malinina et al. (2021). Here, it should be noted that the evaluation of the plume top height from OMPS-LP was possible only on the 22 June 2019. On that day, the instrument was passing right above the Raikoke island, and the plume was very localized. Thus, the increase in the aerosol extinction coefficient associated with the eruption was large and obvious. This large increase was a result of a vast amount of ash released with the eruption. In the following days, when the plume started to spread over the North Pacific, the core of the fresh plume is not hit by the OMPS-LP instrument sampling anymore. Slightly perturbed aerosol extinction observed in transition regions has a similar magnitude as that from interfering events, e.g., the aerosol transport from the Ambae eruption that occurred 11 months earlier, and thus cannot be attributed exclusively to the Raikoke eruption. For this reason, the OMPS-LP measurements in transition regions were excluded from the consideration."

4.3. Ash and SO_2 Measurement by AHI

The AHI data was provided by Fred J. Prata who contributed to Muser et al. (2020): "Himawari-8 is a geostationary satellite platform operated by the Japanese Space Agency (JAXA) in collaboration with the Japanese Meteorological Agency (JMA) carrying the 16 band visible and infrared Advanced Himawari Imager (AHI). Data are acquired every 10 minutes over the Earth's disc covering a circular field of view of approximately 70 degrees, centred at the equator and $\sim 140^\circ$ E longitude. Further details of the orbit, instrument, duty cycles, image geolocation, and data calibration can be found on the JAXA/JMA website

and in documentation (`https://www.data.jma.go.jp/mscweb/en/himawari89/space_segment/spsg_ahi.html`).

For the purpose of this work, AHI infrared data were analysed at 10 min intervals to determine the column amounts of SO_2 gas and ash particle mass loadings, both in units of $\mathrm{g\,m^{-2}}$. At the sub-satellite point the nominal spatial resolution of infrared pixels is 4 $\mathrm{km^2}$, increasing to > 100 $\mathrm{km^2}$ at the largest scan angles. The Raikoke plume covered a relatively large geographic region and range of latitudes/longitudes, so the data were first rectified and resampled to a grid of 1336×2139 latitude $\times$ longitudes centred at 52.5° N latitude and 175° E longitude using a stereographic projection. These infrared data were then processed to determine SO_2 and ash amounts at 10 min intervals. The final data were analyzed at both 10 min and hourly intervals. The basis of the retrieval of SO_2 slant column amount relies on using AHI band 10 centred near to 7.3 μm. At this wavelength there is a strong SO_2 absorption band. Water vapor and clouds cause interference with the SO_2 signal and introduce a positive bias. Therefore, a retrieval scheme was devised to minimize the interfering effects. In short, the bias is minimized by subtracting an offset SO_2 retrieval for a small region where no SO_2 is believed to exist. Details of the retrieval method are very similar to a scheme devised for the High Resolution Infrared Sounder (HIRS) data described by Prata et al. (2004).

Volcanic ash effective particle radius and optical depth are retrieved using AHI bands 14 ($\sim$ 11.2 μm) and 15 ($\sim$ 12.4 μm) on the same latitude/longitude grid as that used for SO_2. The basic physics has been described by Prata (1989) and the retrieval methodology has been described by Prata and Prata (2012) using Meteosat Second Generation (MSG) Spin-Enhanced Visible and Infrared Imager (SEVIRI) data, which has very similar characteristics to the AHI data used here.

Discussions of potential error sources in ash retrieval can be found in numerous papers in the literature, e.g., Wen and Rose (1994); Prata et al. (2001); Clarisse et al. (2010); Mackie and Watson (2014); Western et al. (2015). Prata and Prata (2012) and Clarisse and Prata (2016) provide some error estimates based on independent validation which suggest single pixel retrievals have an absolute error of ± 0.5 $\mathrm{g\,m^{-2}}$ with a low bias; however, much larger errors and biases can occur on occasion and it is generally accepted that relative errors typically lie between 40–60 %. Single pixel retrievals < 0.2 $\mathrm{g\,m^{-2}}$ are regarded as at the threshold of detection. The presence of ice reduces the ash mass estimates by an amount that depends on the proportion of the pixel covered by ice. However, during the Raikoke eruption, ice was not observed except possibly at the start of the eruption which could cause lower ash mass estimates.

The retrieval assumes that pixels detected as containing ash are completely ash covered and although meteorological cloud tests are used, inevitably some anomalous retrievals occur. To minimise these, a mask was used whereby all pixels falling outside a 0.1 $\mathrm{g\,m^{-2}}$ contour line are removed. Within the 0.1 $\mathrm{g\,m^{-2}}$ contour, a 9×9 median filter was applied to remove any remaining "spikes". These measures are largely cosmetic and are based on the premise that anomalous pixels appear to be unphysical in nature.

Integrating the horizontal mass loadings for volcanic ash and SO_2 their emitted masses can be estimated. Based on the AHI measurements the total emitted very fine ash mass ($d < 32$ μm) ranges between

0.4–1.8 $\times 10^9$ kg, the SO_2 mass between 1–2 $\times 10^9$ kg. The latter agrees well with the TROPOMI measurement in Sect. 4.1."

4.4. Vertical Aerosol Distribution by CALIOP

The CALIOP data was provided by Christian von Savigny who contributed to Muser et al. (2020): "CALIOP (Cloud-Aerosol Lidar with Orthogonal Polarization) is one of three instruments on board the CALIPSO (Cloud-Aerosol Lidar and Infrared Pathfinder Satellite Observation) satellite, which was launched on 28 April 2006 and is still operational. CALIOP provides backscatter measurements at 532 nm and 1064 nm and the backscattered radiation at 532 nm is measured in two channels detecting orthogonally polarized radiation. The determination of the Raikoke plume height is based on total attenuated backscatter data at a wavelength of 532 nm. CALIOP L1 data version 4.10 is used." Further details on CALIOP data can be found in Vaughan et al. (2004).
On 23 June 2019, at around 15:00 UTC the CALIOP instrument captured part of the volcanic cloud of the Raikoke eruption. The cloud is visible between 15 and 16 km as a distinct signal in the total attenuated backscatter at 532 nm.

5. Methods and Tools

This section describes methods and tools that I used in the scope of this thesis. In Sect. 5.1 details on forward operators are given. These forward operators derive quantities from model results that can directly be compared with observations. The basic concept of data assimilation is introduced in Sect. 5.2. Data assimilation is a mathematical approach to bring a model state closer to observations. Furthermore, in the scope of this thesis an ensemble variational method (ART En-Var) was developed for which the algorithm is explained here. In order to objectively quantify differences between model results and observations, I apply two verification metrics. Details on these metrics are given in Sect. 5.3.

5.1. Forward Operators

Forward operators, also known as observation operators, come into play when model results and observations are compared with each other. In most cases, measuring instruments, especially remote sensing devices, do not measure quantities that can be compared directly to model variables. For example, satellites measure the radiance of aerosol clouds in two dimensions, whereas the model returns aerosol concentrations in all three spatial dimensions. Forward operators are used to translate the model aerosol concentration into the same quantity that is retrieved from the (satellite) measurement. In the scope of this work, I compare column integrated mass and the total attenuated backscatter at 532 nm which are described in the following.

5.1.1. Column Integrated Mass

The column integrated mass of an aerosol or a trace gas is a commonly retrieved quantity from satellite measurements. Deriving this quantity from ICON-ART model output is rather simple, as cells in one model column have all the same base area. The column integrated mass Γ_l of a species l is

$$\Gamma_l = \sum_{i=1}^{n_{lev}} \left(\Psi_{3,l} \rho_a \Delta z\right)_i \,. \tag{5.1}$$

It is the sum over all n_{lev} model levels within one vertical column of the mass loading in each grid cell. For ICON-ART model output, the mass loading in one grid cell is the product of the mass mixing ratio $\Psi_{3,l}$, the air density ρ_a, and the height of the model level Δz.

5.1.2. Total Attenuated Backscatter

The total attenuated backscatter at one wavelength λ is typically retrieved from lidar measurements. In this thesis I compare model results to measurements at $\lambda = 532$ nm. These Lidar instruments are usually either ground or satellite based. The Lidar sends out a laser beam. Once the light interacts with an aerosol particle, the light is partially scattered back to the instrument where the backscattered radiation is measured. However, parts of the backscattered light is removed from its path of travel due to extinction on its way from the instrument to the particle and back. This is why the backscatter signal is attenuated. The total attenuated backscatter ε at a distance r_d from the measuring instrument is determined by

$$\varepsilon(r_d) = \beta_b(r_d) \exp\left(-2 \int_0^{r_d} \beta_e(r'_d) dr'_d\right). \tag{5.2}$$

It depends on the volume backscattering coefficient β_b and the volume extinction coefficient β_e. In ICON-ART, both are determined by summing over all aerosol modes l

$$\beta_e = \sum_l k_{e,l} \rho_a \Psi_{3,l} \tag{5.3}$$

$$\beta_b = \sum_l k_{b,l} \rho_a \Psi_{3,l}\,. \tag{5.4}$$

Values for k_e and k_b at $\lambda = 532$ nm for the different volcanic aerosol modes are listed in Appendix A. Assuming a nadir looking satellite instrument, e.g., CALIOP, the resulting forward operator in ICON-ART simplifies to

$$\varepsilon(z) = \beta_b(z) \exp\left(-2 \sum_{i=1}^{z} \beta_e(z_i) \Delta z_i\right). \tag{5.5}$$

The total attenuated backscatter is then given at every model level z.

5.2. Basics of Data Assimilation

Numerical weather prediction is an initial value problem and so is aerosol dispersion forecasting. That means, even a hypothetically perfect model could only deliver a perfect forecast if the exact initial state is known. The initial state contains all relevant variables, e.g., temperature, pressure, wind speed and direction, aerosol concentrations, and so forth, at every point in space at time t_0. The (atmospheric) state in a model is represented by the state vector $\mathbf{x}$. It contains all relevant variables at every grid point. The true state $\mathbf{x_t}$ is generally not known at every grid point, hence, it can only be estimated. Data assimilation provides the best estimate of the initial state at t_0 of the atmospheric state and the atmospheric composition. For this purpose, in data assimilation all available information from observations and previous model forecasts are combined to derive the so-called analysis state $\mathbf{x_a}$.

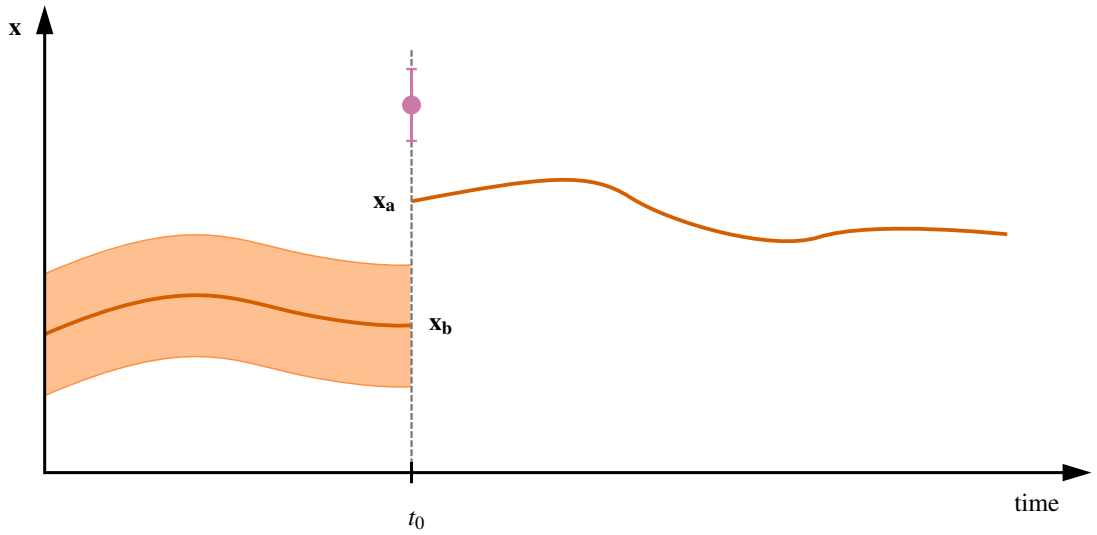

Figure 5.1: Basic concept of data assimilation at one time step t_0. The model state is depicted in red with the background state $\mathbf{x_b}$ and the analysis state $\mathbf{x_a}$ at t_0. An observation is indicated by the purple circle. The observation error and the model error are depicted by the error bar and the shading, respectively.

The basic principle of this idea is sketched in Fig. 5.1. The model state of a previous forecast, gives us a first guess, also known as background state, $\mathbf{x_b}$. Observations at t_0 (purple dot) deviate from $\mathbf{x_b}$. Data assimilation provides $\mathbf{x_a}$, the analysis state, that combines $\mathbf{x_b}$ and observations. In doing so, the model errors and also observational errors are taken into account. The red shading illustrates the model errors which are typically represented by the covariance matrix $\mathbf{B}$. The observational errors are given by the error matrix $\mathbf{R}$ and are illustrated by the error bar in Fig. 5.1. A new forecast run is then initialized with $\mathbf{x_a}$.

Observations are given by the observation vector $\mathbf{y}$. In practice, there are usually not as many observations as there are degrees of freedom in the state vector $\mathbf{x_a}$. In order to directly compare the observation vector with the state vector, we need a function that transforms the model state into observation space. This is done by the forward operator H which is also known as observation operator. In general, the forward operator can be nonlinear. In that case $\mathbf{H}$ is its linear approximation. For any $\mathbf{x}$ in the vicinity of $\mathbf{x_b}$ the linearized forward operator reads

$$H(\mathbf{x}) - H(\mathbf{x_b}) \approx \mathbf{H}(\mathbf{x} - \mathbf{x_b})\,. \tag{5.6}$$

Knowing H, we could find a state vector that fits the observation vector $\mathbf{y} = H(\mathbf{x})$. The aim of data assimilation is to find $\mathbf{x_a}$ in a way that it fits $\mathbf{x_b}$ and $\mathbf{y}$ best by taking $\mathbf{B}$ and $\mathbf{R}$ into account. Variational data assimilation methods are one strategy to solve this problem.

5.2.1. Variational Data Assimilation (2D-Var)

Variational data assimilation methods are commonly represented by the well-known 3D-Var or 4D-Var methods. Their names indicate the dimensions which are considered during assimilation. The 3D-Var method assimilates observations that contain information in all three spatial directions. In addition to that, 4D-Var also takes into account the temporal component. In this thesis, a 2D approach is pursued, as the horizontal distribution of volcanic ash is assimilated. Textbooks, e.g., Nakamura and Potthast (2015), provide detailed descriptions on the derivations of the following equations. Here, the basic concept is replicated.
The idea of variational data assimilation methods is to iteratively find $\mathbf{x_a}$ that minimizes the cost function

$$J(\mathbf{x}) = (\mathbf{x}-\mathbf{x_b})^{\mathrm{T}}\mathbf{B}^{-1}(\mathbf{x}-\mathbf{x_b}) + (\mathbf{y}-H(\mathbf{x}))^{\mathrm{T}}\mathbf{R}^{-1}(\mathbf{y}-H(\mathbf{x}))\,. \tag{5.7}$$

Consequently, the gradient of J becomes 0 at $\mathbf{x_a}$. With Eq. 5.6, a positive definite matrix $\mathbf{R}$, and $\mathbf{HBH}^{\mathrm{T}}$ being positive, the minimization of $J(\mathbf{x})$ reads

$$\nabla J(\mathbf{x_a}) = 0 = 2\mathbf{B}^{-1}(\mathbf{x_a}-\mathbf{x_b}) - 2\mathbf{H}^{\mathrm{T}}\mathbf{R}^{-1}(\mathbf{y}-H(\mathbf{x_a})) \tag{5.8}$$

$$0 = \mathbf{B}^{-1}(\mathbf{x_a}-\mathbf{x_b}) - \mathbf{H}^{\mathrm{T}}\mathbf{R}^{-1}(\mathbf{y}-H(\mathbf{x_b})) - \mathbf{H}^{\mathrm{T}}\mathbf{R}^{-1}\mathbf{H}(\mathbf{x_a}-\mathbf{x_b})\,. \tag{5.9}$$

Rearranging the terms leads to

$$\mathbf{x_a} = \mathbf{x_b} + \mathbf{BH}^{\mathrm{T}}\left(\mathbf{R}+\mathbf{HBH}^{\mathrm{T}}\right)^{-1}(\mathbf{y}-\mathbf{Hx_b}) \tag{5.10}$$

in which the expression

$$\mathbf{K} = \mathbf{BH}^{\mathrm{T}}\left(\mathbf{R}+\mathbf{HBH}^{\mathrm{T}}\right)^{-1} \tag{5.11}$$

is called gain. The gain $\mathbf{K}$ can be interpreted as the factor with which the difference between observations and background state is weighted to get the increment $\mathbf{x_a}-\mathbf{x_b}$.
In this approach, the analysis equation (Eq. 5.10) is solved in observational space. This form is known as Physical Space Assimilation System (PSAS). Please note that Eq. 5.10 is not constricted to 2D-Var. It is also valid for 3D-Var data assimilation.

5.2.2. En-Var Method

One of the main challenges in data assimilation is to quantify the model error, hence, to find a formulation for $\mathbf{B}$. A basic approach is the use of a Gaussian error covariance matrix $\mathbf{C}$. It can be interpreted as a localization matrix. The formulation of $\mathbf{C}$ is described in more detail in Sect. 5.2.3. Another approach to estimate model uncertainties is the use of ensemble simulations (Nakamura and Potthast, 2015). This

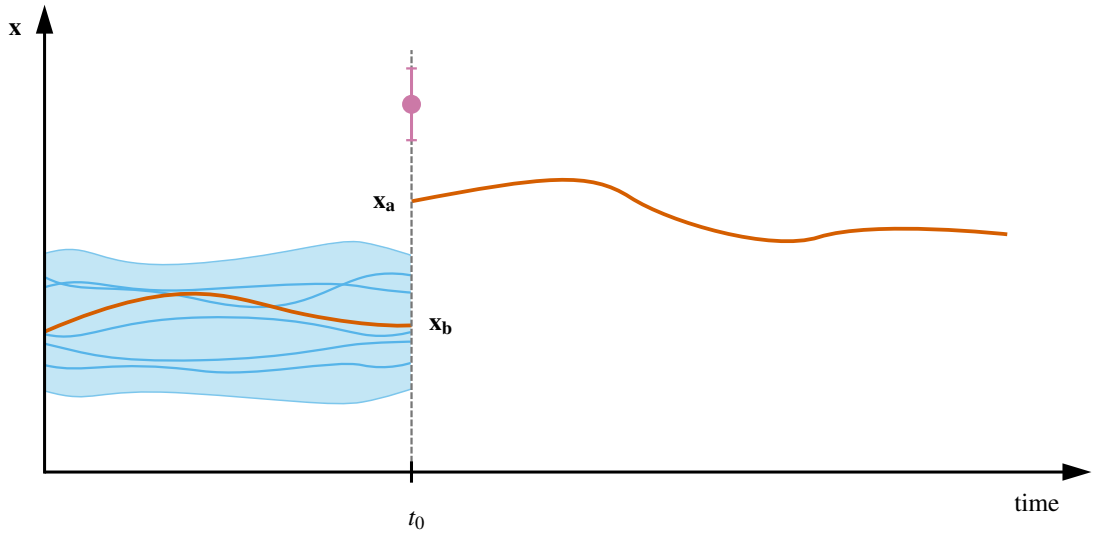

Figure 5.2: The basic concept of the En-Var method: the deterministic run is depicted in red with the background state $\mathbf{x_b}$ and the analysis state $\mathbf{x_a}$ at t_0. The additional ensemble members are given in blue and the uncertainty given by the ensemble is illustrated by the blue shading. An observation is indicated by the purple circle with the error bar representing the observation error.

idea is depicted in Fig. 5.2. Together with the background state $\mathbf{x_b}$ a set of E ensemble members is shown. Additional members are depicted in blue color. This ensemble allows the quantification of the model uncertainty (blue shading) with respect to disturbances that are introduced upon ensemble generation.

The ensemble matrix $\mathbf{X}$ is composed of the departure of the state vectors of member $\mathbf{x}^1$ to $\mathbf{x}^E$ from the ensemble mean $\overline{\mathbf{x}}$

$$\mathbf{X} = \frac{1}{\sqrt{E-1}}(\mathbf{x}^1 - \overline{\mathbf{x}}, ..., \mathbf{x}^E - \overline{\mathbf{x}}) \,. \tag{5.12}$$

In the scope of this thesis, I use a combination of both approaches. Hence, the model error covariance $\mathbf{B}$ consists of the Gaussian localization matrix $\mathbf{C}$ and the information provided by the ensemble. Mathematically, the model error covariance matrix is formulated with the element-wise product (Schur product)

$$\mathbf{B} = \mathbf{C} \circ \mathbf{X}\mathbf{X}^{\mathrm{T}} \,. \tag{5.13}$$

Consequently, the analysis equation (Eq. 5.10) can be written as

$$\mathbf{x_a} = \mathbf{x_b} + \left(\mathbf{C} \circ \mathbf{X}\mathbf{X}^{\mathrm{T}}\right) \mathbf{H}^{\mathrm{T}} \left(\mathbf{R} + \mathbf{H}\left(\mathbf{C} \circ \mathbf{X}\mathbf{X}^{\mathrm{T}}\right) \mathbf{H}^{\mathrm{T}}\right)^{-1} (\mathbf{y} - \mathbf{H}\mathbf{x_b}) \tag{5.14}$$

in which the gain for the En-Var data assimilation scheme is given by

$$\mathbf{K} = \left(\mathbf{C} \circ \mathbf{X}\mathbf{X}^{\mathrm{T}}\right) \mathbf{H}^{\mathrm{T}} \left(\mathbf{R} + \mathbf{H}\left(\mathbf{C} \circ \mathbf{X}\mathbf{X}^{\mathrm{T}}\right) \mathbf{H}^{\mathrm{T}}\right)^{-1} . \tag{5.15}$$

5.2.3. ART En-Var Algorithm

In the scope of this thesis, I implemented an algorithm for the 2D En-Var assimilation of column integrated volcanic ash mass into *datools*. *Datools* is a coding environment developed and used at DWD for the development of new data assimilation tools. It contains data assimilation algorithms amongst other useful tools. In this section (Sect. 5.2.3), I briefly explain the 2D ART En-Var algorithm.
As mentioned above, Eq. 5.10 and Eq. 5.14 can be used for 3D-Var and 3D En-Var, respectively. However, in the scope of this work, a 2D approach is pursued. This reduces the complexity and allows several simplifications which I shortly discuss here. The filtered Himawari data, as described in Sect. 4.3, is used as observational data. The dataset contains 2D column integrated total ash mass concentrations. However, it does not include any information on the height levels in which the ash cloud is located. For simplification, I assume that the vertical distribution of volcanic ash is correct in the model background state. Ash is only assimilated in the horizontal plane. This additionally allows the reduction of the state vector $\mathbf{x}$ to a 2D field. This reduction has also technical advantages. First of all, it significantly reduces the size of the state vector $\mathbf{x}$ by the number of vertical levels (in this thesis 90 levels) which speeds up computation. Secondly, it reduces the necessary memory. Since the ART En-Var code is not yet parallelized, it has to run on a single node. Hence, memory is a limiting factor. The 2D approach has another advantage for the formulation of the forward operator $\mathbf{H}$. After interpolating the observations on the model grid, $\mathbf{y}$ and $\mathbf{x}$ have the same length and contain the same variable. This simplifies Eq. 5.14, as $\mathbf{H} = \mathbf{I}$ becomes the identity matrix.
So far, little has been said about the composition of $\mathbf{R}$ and $\mathbf{C}$. In operational data assimilation it is often assumed that observational errors are uncorrelated (e.g., Stewart et al., 2013; Liu et al., 2019). This results in a diagonal matrix $\mathbf{R}$. In the scope of this work, I follow the same approach. Hence, the observation error matrix is composed of $\mathbf{R} = r\mathbf{I}$ with r being the observation error.
The model error matrix $\mathbf{B}$ can become rather large, i.e., in the order of $10^6 \times 10^6$ for a 3D-var data assimilation scheme for a global simulation. This makes its handling problematic in terms of storage (Navon et al., 2005). As described above, $\mathbf{B}$ consist of a combination of the localization matrix $\mathbf{C}$ and the ensemble matrix $\mathbf{X}$. In the scope of this thesis, $\mathbf{C}$ is set up as a 2D Gaussian matrix

$$C_{ij} = e^{-\frac{1}{2}\frac{||p_i - p_j||^2}{\sigma_C^2}}. \tag{5.16}$$

C_{ij} is the covariance stored in $\mathbf{C}$ at index i and j. The covariance depends on the distance between the two points p_i and p_j. They represent the location of the variables at index i and j, respectively. The correlation length scale is given by σ_C. This formulation (Eq. 5.16) has the advantage that the full $\mathbf{C}$ matrix has not to be stored during runtime. However, the matrix can easily be evaluated at every index ij.
As $\mathbf{C}$ is usually a very large matrix, an additional approach is used to further speed up computation. Instead of applying $\mathbf{C}$ directly, $\mathbf{C}^{1/2}\mathbf{C}^{1/2}$ is computed. This multiplication in two steps allows a transfor-

mation onto an auxiliary grid and back to the original grid. This can reduce the number of computations if a suitable auxiliary grid is chosen. Thanks to the characteristics of a Gaussian matrix, the square root can be determined, which is a Gaussian matrix again.
The multiplication of $\mathbf{C} \circ \mathbf{X}\mathbf{X}^{\mathrm{T}}$ with a vector $\mathbf{z}$ is computed at every index i of the resulting vector with

$$\sum_j \left(\mathbf{C} \circ \mathbf{X}\mathbf{X}^{\mathrm{T}}\right)_{ij} z_j = \sum_j \sum_e C_{ij} X_{ie} X_{je} z_j \tag{5.17}$$

$$= \sum_j \sum_e X_{ie} C_{ij} X_{je} z_j \tag{5.18}$$

$$= \sum_e \sum_\zeta X_{ie} C_{i\zeta}^{1/2} \left(\sum_j C_{\zeta j}^{1/2} X_{je} z_j \right). \tag{5.19}$$

The indices i and j are in model space on the original grid. The index ζ loops over the auxiliary grid and e sums over the E ensemble members. In this work I use an unstructured triangular ICON grid (R02B05) with 80 km horizontal resolution as an auxiliary grid. As the data assimilation is only applied in an area around the Raikoke volcano and not on the global grid, it has to be ensured that the auxiliary grid covers all of the original grid. In the scope of this work, I do assimilate in a region between 40 – 67° N and 133° E – 134° W. The auxiliary grid contains grid points between 39 – 68° N and 132° E – 133° W.
Having a formulation for $\mathbf{H}$, $\mathbf{R}$, $\mathbf{X}$, and $\mathbf{C}$, the analysis state $\mathbf{x_a}$ can simply be calculated by applying Eq. 5.14. However, a direct solution would need the computation of the inverse of $\mathbf{R} + \mathbf{H}\left(\mathbf{C} \circ \mathbf{X}\mathbf{X}^{\mathrm{T}}\right)\mathbf{H}^{\mathrm{T}}$. Computing the inverse of a large matrix is usually computationally expensive if possible at all. Instead, an iterative approach can be pursued. The multiplication of

$$\mathbf{z} = \left(\mathbf{R} + \mathbf{H}\left(\mathbf{C} \circ \mathbf{X}\mathbf{X}^{\mathrm{T}}\right)\mathbf{H}^{\mathrm{T}}\right)^{-1} \left(\mathbf{y} - \mathbf{H}\mathbf{x_b}\right) \tag{5.20}$$

can be solved as a linear equation system in the form of

$$\left(\mathbf{R} + \mathbf{H}\left(\mathbf{C} \circ \mathbf{X}\mathbf{X}^{\mathrm{T}}\right)\mathbf{H}^{\mathrm{T}}\right)\mathbf{z} = \mathbf{y} - \mathbf{H}\mathbf{x_b} \tag{5.21}$$

$$\mathbf{A}\,\mathbf{z} = \mathbf{b} \tag{5.22}$$

To solve this large equation system, I use the method of conjugate gradients (CG method) (Hestenes and Stiefel, 1952). The analysis state is then derived by the post-multiplication of

$$\mathbf{x_a} = \mathbf{x_b} + \left(\mathbf{C} \circ \mathbf{X}\mathbf{X}^{\mathrm{T}}\right)\mathbf{H}^{\mathrm{T}}\mathbf{z}. \tag{5.23}$$

The CG method is extensively described in literature (e.g., Hestenes and Stiefel, 1952; Barrett et al., 1994). Code examples can be found online, e.g., Conjugate gradient method (2021). Theoretically, the CG method reaches the exact solution after a maximum of m iterations, when the size of $\mathbf{A}$ is $m \times m$.

However, the iteration is usually stopped as soon as the residuum is small enough. The convergence of th CG method can be increased with a suitable preconditioner. In this thesis, I use

$$\mathbf{M} = \frac{1}{r + \left(\frac{1}{2}\sqrt{\frac{4\pi}{n_{cell}}}\frac{180}{\pi}\right)^2}\mathbf{I} \tag{5.24}$$

as the preconditioner matrix in which r is the observation error and n_{cell} the number of grid cells of the global ICON grid of the first guess.

5.3. Verification Metrics

I apply two different verification metrics in the scope of this thesis to objectively quantify differences between observation and model fields. Details on the Fractions Skill Score (Roberts and Lean, 2008; Roberts, 2008) are given in Sect. 5.3.1. Additionally, I use the object based verification metric, the Structure-Amplitude-Location (SAL) method, introduced by Wernli et al. (2008), which is described in Sect. 5.3.2.

5.3.1. Fractions Skill Score

The Fractions Skill Score (FSS) is a spatial verification measure (Roberts and Lean, 2008; Roberts, 2008). It assesses the quality of a forecast of a two dimensional quantity by comparing it to observational data. The score is used in many studies as a verification metric (e.g., Baldauf et al., 2011; Simonin et al., 2017; Caldas-Alvarez et al., 2021). The FSS aims to avoid the double penalty that is inherent to point based verification measures. This double penalty occurs when the model field is slightly shifted compared to observation. In this case, a point to point comparison, e.g., by root mean square error, can result in a large error, although both fields subjectively seem to match well. The FSS is not evaluated at single points only, but within a $n_{box} \times n_{box}$ box of neighboring cells. With a variation in the number of neighboring cells that are accounted for the FSS, the metric provides information on the spatial scale at which the forecast becomes useful.

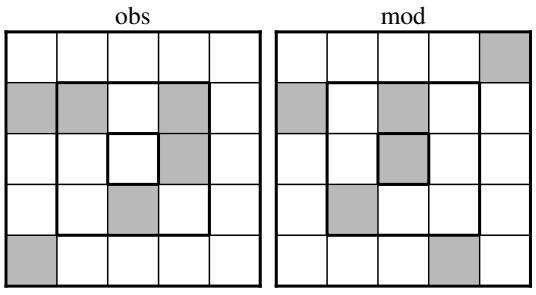

Figure 5.3: Schematic of the basic concept of the FSS, with observational field (obs) on the left and model field (mod) on the right. Adapted from Roberts (2008).

To compute the FSS, observation and model data must be on the same grid. The computation itself is a two stage process. First, the fractions are determined based on a threshold value. In the second step, the actual skill score is computed. In the scope of this work, I compare fields of column integrated volcanic ash mass with each other.

The generation of the fractions for observation and model result can be explained with the schematic in Fig. 5.3. It depicts two binary fields in which cells with a column integrated mass exceeding a defined threshold R^* are shown in gray. Cells which contain a column integrated mass below threshold are depicted in white. The binary observation field (obs) is shown on the left and the binary model field (mod) on the right. In Fig. 5.3, the fraction value can be determined, on different spatial scales for the innermost cell, exemplarily. Without considering any neighboring cells, the fraction value of the innermost cell is $f_{obs,i} = 0/1$ and $f_{mod,i} = 1/1$ in the observation field and the model field, respectively. By considering also the neighboring cells in the highlighted 3×3 box, the fraction value of the inner most cell is $f_{obs,i} = 4/9$ in the observation and $f_{mod,i} = 3/9$ in the model field. Considering the full domain, the fraction value of the innermost cell results to $f_{obs,i} = f_{mod,i} = 6/25$. This example shows how observation and model disagree when evaluated with a point based approach, but agree when the whole 5×5 box is considered.

Once fraction values $f_{obs,i}$ and $f_{mod,i}$ of all n_{cell} cells in domain $\mathscr{D}$ are known, the FSS can be computed. Like most skill scores, the FSS relates a metric to a reference value. Here, the Fractions Brier Score (FBS) is used and related to a worst case value of FBS. Hence, the

$$\mathrm{FSS} = 1 - \frac{\mathrm{FBS}}{\mathrm{FBS}_{\mathrm{worst}}} \tag{5.25}$$

ranges between 0 and 1, with 1 indicating a perfect forecast.

The FBS is given by

$$\mathrm{FBS} = \frac{1}{n_{cell}} \sum_{i \in \mathscr{D}} \left(f_{obs,i} - f_{mod,i}\right)^2 \tag{5.26}$$

and $\mathrm{FBS}_{\mathrm{worst}}$ by

$$\mathrm{FBS}_{\mathrm{worst}} = \frac{1}{n_{cell}} \left[\sum_{i \in \mathscr{D}} f_{obs,i}^2 + \sum_{i \in \mathscr{D}} f_{mod,i}^2 \right], \tag{5.27}$$

respectively.

A detailed discussion on the properties of the FSS can be found in literature (e.g., Roberts and Lean, 2008; Roberts, 2008; Skok and Roberts, 2016).

5.3.2. SAL – Method

The SAL – method was developed by Wernli et al. (2008) and extensively tested by Wernli et al. (2009). It aims to objectively compare the agreement of two two-dimensional fields of an arbitrary quantity R,

e.g., model result with satellite observation. The method quantifies differences based on three metrics which are **S**tructure, **A**mplitude, and **L**ocation. Originally, this method was developed and tested for the comparison of observed and modeled precipitation fields. In the scope of this work, I use it to analyze volcanic aerosol dispersion forecasts. The results have been published by Muser et al. (2020) and are further discussed in Sect. 6. In this connection, I apply the SAL – method for the comparison of column integrated ash mass which is retrieved based on AHI measurements and ICON-ART results. In the following, I describe the basic principle of this method and give some examples.

The method compares an arbitrary quantity R, in this work a column integrated mass, which is given on a domain $\mathscr{D}$ with n_{cell} grid points both for model results R_{mod} and observations R_{obs}. The domain must be the same for model and observation $\mathscr{D}_{mod} = \mathscr{D}_{obs}$. This means, model and observational data must be on the same grid. In order to compute the location and structure component later, defined objects of R must be delimited. Therefore, a threshold value

$$R^* = f_{SAL} R^{\max} \tag{5.28}$$

is used. R^* is the threshold value which correlates with the maximum of R in $\mathscr{D}$ by a factor f_{SAL}. As stated by Wernli et al. (2008) "the choice of factor" f_{SAL} in Eq. 5.28 "is not based on objective criteria". For their comparison of precipitation fields, Wernli et al. (2008) use $f_{SAL} = 1/15$ which "was motivated by the fact that for most considered cases (...), this contour separates features of the precipitation field that correspond reasonably well to distinct objects that can be identified by eye" (Wernli et al., 2008). In the scope of this work, I chose a comparable approach. Details on the choice of the threshold value R^* are given in Sect. 6 together with the results of the SAL – method.

The three different components S, A, and L are explained in order of increasing complexity. To compute the amplitude value A, the domain averaged value of R

$$\overline{R} = \frac{1}{n_{cell}} \sum_{(i,j)\in\mathscr{D}} R_{ij} \tag{5.29}$$

is determined. Here, R is evaluated at every grid cell (i, j) of domain $\mathscr{D}$. Based on this domain averaged quantity $\overline{R}$, the amplitude component

$$A = \frac{\overline{R}_{mod} - \overline{R}_{obs}}{0.5\left[\overline{R}_{mod} + \overline{R}_{obs}\right]} \tag{5.30}$$

is defined. A is the normalized difference of domain averaged $\overline{R}$ between model result and observation. The resulting value for A always ranges between -2 and $+2$, with a perfect agreement for $A = 0$. For $A > 0$ the model overestimates R compared to the observation and underestimates the observation for $A < 0$, respectively.

The location value $L = L_1 + L_2$ is composed of two components. L_1 is determined by the distance between the center of mass in the modeled $\mathbf{z}(R_{mod})$ and the observed field $\mathbf{z}(R_{obs})$. The distance is normalized by the largest distance d_{max} between two grid cells in $\mathscr{D}$. Thus, the value of

$$L_1 = \frac{|\mathbf{z}(R_{mod}) - \mathbf{z}(R_{obs})|}{d_{max}} \tag{5.31}$$

always ranges between 0 and 1.

The second component, L_2, accounts for the different locations of individual objects in the column integrated mass field. Therefore, it relates the averaged distance between the center of mass of the total column integrated mass field and that of individual objects. Each of these objects is weighted by

$$R_n = \sum_{(i,j)\in\mathscr{R}_n} R_{ij} \tag{5.32}$$

which is the sum of R within object $\mathscr{R}_n$. With n_{obj} objects, the weighted averaged distance between $\mathbf{z}$ and individual objects with index n

$$q = \frac{\sum_{n=1}^{n_{obj}} R_n \, |\mathbf{z} - \mathbf{z}_n|}{\sum_{n=1}^{n_{obj}} R_n} \tag{5.33}$$

is determined. The second component

$$L_2 = 2 \left[\frac{|q(R_{mod}) - q(R_{obs})|}{d_{max}} \right] \tag{5.34}$$

is normalized in a way, that its value always ranges between 0 and 1. Consequently, L ranges between 0 and 2 with a perfect agreement for $L = 0$.

The structure component S can be interpreted as the comparison of the area that is covered by the column integrated mass objects in the model result and the observation. In order to make S distinct from A,

$$V_n = \sum_{(i,j)\in\mathscr{R}_n} R_{ij}/R_n^{\max} = R_n/R_n^{\max} \tag{5.35}$$

is scaled by $R_n^{\max}$. It is the maximum value of R in the individual object $\mathscr{R}_n$. With the weighted averaged volume of all objects

$$V(R) = \frac{\sum_{n=1}^{n_{obj}} R_n V_n}{\sum_{n=1}^{n_{obj}} R_n} \tag{5.36}$$

the structure component

$$S = \frac{V(R_{mod}) - V(R_{obs})}{0.5\,[V(R_{mod}) + V(R_{obs})]} \tag{5.37}$$

can be determined. S is normalized in the same way as A, hence, the value always ranges between -2 and $+2$. Again, perfect agreement is indicated by $S = 0$. For $S > 0$ the quantity R is spread over a wider area in the model compared to the observation. The opposite is true for $S < 0$.

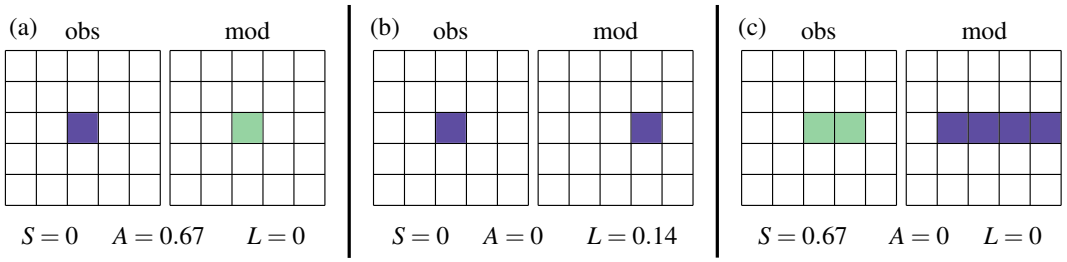

Figure 5.4: Arbitrary examples for three different comparisons between observations (left) and model results (right). Blue color represents a column integrated mass of 1, green color a column integrated mass of 2.

Three idealized examples are shown in Fig. 5.4 in order to visualize the differences between the three SAL components. In each of the three panels (a) to (c), the left and right grid show observation and model result, respectively. The blue color indicates a value of $R = 1$ and the green color of $R = 2$. For this example, a grid with $\Delta x = 1$ km is chosen. Figure 5.4 (a) shows a case with a non-zero measurement at only one grid cell. In the same grid cell, the model has a column integrated mass that is twice as high, hence, $A = 0.67$. As location and structure are both the same in observation and model, $S = 0$ and $L = 0$. The second case, Fig. 5.4 (b), agrees perfectly in structure and amplitude, thus, $S = 0$ and $A = 0$. The column integrated mass in the model result is only shifted by 1 km to the right compared to the observation. Therefore, the location value is $L = 0.14$. The third case, Fig. 5.4 (c), shows an example with one object with the same center of mass and amplitude, hence, $A = 0$ and $L = 0$. However, this time the area that is covered by the object in the model is twice the one in the observation. That is why the structure value results to $S = 0.67$.

A discussion of possible caveats of the SAL – method can be found in Wernli et al. (2008).

6. Simulation of the Raikoke Eruption 2019

On 21 June 2019 at 18:00 UTC the Raikoke volcano started to erupt (Sennert, 2019). The eruption period lasted for around 13 h. It consisted of several individual, short outbursts and one longer, continuous eruption (Bruckert et al., 2021). The volcano is located at 48.29° N, 153.24° E on Raikoke island. It is one of the central Kuril islands in the Sea of Okhotsk, part of western Pacific. The eruption of June 2019 was one of the largest volcanic eruptions during the last 30 years.

For the present study, the Raikoke eruption 2019 is subject of a numerical experiment to investigate the influence of aerosol dynamic effects and aerosol–radiation interaction on volcanic plume dispersion. Large parts of this section are based on *Particle aging and aerosol–radiation interaction affect volcanic plume dispersion: evidence from the Raikoke 2019 eruption* published in *Atmospheric Chemistry and Physics* (Muser et al., 2020). The copied segments are highlighted by quotation marks. These copied segments were originally written by myself. In this chapter, I rearranged or slightly rephrased a few passages compared to Muser et al. (2020). Since the publication of Muser et al. (2020) several bugs were fixed in ICON-ART. That is why some figures look slightly different to the original publication of Muser et al. (2020). However, the conclusions did not change. Beyond that, I present and discuss additional results to provide further insights.

6.1. Raikoke Simulation Setup

In the scope of this thesis I performed seven global simulations of the Raikoke eruption with the ICON-ART model. The simulation setup of these seven simulations is described in this chapter. The setup for four of the seven simulations is already described in Muser et al. (2020) and only replicated here.

"The simulations run on a R3B07 grid that is also used by DWD for operational weather forecasts. The horizontal grid resolution is on average $\Delta\bar{x} = 13.2$ km. 90 vertical levels resolve the atmosphere up to 75 km. The time step Δt is 60 s. Each simulation is started on 21 June 2019 at 12:00 UTC based on initialized analysis data provided by DWD. The simulation covers the first four days after the onset of the eruption.

The simulated volcanic emission starts on 21 June 2019, at 18:00 UTC and lasts for 9 h." For the simulation, Muser et al. (2020) assume that ash and SO_2 of the last three rather short outbursts between 03:00 and 07:00 UTC (22 June 2019) (Bruckert et al., 2021) were also emitted during the first 9 h of the eruption. An emission top height, bottom height, and an emission rate characterize the volcanic emission in the model. Between bottom and top height a uniform emission profile is assumed. Operational

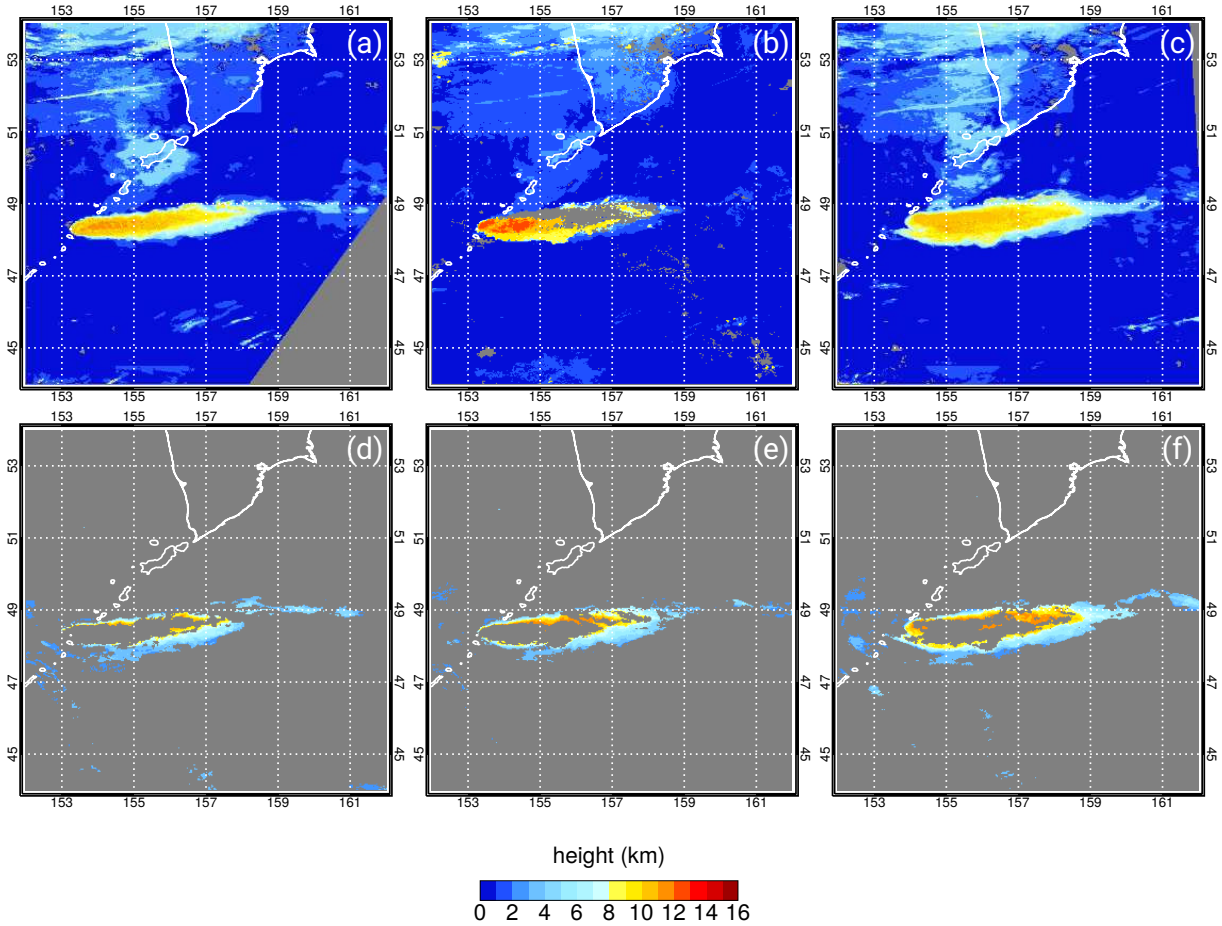

Figure 6.1: Plume height on 22 June 2019, at 01:25 UTC (a, d), 02:15 UTC (b, e), and 03:10 UTC (c, f). The top row shows standard cloud-top heights for (a) MODIS Terra, (b) VIIRS Suomi-NPP, and (c) MODIS Aqua. The bottom row plots ash heights from NOAA's dedicated volcanic ash algorithm for VIIRS on (d, f) NOAA-20 and (e) Suomi-NPP, considering only those pixels that potentially contain volcanic ash.

volcanic aerosol forecast at VAACs relies on such uniform profiles (Beckett et al., 2020). The emission rate was determined by combining information from satellite measurements and 1D plume simulations. Ash particles and SO_2 are emitted.

"The plume height estimate is based on the MODIS and VIIRS data shown in Fig. 6.1. The dedicated ash algorithm (lower panel) is much more restrictive than the standard cloud-top height algorithm (upper panel), but produces similar heights where it is applied. In general, both of these brightness temperature-based products indicate maximum plume heights in the 12–12.6 km range for the time period 7–9 h after the eruption. The estimated height uncertainty is $\sim$ 1.5 km. Based on this plume height estimate and also other studies (Sennert, 2019), the Raikoke eruption emits ash and SO_2 in the simulations at a constant eruption rate between 8 and 14 km above sea level.

The eruption rate of SO_2 is derived from measurements of the total emitted SO_2 mass. According to the TROPOMI (Sect. 4.1) and AHI data (Sect. 4.3), in the simulations 1.5×10^9 kg of SO_2 is emitted over the eruption period. To estimate the total mass eruption rate of volcanic ash, several 1D plume

Table 6.1: Emission parameters for ash emission with median diameter $d_{3,l}$, standard deviation σ_l of ash size distribution, and the mass emission rate Q_{emiss} of each ash mode and SO_2.

Ash mode	Accumulation	Coarse	Giant	SO_2
$d_{3,l}$ [µm]	0.8	2.98	11.35	–
σ_l [-]	1.4	1.4	1.4	–
Q_{emiss} [kg s^{-1} m^{-1}]	3.26	3.26	3.26	7.72

simulations using Plumeria (Mastin, 2007) and FPlume (Folch et al., 2016) were conducted offline, assuming the following parameter ranges: plume height 12–14 km, vent diameter 90–110 m, exit velocity 100–120 m s^{-1}, exit temperature 900–1100 °C, and exit gas mass fraction 3 %. For this purpose, profiles of atmospheric variables were obtained from ERA-Interim (Dee et al., 2011) and introduced in the 1D models ... The results are in the range of 1.45–9.95 $\times 10^6$ kg s^{-1}. Taking the mean value 5.7 $\times 10^6$ kg s^{-1} suggests that about 190 $\times 10^9$ kg tephra is emitted within 9 hours. Assuming that 1 % of the erupted mass is very fine ash with $d < 30$ µm (relevant for long-range transport) (Rose and Durant, 2009; Gouhier et al., 2019), Muser et al. (2020) estimate that 1.9 $\times 10^9$ kg very fine ash is injected into the atmosphere during the eruption. These estimates by the 1D models are in agreement with AHI data (Sect. 4.3).

The estimated 1.9 $\times 10^9$ kg of very fine ash are used in the ICON-ART simulations and distributed equally between accumulation, coarse, and giant modes. The number concentration of the log–normal distribution is calculated based on the median diameter $d_{3,l}$ and standard deviation σ_l of the emitted particle distribution. Table 6.1 lists details about these emitted particle size distributions. The values are based on data from Bonadonna and Scollo (2013).

To study the effect of aerosol dynamic processes and the radiative effect of internally mixed particles on the volcanic plume dispersion, a set of four different simulation scenarios" were conducted. To gain further insights into the relevant processes I conducted three additional simulations. Table 6.2 summarizes these scenarios. "The scenarios with AERODYN treat SO_2 as a chemical substance which

Table 6.2: Simulation scenarios with their represented processes.

scenario	aerosol dynamics and gas phase chemistry	aerosol–radiation interaction
AERODYN-rad	on	on
no_AERODYN-rad	off	on
AERODYN-no_rad	on	off
no_AERODYN-no_rad	off	off
no_coag	on (except coagulation)	on
no_cond	on (except condensation)	on
only_coag	only coagulation	on

can be oxidized. The chemical reaction scheme is the simplified OH-chemistry scheme implemented by Weimer et al. (2017). The no_AERODYN scenarios treat SO_2 as a passive tracer without any gas phase chemistry.

The first scenario (AERODYN-rad) uses the whole new development of the AERODYN module together with the radiative feedback of internally mixed particles. In the second scenario (no_AERODYN-rad) only insoluble ash particles of three different size ranges are transported. Secondary aerosol formation and particle aging are switched off. However, the volcanic ash still interacts with solar and thermal radiation. The third scenario (AERODYN-no_rad) considers the effects of aerosol aging without any radiative feedback of these particles. The fourth scenario represents the status quo of operational volcanic cloud forecast. It considers neither aerosol dynamic effects nor aerosol–radiation interaction."

Table 6.2 also lists the three additional simulations that exclude individual aerosol dynamic processes. The no_coag and the no_cond scenarios are similar to the AERODYN-rad scenario. The former excludes coagulation. The latter excludes the condensation of sulfuric acid on existing particles and the ISORROPIA module. The only_coag scenario corresponds to the no_AERODYN-rad scenario. No gasphase chemistry is computed. Coagulation is the only aerosol dynamic process included.

6.2. Ash– and SO_2–Transport

When evaluating volcanic ash and gas forecast, the horizontal distribution of ash and SO_2 is of great interest. This information is also crucial for the decision on airspace closure issued by VAACs. Here, I compare the simulated ash and SO_2 concentrations with observational data, introduced in Sect. 4.

The TROPOMI instrument provides information on the horizontal distribution of column integrated SO_2 mass. The satellite passed over the volcanic cloud after the Raikoke eruption. "Figure 6.2 shows three TROPOMI retrievals of SO_2 mass loading Γ_{SO_2} in $\mathrm{g\,m^{-2}}$ in panels (a), (b), and (c) for three different dates. Each of these three graphs is a composite of several satellite orbits, chosen from a batch of 14 consecutive orbits (approximately 24 h coverage). Those orbits that directly detect the volcanic cloud in Fig. 6.2 (a) intersected with the area of interest (see Sect. 4.1) on 22 June 2019, between 02:16 and 02:29 UTC. Data points containing the volcanic cloud signature in Fig. 6.2 (b) were measured on 23 June, between 00:15 and 02:10 UTC and in Fig. 6.2 (c) between 24 June, 20:16 UTC and 25 June, 03:13 UTC, respectively. Panels (d) to (f) show ICON-ART results of AERODYN-rad for three different time steps. These time steps have been chosen to be closest to the mean of the time period of the corresponding TROPOMI measurement."

During the first day after the eruption, the wind transports the SO_2 cloud mainly eastward. The maximum column integrated mass is still located close to the volcano (black triangle in Fig. 6.2). The SO_2 cloud turns northward at 180° E from where it starts to spread over the northern Pacific. Three days after the eruption, displayed in Fig. 6.2 (c), the SO_2 cloud covers large areas of the northern Pacific. It separated into two main branches. The larger one travels westward over Asia and the smaller one eastward over

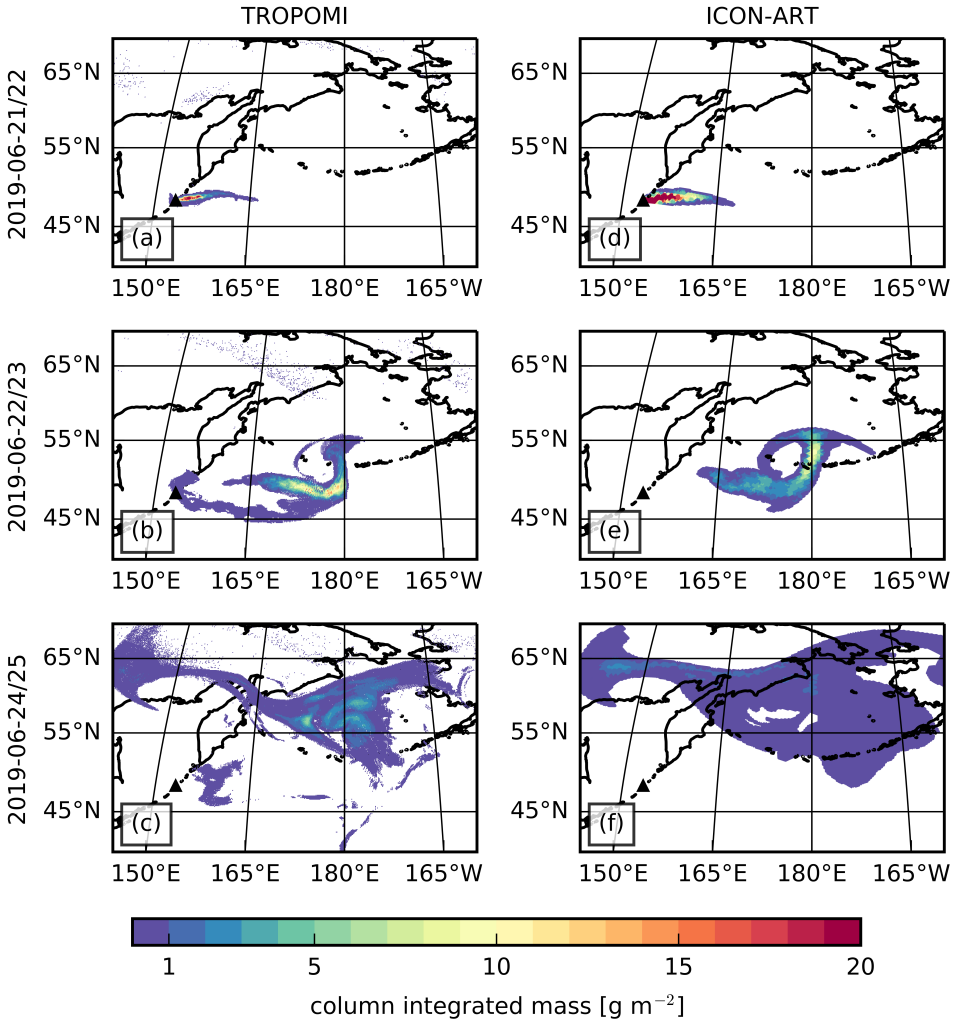

Figure 6.2: Mass loading of SO_2 measured by TROPOMI during three different time periods are shown in panels (a), (b), and (c). Panels (d), (e), and (f) show ICON-ART results of AERODYN-rad at corresponding time steps. The black triangle indicates the location of Raikoke.

North America. The maximum column integrated mass is now located in a cyclonic structure at around 55° N and 180° E.

"The overall structure of the SO_2 mass loading Γ_{SO_2} agrees well between model results and observations. This is especially true for the two earlier dates when the modeled atmospheric state can be assumed to be closer to reality than for later dates. But also the model result 3.5 days after its initialization in Fig. 6.2 (f) shows good agreement with the TROPOMI measurement in (c). A main difference between satellite retrieval and model result is the location of the maximum SO_2 mass loading. Although the magnitude of the maximum SO_2 mass loading is in good agreement, in the model results its location appears further downstream compared to the satellite measurement. One reason could be the different time of measurement and model result. However, a greater influence can be expected by uncertainties of the emission profile parametrization and of the simulated wind velocity. In case more SO_2 is emitted in

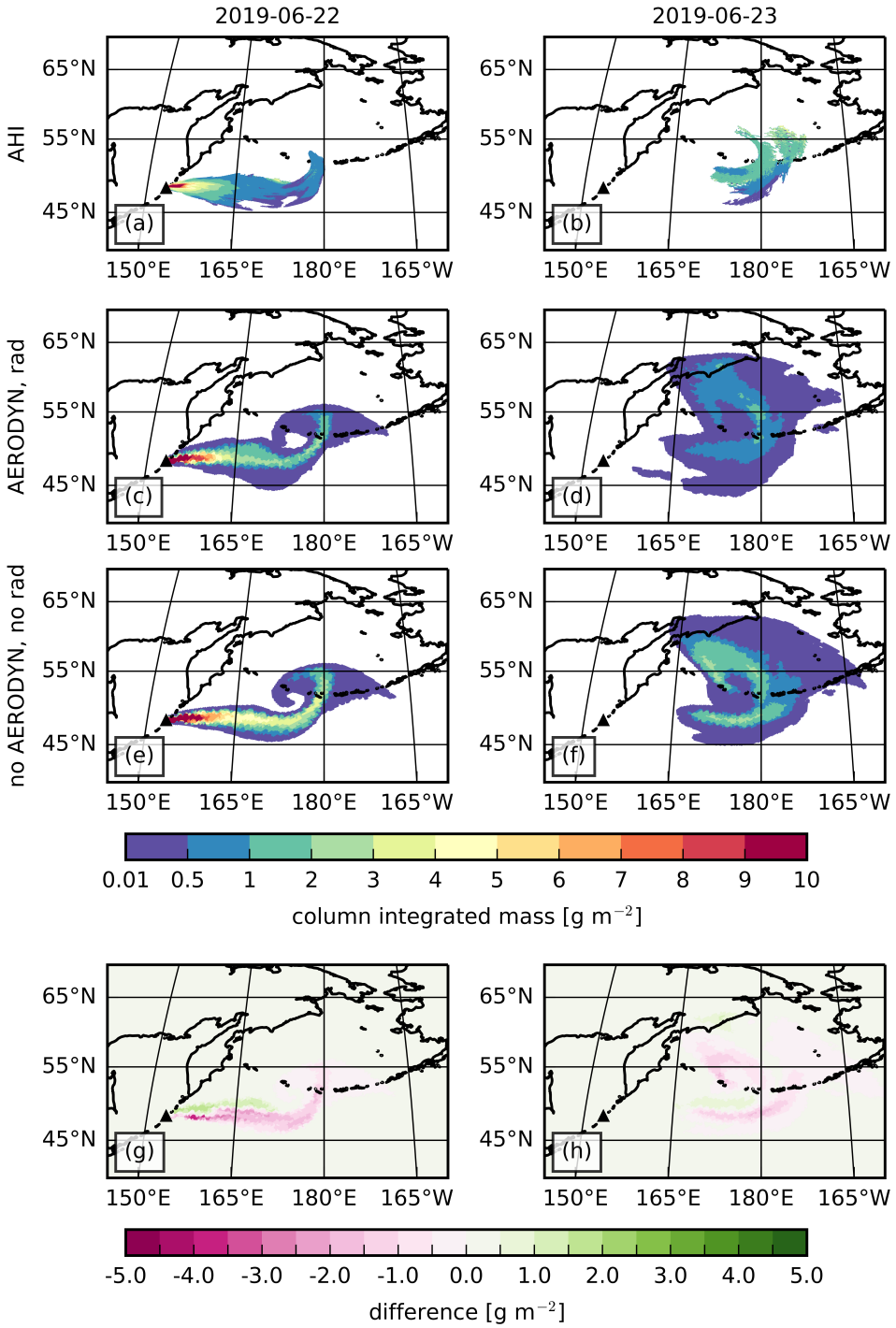

Figure 6.3: Daily mean column integrated mass of volcanic ash on 22 June (left column) and 23 June 2019 (right column). Panels (a, b) show results measured by AHI on board Himawari-8. Panels (c – f) show ICON-ART results for AERODYN-rad and no_AERODYN-no_rad, respectively. The black triangle depicts the location of Raikoke volcano. Panels (g) and (h) show the absolute difference between the two simulation scenarios.

altitudes with higher wind speed in the model, it will be transported faster. The same applies for the case that in some altitudes the wind speed in the model is slightly higher than it is in reality. Furthermore, the TROPOMI measurements can also be erroneous. The TROPOMI sensor might not capture all of the SO_2 due to deficiencies of the measurement technique in opaque regions." Additionally, the retrieval of column integrated SO_2 mass from the satellite measurement relies on the assumption of a pre-defined vertical SO_2 profile. The true vertical SO_2 profile is usually not known during the application of the retrieval algorithm. Hence, this assumption can also result in an incorrectly measured column integrated SO_2 mass.

The AHI instrument of the geostationary Himawari-8 satellite detected the volcanic ash cloud of the Raikoke 2019 eruption. "Figure 6.3 (a) and (b) show daily mean AHI retrievals of volcanic ash mass loading $\overline{\Gamma}_{ash}$. As described in Sect. 4.3, the filtered data is used. For the daily mean only ash containing pixels are considered. The same averaging approach is applied on the ICON-ART model results, shown in panels (c) to (f) of Fig. 6.3. Panels in the left column show measurements and model results of 22 June 2019, panels in the right column of 23 June." Simulation results of the AERODYN-rad scenario are displayed in panels (c) and (d). Panels (e) and (f) show results of the no_AERODYN-no_rad scenario. The difference between the new development (AERODYN-rad) and the VAAC approach (no_AERODYN-no_rad) is depicted in panels (g) and (h).

"On 22 June the volcanic ash cloud moved eastward to 180° E where the direction of transport turned northward. The maximum of daily mean mass loading $\overline{\Gamma}_{ash}$ is still located in proximity to the volcano. For this day, both model results and the satellite retrieval agree very well in location, structure, and absolute values of ash mass loading. It can be assumed that the model captures the atmospheric state well, one day after its initialization. Furthermore, there are only minor differences between the two different simulation setups for the results of 22 June in Fig. 6.3 (c) and (e). These differences are mainly restricted to the slightly higher mass loading in panel (e) and small differences in the volcanic cloud structure. For the first day after the eruption, the aerosol dynamic effects and the aerosol–radiation interaction seem to have only a minor influence on the volcanic ash mass loading. On 23 June the averaged AHI measurements show a more fragmentary ash distribution in Fig. 6.3 (b). This might be a result of volcanic cloud dilution in combination with deficiencies in the volcanic ash measurement of opaque regions. Most of the ash is measured between 50–55° N and around 180° E. The simulation results in Fig. 6.3 (d) and (f) support the assumption of the diluted volcanic cloud, as the mass loading only shows values smaller than 4 $\mathrm{g\,m^{-2}}$. For both simulated scenarios, the overall structure of the volcanic cloud is similar. However, differences prevail in location and absolute values of maximum mass loading. These differences are due to aerosol dynamics and radiative effects which are addressed in more detail in Sect. 6.3 and Sect. 6.4, respectively. Compared to these two simulations, the averaged AHI measurements in Fig. 6.3 (b) show values for the maximum ash mass loading that lie in between the two simulation scenarios. In panels (g) and (h) the differences between the two simulation scenarios are highlighted by the absolute difference of AERODYN-rad – no_AERODYN-no_rad. It shows that considering aerosol dynamics and aerosol–

Table 6.3: Comparison of daily mean column integrated mass of volcanic ash between AHI and ICON-ART results using the SAL method.

	2019-06-22			2019-06-23		
Scenario	S	A	L	S	A	L
AERODYN-rad	0.332	0.529	0.008	1.640	0.320	0.040
AERODYN-no_rad	0.126	0.470	0.006	1.506	0.136	0.027
no_AERODYN-rad	−0.089	0.887	0.015	1.580	0.704	0.031
no_AERODYN-no_rad	−0.170	0.829	0.015	1.543	0.740	0.030

radiation interaction results in lower volcanic ash mass loadings in most parts of the volcanic cloud." On the first day after the eruption, in the AERODYN-rad scenario, there is a slight northward shift of the volcanic cloud compared to the no_AERODYN-no_rad scenario. This results in positive values between 155–170° N in the difference plot.

So far, model results and observations were compared in a rather qualitative fashion. In the following, I evaluate the column integrated volcanic ash mass with the SAL method to compare the results in an objective manner. Wernli et al. (2008) introduced this metric and Wernli et al. (2009) extensively discuss its properties. Details about the method are given in Sect. 5.3.2. Here, I set the threshold value to identify objects for the SAL method to $R^* = 0.01$ g m^{-2}. Table 6.3 summarizes the SAL values for the comparison of the daily mean column integrated mass between ICON-ART results and the AHI retrieval. The same values are visualized in Fig. 6.4. Each of the markers in Fig. 6.4 represents one comparison between AHI and ICON-ART. As a reminder, a value of 0 indicates a perfect agreement between observation and model result. This would result in a dark purple marker located at the center of Fig. 6.4.

"The location of the volcanic cloud agrees very well with the observation for all dates in all simulation scenarios." This is indicated by the purple shades of the markers. Please note the logarithmic colorbar for the location value. The markers in Fig. 6.4 form two different clusters associated with the two dates. L values for the 23 June are generally higher than on 22 June, but they remain on a low level (< 0.1). The structure value significantly deviates from zero for most scenarios, especially on 23 June. This indicates a large difference between the structure of the simulated volcanic ash cloud and the observed one. However, the values of the different scenarios lay close to each other on the respective day. There is no significant influence of the aerosol dynamic processes or aerosol–radiation interaction visible on the structure value. "Only the amplitude values differ distinctly among the different scenarios. Simulations with AERODYN are closer to the observation than simulations without aerosol dynamics."

In ICON-ART simulations, the wind field is the main driver for the location of the volcanic cloud. During simulations, meteorological fields are not aligned with observational data. Consequently, it can occur that the wind field increasingly deviates from observations over time. Furthermore, AHI might have problems to measure the lower ash concentrations especially in opaque regions on 23 June, as discussed earlier. The center of mass in such a fragmentary satellite retrieval is difficult to determine

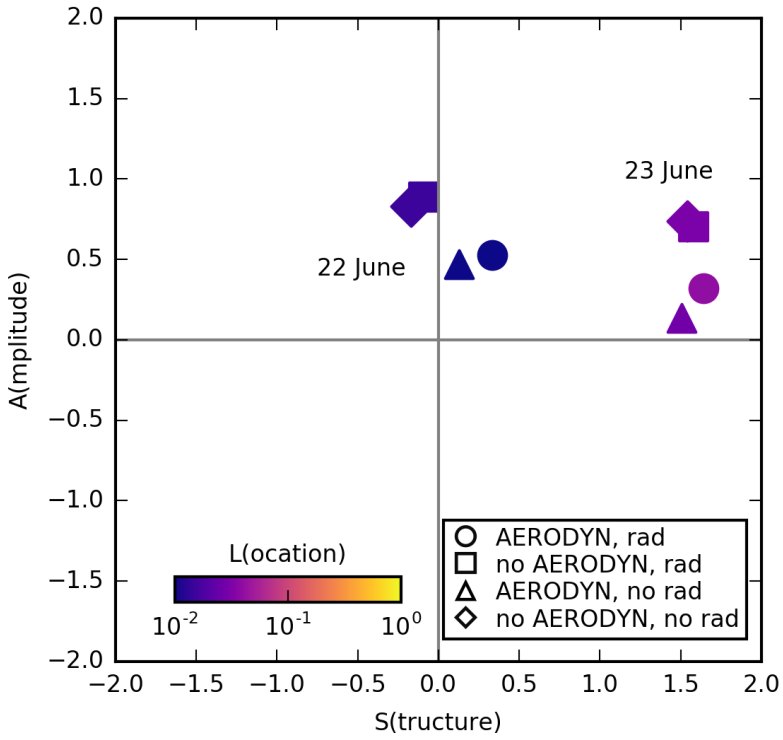

Figure 6.4: Visualization of SAL values for the comparison of ICON-ART results with AHI measurements. The different marker types indicate the simulation scenarios. The two clusters represent the two evaluated dates.

reliably. A combination of both reasons can explain the higher L values on 23 June. The detection limit of the satellite instrument and its deficiencies in measuring volcanic ash under cloudy conditions can be the reason for the rather large positive S values on 23 June. This quantifies the impression from Fig. 6.3 that the volcanic ash cloud in ICON-ART simulations covers a much larger area compared to the AHI measurement. Positive A values indicate that the model overestimates the column integrated mass compared to satellite observations. On the one hand, deficiencies in the satellite measurement could be a reason for this. On the other hand, the choice of eruption source parameters is crucial and can cause a general bias. In the simulations, the Raikoke volcano emits a total of 1.9×10^9 kg ash. However, AHI detects an total ash mass ranging between $0.4–1.8 \times 10^9$ kg. Since I am interested in the effects of aerosol dynamic processes on aerosol dispersion, the particular focus of this work lies on the difference between simulations with and without AERODYN. For the latter, the overestimation of column integrated ash mass is even more pronounced. This indicates that aerosol dynamic processes reduce the total ash mass in the model. Section 6.3 provides more details on this matter.

“The AHI and TROPOMI measurements give confidence in the simulated horizontal distribution of the volcanic cloud. Additionally, information about the vertical distribution of the volcanic cloud is retrieved from OMPS-LP and CALIOP data. OMPS-LP gives a clear signal of the volcanic cloud on 22 June 2019, 02:27 UTC shortly after the onset of the eruption. It locates the volcanic cloud at 49.76° N 154.1° E at

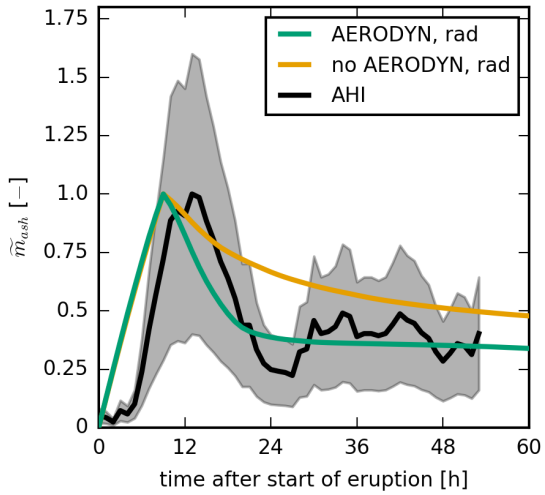

Figure 6.5: Normalized total volcanic ash mass $\widetilde{m}_{ash}$ over the time after the onset of the volcanic eruption on 21 June 2019, at 18:00 UTC. The green and yellow curve represent AERODYN-rad and no_AERODYN-rad, respectively. The black curve is based on AHI measurements with an error estimate in gray.

approximately 17 km. The ICON-ART model result (AERODYN-rad) shows a similar cloud top height which will be addressed in more detail in Sect. 6.4. Also the height of the volcanic cloud measured by CALIOP on 23 June 2019, agrees well with the model result." This is a topic of the following section.

6.3. Effect of Aerosol Dynamics

"So far mainly the ICON-ART model result of the AERODYN-rad scenario was discussed. In this section, it is compared with the no_AERODYN-rad scenario to study the influence of secondary aerosol formation and particle aging on volcanic aerosol dispersion."

The results of the SAL method suggest that aerosol dynamic processes lead to a reduction of volcanic ash mass in the simulations. To further investigate this behavior, the temporal evolution of volcanic ash mass in the atmosphere is examined and illustrated in Fig. 6.5. "The graph shows how the normalized total ash mass $\widetilde{m}_{ash}$ evolves over time after the onset of the volcanic eruption on 21 June 2019, at 18:00 UTC. Muser et al. (2020) define

$$\widetilde{m}_{ash}(t) = \frac{m_{ash}(t)}{\max(m_{ash}(t))}$$

with $m_{ash}(t)$ as the total observed volcanic ash mass at one measurement time or simulation time step. In the ICON-ART simulations, AERODYN-rad and no_AERODYN-rad, $\max(m_{ash}(t))$ is close to 1.9×10^9 kg. For the AHI retrieval $\max(m_{ash}(t))$ is estimated to range between 0.4×10^9 and 1.8×10^9 kg. Figure 6.5 shows $\widetilde{m}_{ash}$ for two different simulation scenarios, AERODYN-rad (green) and no_AERODYN-rad (yellow), and the AHI retrieval (black). The gray shading depicts an error estimate for the AHI measurement between $0.4\widetilde{m}_{ash}$ and $1.6\widetilde{m}_{ash}$.

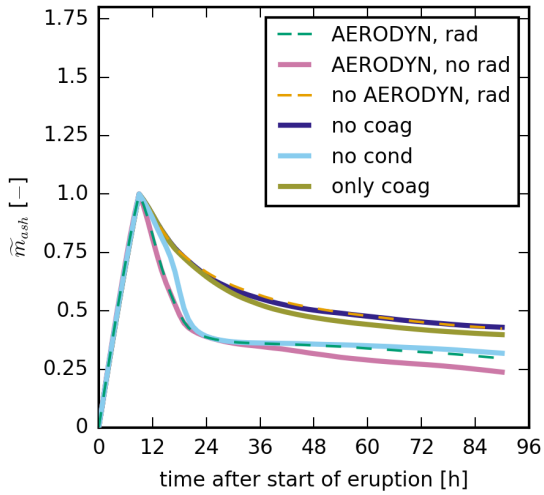

Figure 6.6: Normalized total volcanic ash mass $\widetilde{m}_{ash}$ over the time after the onset of the volcanic eruption on 21 June 2019, at 18:00 UTC. The dashed green and yellow curve represent AERODYN-rad and no_AERODYN-rad, respectively. The solid curves result from different simulation scenarios.

Both simulations and the satellite measurement agree very well over the course of the first 9 h. This is the eruption phase of the Raikoke volcano." There was no continuous eruption of the Raikoke volcano during these 9 h. This is visible as the small-scale variations in the AHI measurement during the eruption phase. In contrast to that, the simulated eruption uses a continuous emission of volcanic ash. This can explain the offset between observation and simulation. Bruckert et al. (2021) discuss this phase of the eruption in more detail and show a method to reduce this offset. The major and mainly "continuous eruption of Raikoke occurred between 21 June 2019, 22:40 UTC and 22 June, 02:00 UTC, with several additional outbursts before and after this period. While in the simulations a constant and continuous eruption is assumed.

After the end of the eruption, the observed ash mass (black) decays to less than 50 % over the course of 12 h. Thereafter, the total volcanic ash mass seems to stabilize. The small-scale variations in the observation might be due to deficiencies or limitations of the retrieval algorithm, as no new ash is emitted during this period. A very similar decay and stabilization of ash mass can be observed for the AERODYN-rad scenario in green. The result suggests that the necessary sink processes are represented by the new aerosol dynamics module AERODYN. The same are missing in no_AERODYN-rad, for which the volcanic ash mass decays much slower. It can be deduced that secondary aerosol formation and particle aging, due to condensation and coagulation, are essential processes for the correct simulation of volcanic aerosol dispersion. These processes largely influence the transported aerosol concentrations. Additionally, it should be noted that the prevailing settling mechanism of aerosol after the Raikoke 2019 eruption for all the simulation scenarios is due to sedimentation. Dry deposition is only relevant for aerosol near the ground. Wet deposition should also play a minor role during the first days after the eruption, as most of the volcanic ash is emitted above cloud level."

The AERODYN module comprises several different processes. The investigation of three additional scenarios, no_coag, no_cond, and only_coag, reveals the relevance of single aerosol dynamic processes for the rapid removal of volcanic ash. Figure 6.6 shows the corresponding results. The dashed lines depict the previously shown curves of the AERODYN-rad and the no_AERODYN-rad scenario. The solid lines represent the additional simulation scenarios. After the end of the eruption, the lines separated into two groups. On the one hand, no_coag and only_coag closely follow the no_AERODYN-rad scenario. On the other hand, the results of no_cond and AERODYN-no_rad remain close to the line of the AERODYN-rad scenario.

The total ash mass in the simulation without condensation (light blue curve) shows only small differences to the one of the AERODYN-rad scenario. These differences are restricted to the first few hours after the end of the eruption and to the long-term development. Consequently, condensation of gaseous species on volcanic ash particles plays only a minor role in the removal of ash. In contrast to that, in the simulation without coagulation (purple curve), the total ash mass behaves as in the no_AERODYN simulation. This shows that coagulation plays a key role in the removal of ash. The opposite, however, is not true. The only_coag simulation scenario for which all aerosol dynamic processes, condensation, nucleation, and ISORROPIA are switched off, shows no enhanced removal of volcanic ash. The olive colored curve in Fig. 6.6 shows this behavior. In this scenario, only ash particles participate in coagulation, but no secondary volcanic aerosols are formed. This leads to only a slightly enhanced removal of volcanic ash compared to the simulation with no aerosol dynamic processes. The results indicate that the coagulation of ash particles with secondary volcanic aerosols, sulfate particles, is the main driver for the rapid removal of volcanic ash after the Raikoke eruption.

Additionally, the light purple curve indicates that neglecting aerosol–radiation interaction leads to a lower ash mass in the atmosphere. This particularly applies on the long-term ash mass development. Section 6.4 addresses this issue in more details.

So far, only the development of the total volcanic ash mass was shown over time. Fig. 6.7 (a) depicts the ash mass per aerosol mode for the AERODYN-rad scenario. Analogously, panel (b) displays the total number of particles for each ash containing mode. Colors distinguish between the sizes of the modes and the line style indicates the mixing state. Solid lines represent insoluble modes and dashed lines mixed modes. Both panels illustrate that especially the quick sedimentation of coarse and giant mode particles is responsible for the fast removal of volcanic ash after the end of the eruption. In contrast, the accumulation mode remains more or less in the atmosphere. Only insoluble ash particles shift into the mixed accumulation mode. That means that soluble substances such as water and sulfate form a coating on these accumulation mode ash particles over time. In the coarse mode, particles also get coated and form a mixed mode. However, the mixed coarse mode falls out rather quickly together with the insoluble coarse mode particles. The total particle number of ash containing modes shows a similar behavior as shown in panel (b). Here, also the different orders of magnitude in particle number for the different modes become visual. Although the emitted ash mass per size mode is identical, due to the different

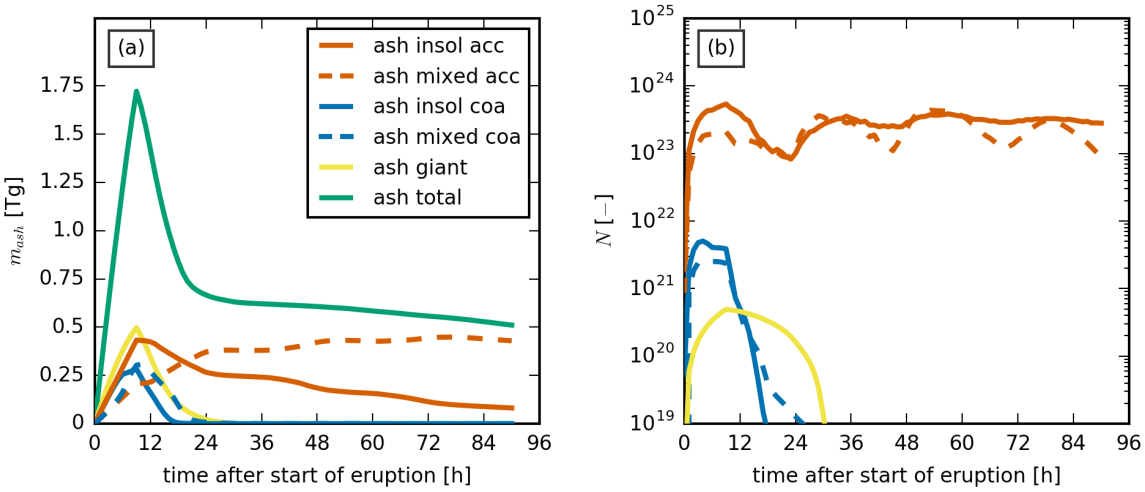

Figure 6.7: Absolute total volcanic ash mass m_{ash} in panel (a) and total particle number in panel (b) over the time after the onset of the volcanic eruption on 21 June 2019, at 18:00 UTC. The results are derived from the AERODYN-rad scenario. Different colors represent different ash containing aerosol modes.

particle diameters, the resulting numbers differ significantly. One feature I would like to highlight here, is the quicker removal of coarse mode particles compared to giant mode particles. As the latter do not participate in aerosol dynamic processes in the simulations, their size cannot increase over time. Coarse mode ash, however, can coagulate, hence, form larger particles or build up a soluble shell. This results in larger particles that sediment faster. The results in Fig. 6.7 suggest that these aged coarse mode particles sediment even faster than (unaged) giant mode particles.

The enhanced removal of volcanic ash due to sedimentation must also result in a different vertical distribution of the ash cloud. CALIOP measurements serve here as a comparison in the evaluation of the vertical structure of the model results. "The CALIPSO satellite passed over the volcanic cloud on 23 June 2019, at around 15:00 UTC. On this date, the satellite ground track clearly intersects the modeled volcanic cloud, as shown in Fig. 6.8 (a). This 2D map depicts the volcanic cloud top height of accumulation mode ash particles calculated with ICON-ART (AERODYN-rad). In this connection, a threshold of 0.01 µg ash per kg air defines the volcanic cloud top. The map shows a maximum volcanic cloud top height in the range of 17–19 km under the CALIPSO ground track at around 50° N." Figure 6.8 (b) shows the CALIOP measurement of the total attenuated backscatter at 532 nm. It indicates volcanic aerosols in a region between 49° N and 51° N at an altitude between 15 and 16 km, as highlighted by the magenta circle. This part of the signal was identified as volcanic ash by the CALIOP retrieval algorithm. Fig. 6.8 (c) illustrates the attenuated backscatter at 532 nm of volcanic aerosols on 23 June for the 15:00 UTC model output (AERODYN-rad). Displayed is the result of ICON-ART model columns along the CALIPSO ground track. The calculation of the attenuated backscatter from model fields is based on simulated ash and sulfate concentrations together with their optical properties. For the ease of

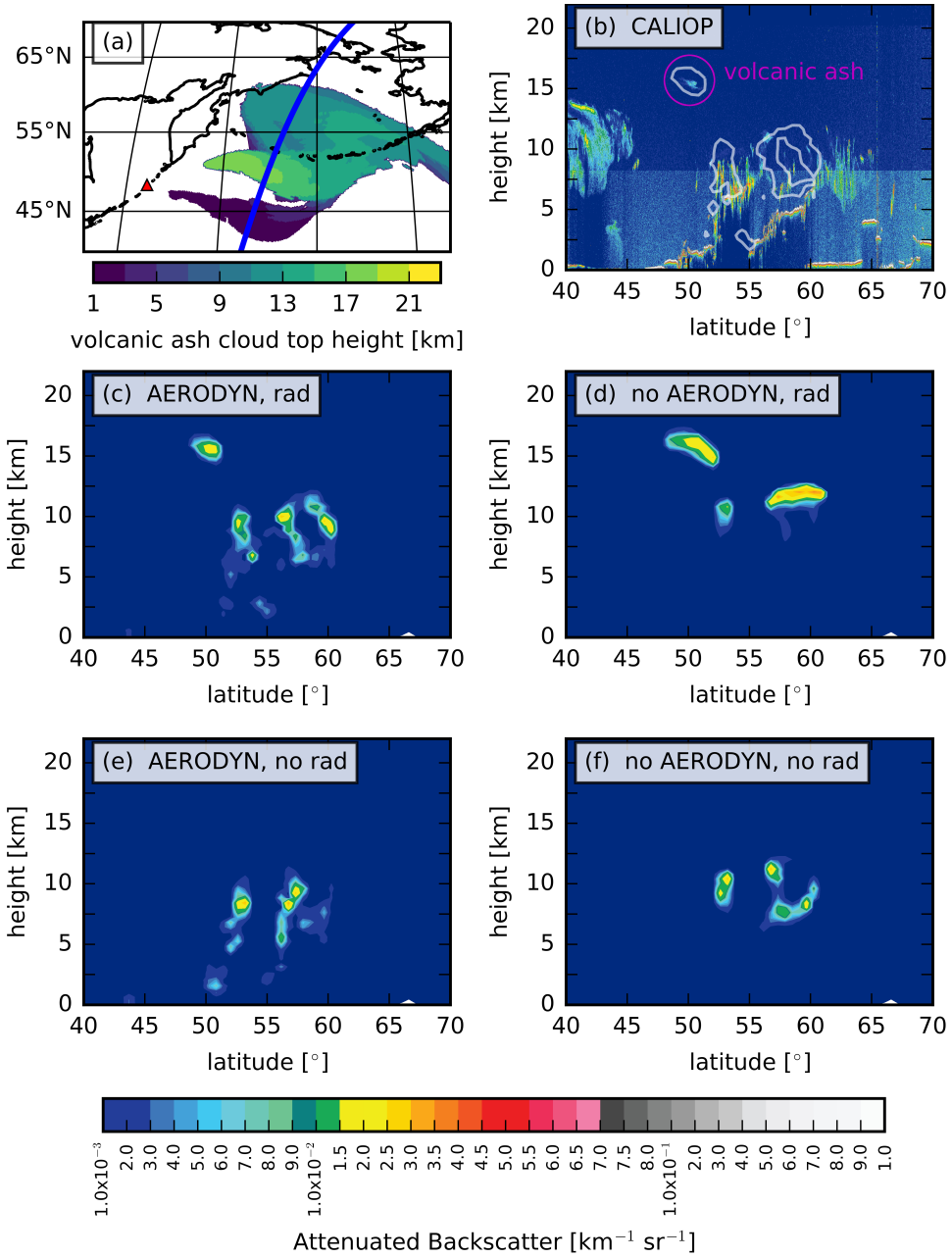

Figure 6.8: (a) CALIPSO ground track on 23 June 2019, around 15:00 UTC in blue color and location of Raikoke volcano as red triangle. The contour map shows the volcanic ash cloud top height for the AERODYN-rad scenario. (b) The CALIOP attenuated backscatter for 532 nm for the satellite position between 40° N and 70° N. Highlighted by the magenta circle is the part of the signal that was identified as volcanic ash by the CALIOP retrieval algorithm. The white line shows the 0.002 km^{-1} sr^{-1} contour of AERODYN-rad at 15:00 UTC. (c – f) Total attenuated backscatter for 532 nm of volcanic aerosols under the CALIPSO ground track on 23 June 2019, for the 15:00 UTC model output are displayed. (c) shows the result for AERODYN-rad, (d) for no_AERODYN-rad, (e) for AERODYN-no_rad, and (f) for no_AERODYN-no_rad.

comparison between measurement in Fig. 6.8 (b) and AERODYN-rad result in Fig. 6.8 (c), the white "line in panel (b) shows the 0.002 km^{-1} sr^{-1} contour of the model result in panel (c).

The AERODYN-rad simulation result captures the most prominent feature of the CALIOP retrieval between 49° N and 51° N at a height around 16 km. Here, the model shows a clear maximum in total attenuated backscatter of volcanic aerosol." Furthermore, the white contour lines indicate that several other peaks of the modeled attenuated backscatter signal north of 51° N is co-located with CALIOP measurements. I would assume that the CALIOP signal in this region shows to some extent volcanic aerosols. This comparison shows the potential of using simulation results for the interpretation of satellite retrievals.

One remark on the related attenuated backscatter figure in Muser et al. (2020): In Muser et al. (2020), the attenuated backscatter signal in panel (c) and (e) shows a feature at around 44° N close to the surface. The CALIOP measurement in panel (b) exhibits a similar signal in this region. In this thesis, Fig. 6.8 (c) does not contain this feature anymore. However, the volcanic cloud top height in panel (a) shows that there is low level volcanic aerosol present in the AERODYN-rad scenario. This leads to the conclusion, that the volcanic aerosol concentration in this low altitude branch of the volcanic cloud is now lower than in the previous simulation of Muser et al. (2020). Nevertheless, I would still argue that volcanic aerosols are the cause for the attenuated backscatter signal at 44° N and about 3 km altitude in the CALIOP measurement.

"Comparing AERODYN-rad in Fig. 6.8 (c) with no_AERODYN-rad in Fig. 6.8 (d) shows the distinct effect of aerosol dynamics on the vertical distribution of the volcanic cloud. No_AERODYN-rad catches the main feature between 49° N and 51° N at a height up to 17 km. However, the volcanic aerosol layer extends significantly further north, up to 53° N. This is in contrast to the CALIOP signal in Fig. 6.8 (b). Also the smaller patterns in lower altitudes and higher latitudes are missing in the no_AERODYN-rad scenario. ...Without aerosol dynamics, most of the aerosol stays at one height level, whereas with aerosol dynamics, the particles get mixed down to lower altitudes. Coagulation of particles and condensation of sulfate and water onto existing particles increase the aerosol mass. Hence, these particles sediment faster and, therefore, are removed from the atmosphere more efficiently.

A similar conclusion can be derived from the AERODYN-no_rad and no_AERODYN-no_rad scenarios in Fig. 6.8 (e) and (f), respectively. Although both are missing the most prominent feature between 49° N and 51° N at around 16 km, they show the same behavior in terms of aerosol dynamic effects."

With AERODYN, enhanced downward mixing results in a better agreement between simulation results and CALIOP measurements in terms of the vertical distribution of volcanic aerosol. Appendix B includes further CALIOP measurements on other dates together with the corresponding ICON-ART results.

I would like to shortly comment on the assumptions that were made to determine the optical properties of the particles in the ICON-ART simulations. As described in Sect. 3.7, the optical properties of each aerosol mode are based on the assumption of spherical particles, with a fixed chemical composition, coating ratio, and particle diameter. However, volcanic ash consists of non-spherical particles (Bagheri

and Bonadonna, 2016) and aerosol dynamic processes change composition, coating ratio, and particle diameters over time. This results in deviations from the assumptions made and, consequently, in a different amplitude of the attenuated backscatter signal of simulated volcanic ash. As Hoshyaripour et al. (2019) have shown for mineral dust, the non-sphericity of particles can have a considerable impact. The backscattering ability of randomly oriented non-spherical particles is significantly lower compared to that of spherical particles (Mishchenko et al., 1997). Consequently, the absolute values of the attenuated backscatter signal in Fig. 6.8 (c) to (f) might be lower if the non-sphericity of ash particles is included. This characteristic can be an explanation for the higher amplitude in the attenuated backscatter signal of ICON-ART results compared to the CALIOP measurement in Fig. 6.8.

6.4. Effect of Radiative Interaction

"In contrast to aerosol dynamics, aerosol–radiation interaction does not largely influence the horizontal aerosol concentrations after the Raikoke eruption." This is a conclusion from the SAL analysis in Fig. 6.4. The comparison of simulation scenarios in which only the setting for the radiation interaction differs, suggest only minor differences in the amplitude of the volcanic ash mass. "However, there are differences in the mass loading $\overline{\Gamma}_{ash}$ patterns that can be explained by radiative effects. This is already somewhat indicated by the S value in Table 6.3. The S values of simulation scenarios with the same radiation interaction setup are closer to each other compared to the other scenarios." In contrast to that, the light purple curve in Fig. 6.6 indicates that aerosol–radiation interaction increases the lifetime of volcanic ash in the atmosphere.

An analysis of the maximum height that is reached by the volcanic cloud over time follows in this section. It provides a more detailed insight into the influence of aerosol–radiation interaction on volcanic aerosol dispersion. "A volcanic cloud that is lifted up in the atmosphere has a longer lifetime. Hence, it can be transported over longer distances, remains a hazard for aircraft over a longer period of time, and has longer lasting climatic effects. Additionally, the height of the volcanic cloud in the atmosphere also influences its transport, as wind speed and direction can differ between height levels. Figure 6.9 (a) and (b) show the height of the volcanic cloud top over the course of time after the onset of the volcanic eruption. A threshold value is used to determine the extent of the volcanic cloud in the model result. Model grid boxes with an ash concentration above this threshold are considered as part of the volcanic cloud. For each mode this threshold is set to" 10000 ash particles per kg air. Different colors in Fig. 6.9 (a) and (b) indicate the four different scenarios. The upper and lower panel show the volcanic cloud top height of ash particles in the accumulation and coarse mode, respectively. In simulations with aerosol dynamic processes, for both (size) modes the higher top height of either the insoluble or the mixed mode is used. "Comparing the yellow (no_AERODYN-rad) with the green curve (AERODYN-rad), the influence of the aerosol dynamic processes on the maximum volcanic cloud top height can be seen. For both, the accumulation and the coarse mode the volcanic cloud top height is lower for the scenario with AERO-

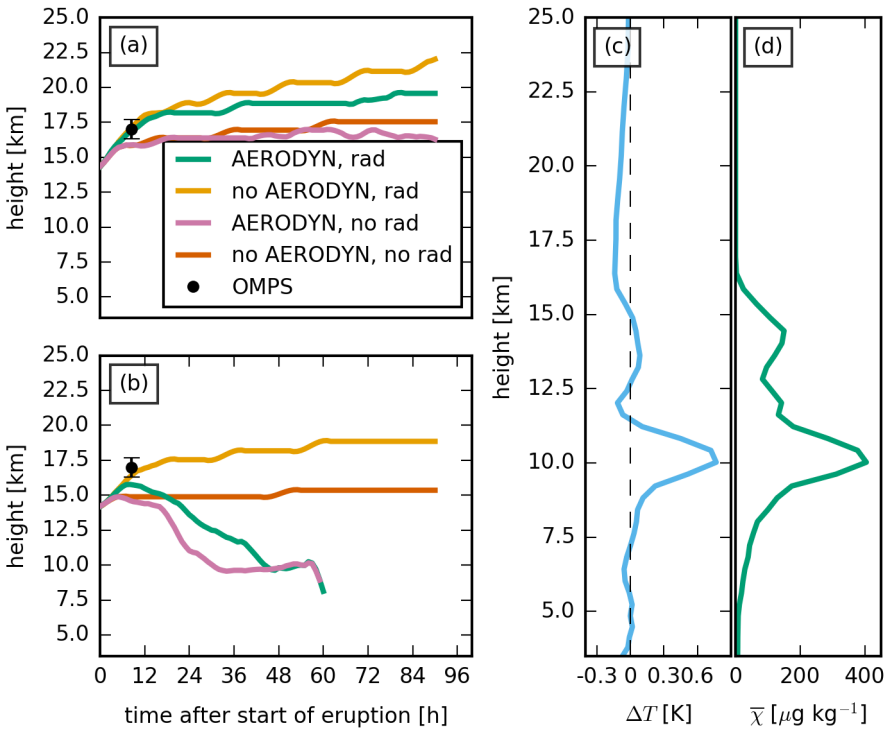

Figure 6.9: (a, b) Evolution of height of volcanic ash cloud top after the onset of the eruption on 21 June 2019, at 18:00 UTC. The yellow curve represents the no_AERODYN-rad scenario, the green curve AERODYN-rad, the pink one AERODYN-no_rad, and the orange one represents the no_AERODYN-no_rad scenario. Panel (a) shows the ash cloud top of particles in the accumulation mode, (b) of particles in the coarse mode. The black circle depicts the volcanic cloud top height obtained from OMPS-LP. (c) Mean temperature difference (AERODYN-rad – AERODYN-no_rad) in volcanic ash cloud columns on 23 June 2019, 12:00 UTC. (d) Mean volcanic ash concentration $\overline{\chi}$ for the same model columns as in (c) for AERODYN-rad.

DYN. This result agrees with the backscatter signal of the same two simulation scenarios in Fig. 6.8. Due to aerosol dynamic processes particles grow in size as they age over time. Hence, the volcanic cloud is located at lower altitudes. This effect is more pronounced for the larger and therefore heavier coarse mode particles. Due to their larger surface, the condensation of sulfate onto them is more efficient compared to accumulation mode particles. The result indicates that for coarse mode ash the aging process is the determining factor of whether the volcanic cloud rises higher or sinks. The ash cloud top height of coarse mode ash particles in no_AERODYN-rad continuously rises up to more than 20 km. In contrast, the ash cloud top height in AERODYN-rad gradually sinks during the following 50 h (after reaching its peak). The graph for the AERODYN-rad and the AERODYN-no_rad scenario stops after around 60 h. This behaviour can be explained by the evaluation method. The aged coarse mode particles sediment out and reduce their concentration significantly. Eventually, the concentration decreases to the same order of the threshold value that is used to determine the volcanic cloud. From this point onward, the maximum volcanic cloud top height cannot be determined reliably anymore.

Even more pronounced than the aerosol dynamic effect, the influence of radiative effects on the volcanic cloud dispersion can be seen in Fig. 6.9. A distinct difference prevails between the two scenarios with

radiative interaction (yellow and green curve) and the two without radiative interaction (pink and orange curve). Accumulation mode ash particles stay more or less at the initial maximum height level (14 km) in case they do not interact with radiation. On the contrary, the ash cloud top rises up to 20 km altitude in the two scenarios with radiative interaction over the first four days after the onset of the eruption. Furthermore, the graph for accumulation mode ash particles indicates that the aerosol aging reduces the lifting effect induced by radiative interaction. The reason for this is an increased sedimentation velocity due to larger particles. Hence, pure ash particles are lifted higher compared to aged ash particles.
The described behavior is even more pronounced for coarse mode ash particles, shown in Fig. 6.9 (b). Especially for the simulated scenario with no radiative interaction, but aerosol dynamic processes (pink curve), the ash particles sediment out" the fastest compared to the other three simulation scenarios. Almost no increase of the volcanic cloud top height is visible for this scenario after the onset of the eruption. On the contrary, a lifting of the volcanic cloud top height is visible in the two simulations with radiative interaction during the first 12 h. Afterwards, particle aging gets more dominant for coarse mode ash particles. In the no_AERODYN-no_rad simulation scenario (orange line), like for accumulation mode particles, coarse mode particles remain more or less at the same altitude.
"A direct effect of the radiative interaction is shown in Fig. 6.9 (c) and (d) exemplarily for the model result of 23 June 2019, 12:00 UTC. The graph in (c) depicts the horizontally averaged atmospheric temperature difference ΔT between AERODYN-rad and AERODYN-no_rad at different heights. For the averaging approach, only model columns which contain a volcanic ash mass loading $\Gamma_{ash} > 0.01$ g m^{-2} in both scenarios are considered. Figure 6.9 (d) illustrates the horizontally averaged volcanic ash concentration $\overline{\chi}$ at different heights for the AERODYN-rad scenario. For this averaging exactly the same model columns, as used for the temperature difference, are considered. The curve of the temperature difference shows one distinct peak at around 10 km. Here, the simulation which considers aerosol–radiation interaction exhibits more than 0.6 K higher air temperature. The peak co-locates with the maximum in volcanic ash mass mixing ratio. In this height, the volcanic ash leads to an increased absorption of solar and thermal radiation, hence, it heats the surrounding air. This leads to a vertical velocity perturbation Δw. To further investigate this perturbation, the difference in vertical velocity between the AERODYN-rad and AERODYN-no_rad scenario during the first 12 h after the eruption is analyzed. Only grid cells in model columns which contain a volcanic ash mass loading $\Gamma_{ash} > 0.01$ g m^{-2} in both scenarios are considered. Locally, Δw reaches 0.19 m s^{-1} with a 98th percentile of 0.05 m s^{-1}. This agrees well with the vertical lifting of the volcanic cloud top height of around 3 km during the first 12 h ($\overline{w} = 0.07$ m s^{-1}).
The comparison of the four simulated scenarios with the OMPS-LP retrieval indicates that considering aerosol–radiative effects is essential to simulate volcanic aerosol dispersion correctly. This concerns already the first four days after the start of the eruption. Especially the simulated height of the accumulation mode particle's cloud top in Fig. 6.9 (a) agrees very well with the measured height. It should be noted that the OMPS-LP measurement gives the volcanic cloud height at one (horizontal) position. The maximum volcanic cloud top height is not necessarily co-located with this measurement position.

However, at this early stage during the eruption phase the volcanic cloud is not distributed over a large area yet. That is why it can be assumed that the volcanic cloud top height does not differ significantly in horizontal direction. Additionally, the ICON-ART model result shows the maximum volcanic cloud top height in proximity to the location of the satellite measurement. Based on the simulation result, it can be concluded that mainly accumulation mode particles are present at the top of the volcanic cloud. These particles are in the size of 0.1 µm."

Earlier in Sect. 6.3 it was mentioned that the two no_rad scenarios in Fig. 6.8 (e) and (f) miss the most prominent feature of the CALIOP measurement between 49° N and 51° N at an altitude of 15 to 16 km. My results show that the uplifting of particles due to radiation interaction is the reason for this behavior. As a reminder, volcanic ash and SO_2 are emitted between 8 and 14 km altitude in the simulations (see Sect. 6.1). The aerosol–radiation interaction with the consequent heating of the surrounding air lifts part of the volcanic aerosol cloud. On the contrary, in no_rad simulations the volcanic aerosol cloud does not reach altitudes higher than the initial 14 km (see Fig. 6.8 (e,f)). The same can be observed on other dates in Appendix B.

Many (recent) studies focus on an accurate as possible formulation of the eruption source parameters (e.g., Eckhardt et al., 2008; Kristiansen et al., 2010; Moxnes et al., 2014; de Leeuw et al., 2021; Bruckert et al., 2021). They argue that the emission height together with the emission profile are crucial for the correct simulation of the volcanic aerosol and SO_2 transport. This can strongly influence the horizontal transport, as wind speed and direction can differ with height. The altitude at which volcanic aerosols are present, has also a strong impact on their atmospheric lifetime. However, most of the aforementioned studies ignore aerosol dynamic processes and aerosol–radiation interaction. Especially the missing lifting of the volcanic cloud due to radiative heating is then compensated by emissions into higher altitudes (e.g., de Leeuw et al., 2021). My results show that even with a rather simplistic emission parametrization, but accounting for aerosol dynamic effects and aerosol–radiation interaction, the vertical structure of the volcanic aerosol distribution can be simulated in ICON-ART.

7. Potential of Data Assimilation for Volcanic Aerosol Dispersion Forecast

I applied the newly developed ART En-Var method (Sect. 5.2) to generate an analysis state from which a volcanic aerosol dispersion forecast is started. As for the investigation on the effect of aerosol dynamic processes and aerosol–radiation interaction, I used the Raikoke eruption of 2019 as a case study. Section 7.1 explains the setup of the data assimilation experiment. Section 7.2 contains results of the assimilation. Additionally, the advantage of the ART En-Var over the 2D-Var method is discussed. Concluding, Sect. 7.3 contains a discussion on the influence of the ART En-Var method on the aerosol dispersion forecast.

The data assimilation experiment was conducted within *bacy* (basic cycling). *Bacy*, like *datools*, is a script package developed at DWD. It is used to set up and run data assimilation experiments. It cycles for a given time period between data assimilation and model run. That means, model runs are interrupted usually every three hours to assimilate observational data. Subsequently, another three hour model run starts from the analysis field.

In the context of this thesis I extended bacy to make it capable of running data assimilation experiments for volcanic aerosol dispersion forecasts. For this purpose, I had to include the handling of volcanic aerosol. Furthermore, I adjusted the automatic run script generation of *bacy* to account for the newly implemented AERODYN module in ICON-ART.

7.1. Data Assimilation Experiment Setup

The assimilation of volcanic ash data aims to overcome uncertainties in the eruption source parameters. This is the reason why the data assimilation experiment is designed in a way as if the emission rate of volcanic ash during the Raikoke eruption is not known. The ICON-ART setup for the data assimilation experiment corresponds in large parts to the AERODYN-rad scenario as described in Sect. 6.1. Only the spatial and temporal resolution as well as the emission rate of volcanic ash differ. Additionally, the ISORROPIA module is turned off[1], but all other aerosol dynamic processes are still considered. The horizontal resolution in ICON-ART is reduced to $\Delta\overline{x} = 40$ km. At this horizontal resolution a time step of $\Delta t = 360$ s is used. The emission rate of volcanic ash in the data assimilation experiment is reduced by a factor of almost two, compared to the simulations of Sect. 6. This reduced emission introduces an artificial uncertainty into the model simulation. Each volcanic ash mode is emitted at a rate

[1] The compiler on the DWD HPC system has problems with the ISORROPIA module, that is why I could not use it for the data assimilation experiment.

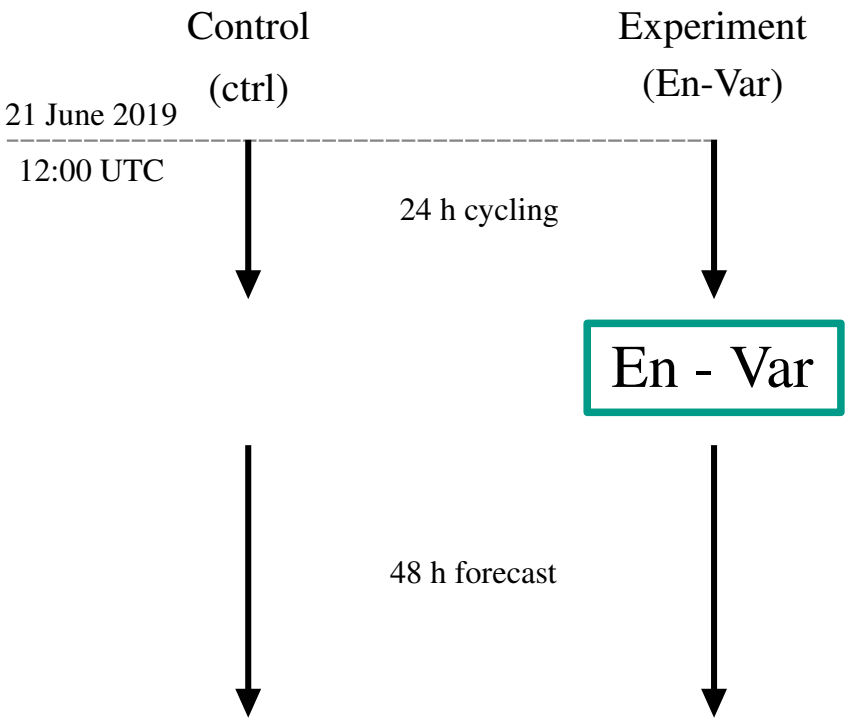

Figure 7.1: Setup of data assimilation experiment with one control (ctrl) and one En-Var simulation.

of 1.65 $\mathrm{kg\,s^{-1}\,m^{-1}}$. The emission profile between 8 and 14 km and the 9 h eruption period remain the same as in the simulations of Sect. 6.

The schematic in Fig. 7.1 shows a set of two experimental runs. Both runs start on 21 June 2019 at 12:00 UTC. They are initialized from the uninitialized analysis product for incremental analysis update (IAU) (Bloom et al., 1996; Polavarapu et al., 2004). ART variables are initialized as a clean atmosphere. During the first 24 h of simulation a cycling with a 3 h interval is performed. That means, ICON-ART is integrated for 3 h with a subsequent assimilation of atmospheric variables. These assimilation steps still ignore aerosol and trace gases. From the resulting analysis field the atmospheric variables are initialized and another 3 h model run is performed. At these intermediate reinitializations, the ART variables are initialized from the previous fields. The ART variables also don't participate in the IAU initialization.

After the 24 h cycling period, the ART En-Var method is used to assimilate volcanic ash. Due to the characteristics of the IAU method for the atmospheric variables, a new model run is started 1.5 h before the actual intended start date. As an example, if a forecast run is intended to start at 12:00 UTC, ICON-ART starts at 10:30 UTC performing the IAU. For that reason, the assimilation of volcanic ash is performed on 22 June 2019 at 10:30 UTC.

I use the filtered column integrated volcanic ash mass of the AHI instrument (compare Sect. 4.3) for the assimilation. The mean of two datasets, at 10:00 and 11:00 UTC, is used to approximate the 10:30 UTC observation. The observational data needs to be transferred to the model grid. As the spatial resolution of the satellite retrieval is finer than the model grid, each ash containing satellite pixel is assigned to the nearest model grid cell. The mean of all satellite pixels in one model grid cell determines the value of the

Table 7.1: Ensemble setup for data assimilation experiment. Member ens_01 is used for the deterministic forecast.

Ensemble member	Top height [km]	Bottom height [km]
ens_01	14	8
ens_02	12	6
ens_03	10	4
ens_04	8	2
ens_05	6	0
ens_06	16	10
ens_07	18	12
ens_08	20	14
ens_09	22	16

cell. Note that only satellite pixels which contain ash are considered for the mean. Fig.7.2 (b) displays the resulting column integrated ash mass that has been transferred on the model grid.
For the ART En-Var method I use an ensemble consisting of nine ensemble members. Ensemble member ens_01 also represents the first guess and is used for the deterministic forecast after the assimilation. The members ens_01 to ens_09 only differ in the emission height of volcanic ash. All other variables are initialized with the same values. Table 7.1 lists the emission height for volcanic ash and SO_2.
The deterministic forecast is started on 22 June 2019 12:00 UTC. As described above, for the initialization of aerosol the analysis field at 10:30 UTC is used. The deterministic forecast is run for 48 h. As displayed in the schematic of Fig. 7.1, two free running model runs are performed. One is initialized from the analysis state of the ART En-Var assimilation. The other (ctrl) is initialized from the first guess state.
In the scope of this work, the data assimilation experiment focuses on volcanic ash. That is why the following evaluations relate to ash only.

7.2. Results of the Assimilation

This section presents the input fields for the ART En-Var method, first guess and ensemble mean together with the results of the assimilation. Additionally, some advantages of the ART En-Var method over the simpler 2D-Var method are discussed. For the assimilation I use a localization of the model error covariance with $\sigma_C = 0.9$ and assume the observation error as $r = 10^{-5}$.
Figure 7.2 presents the input fields for and the result of the assimilation with the ART En-Var method. All four panels display the column integrated ash mass Γ_{ash}. Figure 7.2 (a) shows the first guess $\mathbf{x_b}$ and the ensemble mean $\overline{\mathbf{x}}$ in panel (c). Figure 7.2 (b) displays the averaged and remapped AHI data $\mathbf{y}$. All

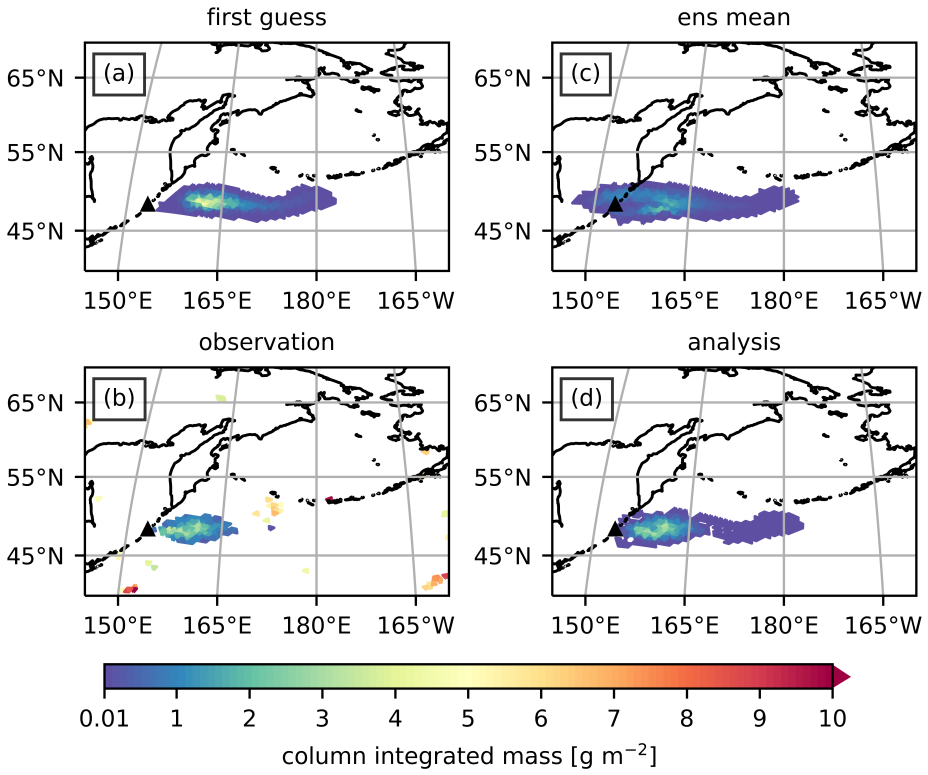

Figure 7.2: First guess (a), ensemble mean (c), observation (b), and analysis (d) of column integrated ash mass Γ_{ash} on 22 June 2019 at 10:30 UTC. The analysis state is the result of the ART En-Var assimilation. The black triangle marks the location of the Raikoke volcano.

three are input fields for the ART En-Var assimilation. The resulting analysis state $\mathbf{x_a}$ is shown in panel (d).

The volcanic ash cloud is still located close to the volcano (black triangle) in the first guess on 22 June 2019 at 10:30 UTC. Some parts of the cloud stretch as far as 180° E. The maximum in the column integrated ash mass is located around 10° east of the volcano. The contour of the ensemble mean in Fig. 7.2 (c) looks similar to the first guess, especially east of the volcano. However, the volcanic cloud in the ensemble mean covers a larger area around the volcano. The cloud even stretches towards the west of Raikoke. Similarly, the maximum column integrated mass in the ensemble mean spreads over a larger area. This spread over a larger area shows that the ash is transported in different directions in the different ensemble members.

The size of the volcanic cloud in the AHI observation, Fig. 7.2 (b), is much smaller compared to the first guess. The observation locates the ash cloud between Raikoke and around 166° E. The maximum column integrated mass is in the same order of the values given in the first guess, however, the location of the maximum is significantly closer to the volcano. At most locations where the satellite detects the volcanic ash cloud, the first guess also contains ash. It is also noticeable that almost no values < 1 g m^{-2} are observed by the satellite. This is in contrast to the volcanic cloud in the first guess. Hence, it suggests

that the satellite instrument has difficulties to detect some parts of the volcanic cloud. Furthermore, the observation contains pixels with a very high column integrated ash mass > 5 g m^{-2}. These clusters of few pixels seem to be randomly distributed in regions where volcanic ash is not expected. Most of these data points even exhibit higher values than measured in the center of the volcanic plume. This is why I assume these high values as noise. A short discussion on why these values are not visible in the analysis state in Fig. 7.2 (d) is provided later in this section.

The analysis state in Fig. 7.2 (d) visualizes the effect of the ART En-Var assimilation. The signature of the observed ash cloud is visible. In regions where no volcanic ash is observed by AHI, the ash concentration of the first guess is reduced. This analysis state is used for the volcanic ash forecast in Sect. 7.3.

To quantify this subjective impression on the visualization of the assimilation, I calculate the Euclidean norm, the l^2 norm. It can be interpreted as the length of a vector. The norm of the difference between observation – first guess and observation – analysis state is $\|\mathbf{y} - H\mathbf{x_b}\|_2 = 73.65$ and $\|\mathbf{y} - H\mathbf{x_a}\|_2 = 71.35$, respectively. The lower value of $\|\mathbf{y} - H\mathbf{x_a}\|_2$ shows that the analysis state is closer to the observation $\mathbf{y}$ than the first guess is to $\mathbf{y}$. The high absolute values (> 70), however, result from the randomly distributed data points of high value in the observation. When I remove these high values from the observation, the norm decreases to $\|\mathbf{y} - H\mathbf{x_b}\|_2 = 17.93$ and $\|\mathbf{y} - H\mathbf{x_a}\|_2 = 5.28$. Now the values clearly show that the analysis state $\mathbf{x_a}$ came closer to the observation $\mathbf{y}$ than the first guess $\mathbf{x_b}$.

The reader might wonder why the data points with high column integrated ash mass outside the volcanic cloud are not visible in the analysis state, Fig. 7.2 (d). This behavior is related to a characteristic of the ART En-Var method, which is shortly discussed in the following. For comparison, Fig. 7.3 shows results of the simpler 2D-Var assimilation.

The left column displays the remapped and averaged AHI data, the right column the resulting analysis state $\mathbf{x_a}$ of column integrated ash mass Γ_{ash} on 22 June 2019 at 10:30 UTC. The assimilation shown in the top row is performed with the same observational data as the ART En-Var assimilation before. Now, the resulting analysis state, Fig. 7.3 (c), contains the signature of these data points with high values. Due to the Gaussian localization matrix, the data points are not visible as single points anymore, but $\mathbf{y} - H\mathbf{x_b}$ is distributed spatially around the point of measurement. Moreover, the analysis state in Fig. 7.3 (c) seems to contain almost no information of the first guess east of 166° E. This is in contrast to the analysis state of the ART En-Var method.

To get rid of the spurious observation points, a quality control measure is necessary. Therefore, an observation at index i

$$y_i = \begin{cases} y_i\,, & \text{if } |y_i - x_{bi}| \leq 3 \text{ g m}^{-2} \\ x_{bi}\,, & \text{otherwise} \end{cases} \tag{7.1}$$

is replaced with the value of the first guess x_{bi} in case the difference of the two becomes larger than 3.

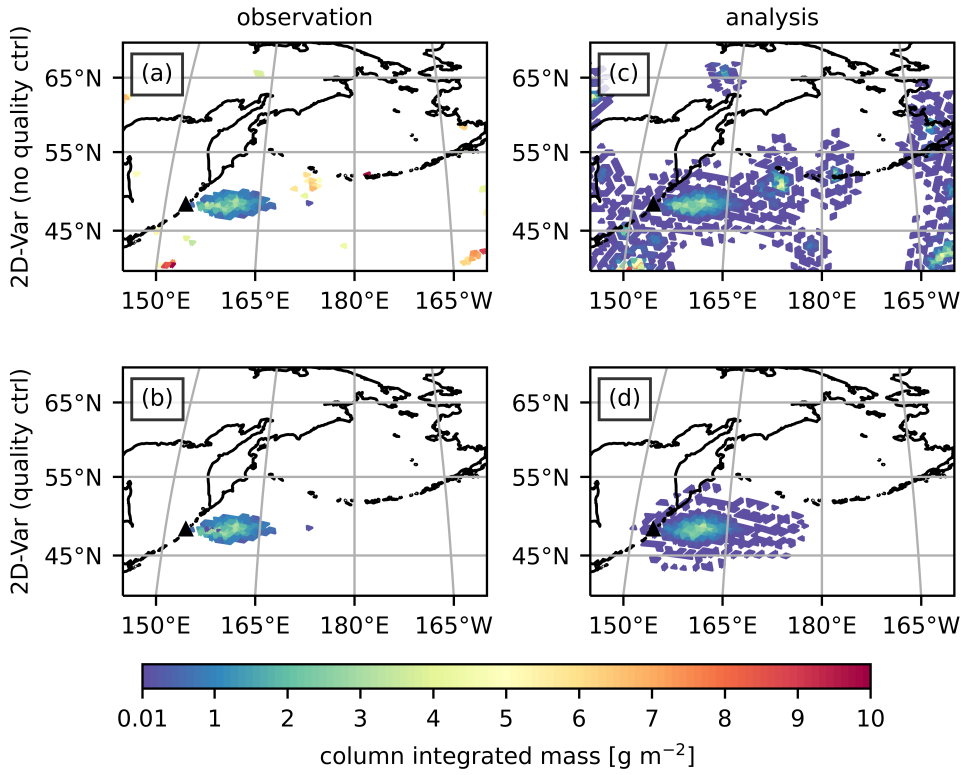

Figure 7.3: Observed column integrated ash mass Γ_{ash} on model grid (a) without and (b) with quality control. Panels (c) and (d) show the resulting analysis field. The black triangle marks the location of the Raikoke volcano.

The remapped and averaged AHI data with quality control is shown in Fig. 7.3 (b). Most of the scattered data points outside the volcanic cloud are now removed, whereas most of the data points within the volcanic clouds fulfill the quality criterion. Figure 7.3 (d) displays the resulting analysis state. This analysis state of the 2D-Var assimilation with quality control looks more alike the one of the ART En-Var assimilation in Fig. 7.2 (d).

The comparison between the ART En-Var and 2D-Var assimilation illustrates one benefit of considering information provided by an ensemble. For the presented assimilation, no quality control measure is necessary for the assimilation with En-Var. The difference between the two methods lies in the model error covariance $\mathbf{B}$. For ART En-Var, due to the ensemble information, the model uncertainty is constrained to areas in which at least one of the ensemble members contains volcanic ash. A hypothetical grid cell with index i that contains the same ash concentration in all ensemble members would result in a covariance $B_{ij} = \left(\mathbf{C} \circ \mathbf{X}\mathbf{X}^{\mathrm{T}}\right)_{ij} = 0$. In contrast, the covariance is largest where the ensemble members differ the most. Grid cells within the volcanic cloud are expected to vary considerably among the different ensemble members. For the 2D-Var method, however, the covariance is the same in every grid cell. This relation between covariance, location, and assimilation method is examined in more detail in the following.

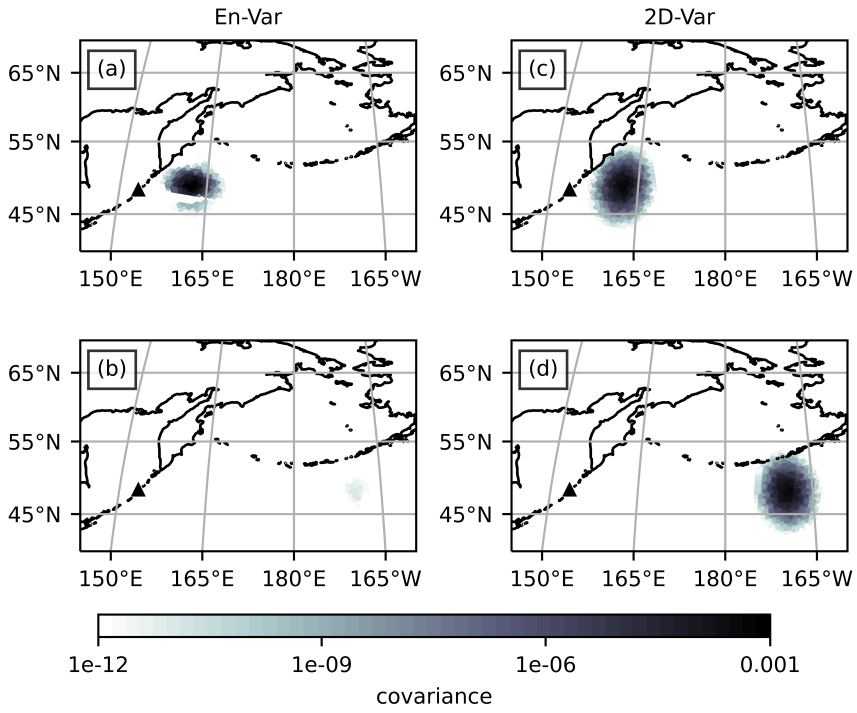

Figure 7.4: Covariance of two grid points for ART En-Var (left) and 2D-Var (right). The top shows the covariance for the grid cell at 162.3° E 48.8° N, the bottom for 169.3° W 48.1° N. The black triangle marks the location of the Raikoke volcano.

The covariance is displayed in Fig. 7.4 exemplarily for two different grid cells i. Panels on the left and right represent the covariance $\mathbf{B} = \mathbf{C} \circ \mathbf{X}\mathbf{X}^{\mathrm{T}}$ of the ART En-Var method and $\mathbf{B} = \mathbf{C}$ of the 2D-Var method, respectively. The top row displays the covariance for the grid cell at 162.3° E and 48.8° N. This grid cell lies within the volcanic cloud, e.g., displayed by the ensemble mean in Fig. 7.2 (c). The bottom row contains the values for the grid cell at 169.3° W and 48.1° N, which lies outside the volcanic cloud.

Fig. 7.4 illustrates what has already been mentioned in the paragraph on quality control of observational data above. The covariance of the 2D-Var method contains no information of the volcanic cloud. Hence, it looks the same at different locations, as shown in Fig. 7.4 (c) and (d). The opposite is true for the ART En-Var assimilation. Outside the volcanic cloud, values of the covariance are close to zero, Fig. 7.4 (b). Inside the volcanic cloud, however, values are significantly higher.

The covariance can be interpreted as a quantity that indicates how $\mathbf{y} - H\mathbf{x_b}$ in grid cell i influences neighboring cells. Higher values depict a stronger influence. The highest value is reached in cell i itself. The circular shape results from the Gaussian error function. Deviations from a symmetrically distribution in the left panels are due to the ensemble matrix. For example, the shape of the covariance in Fig. 7.4 (a) adumbrates the location and shape of the volcanic ash cloud.

In the following, only the analysis state of the ART En-Var method is used.

7.3. Influence of ART En-Var on Ash Forecast

Figure 7.5 (a) shows the daily mean column integrated mass $\overline{\Gamma}_{ash}$ retrieved from AHI measurements on 23 June 2019. The same quantity is displayed in panels (b) and (c) for the ctrl simulation and the En-Var experiment, respectively. The two bottom panels, (d) and (e), display

$$\left|\overline{\Gamma}_{ash,\text{AHI}} - \overline{\Gamma}_{ash,\text{ctrl}}\right| - \left|\overline{\Gamma}_{ash,\text{AHI}} - \overline{\Gamma}_{ash,\text{En-Var}}\right| .$$

Red colors represent data points at which the En-Var experiment is closer to the observation than the ctrl simulation, and blue colors vice versa. The difference between panel (d) and (e) is a mask that is applied to data points in (e). Figure 7.5 (e) shows only data points at which the AHI retrieval contains an column integrated ash mass $\overline{\Gamma}_{ash,\text{AHI}} > 0.01$ g m^2.

The differences between the three panels (a), (b), and (c) are rather large. On the one hand, absolute values of column integrated mass in the AHI measurement are significantly higher than in the two ICON-ART simulations. On the other hand, the expansion of the measured volcanic cloud in (a) is much smaller than the one in the simulations. The ctrl simulation and the En-Var experiment also differ. The former contains higher column integrated mass values east of 165° E than the En-Var experiment. However, additional volcanic ash appears in the region around the volcano in the En-Var experiment. Apparently, part of the volcanic cloud is transported in a different direction in the En-Var experiment compared to the ctrl simulation. One reason could be that the assimilation changes the ash concentration in the wrong altitude. Another explanation could be a horizontal shift of the ash cloud due to the assimilation.

The difference plots in Fig. 7.5 (d) and (e) allow a point to point comparison between the two simulations and the measurement. In panel (d), red and blue shades balance each other. That means, there are red regions where the En-Var experiment is closer to the observed column integrated ash mass and blue areas where the ctrl simulation is closer to the observation. When looking at only these data points at which the AHI instrument measured the volcanic cloud, the blue color prevails. Apparently, the ART En-Var assimilation leads to a reduction of ash concentration in this region.

At first glance, the result of the En-Var experiment seems to be worse than the ctrl simulation. To gain a more objective insight, I apply the FSS and SAL metric.

The SAL method is applied with a threshold to identify objects of $R^* = 0.01$ g m^{-2}. Table 7.2 presents the SAL values for the ctrl simulation and the En-Var experiment. As a reminder, a value of 0 indicates

Table 7.2: Comparison of daily mean column integrated mass of volcanic ash between AHI and the data assimilation experiment on 23 June 2019 using the SAL method.

Experiment	S	A	L
ctrl	1.240	−0.839	0.025
En-Var	0.971	−0.973	0.059

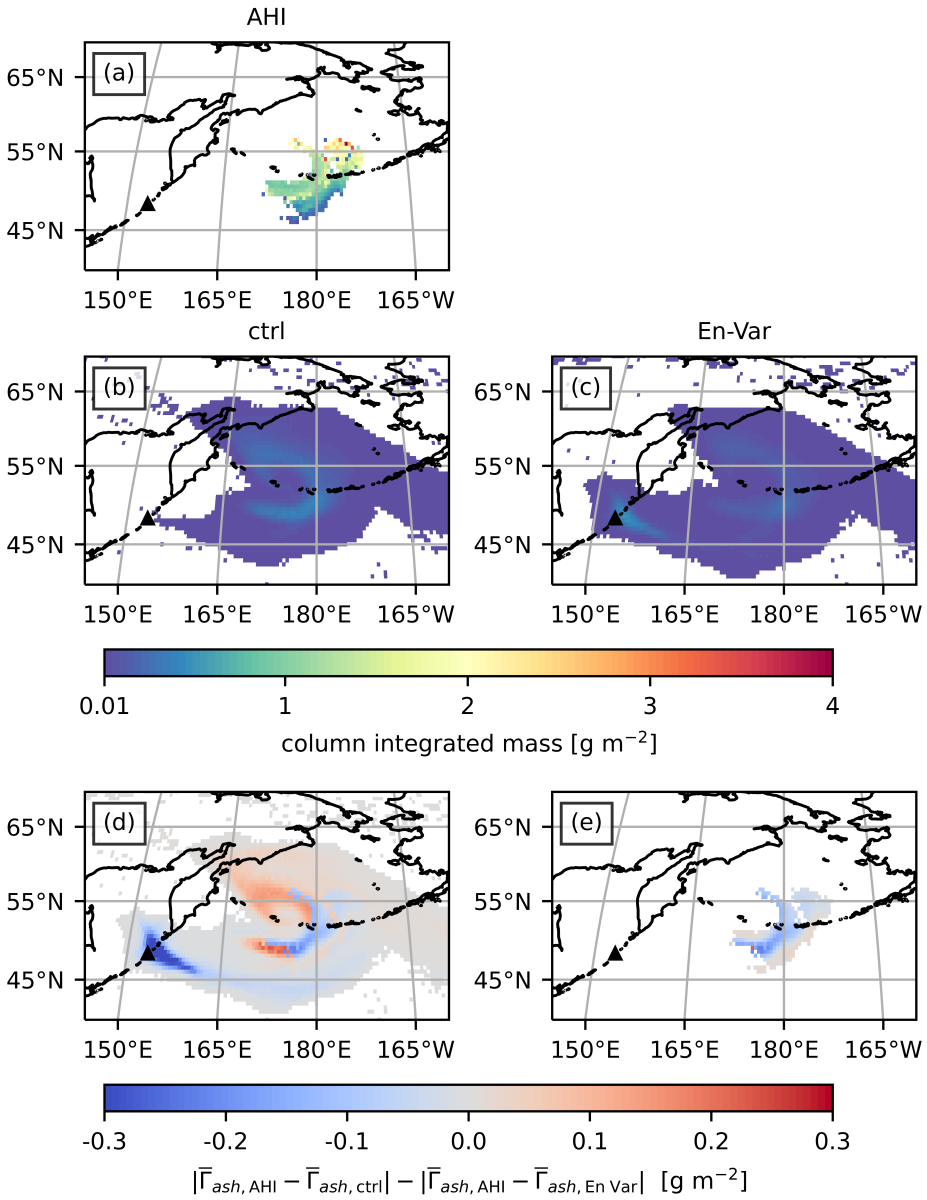

Figure 7.5: Daily mean column integrated mass $\overline{\Gamma}_{ash}$ of volcanic ash on 23 June 2019. (a) contains $\overline{\Gamma}_{ash,\mathrm{AHI}}$ of the AHI measurement, (b) contains $\overline{\Gamma}_{ash,\mathrm{ctrl}}$ of the ctrl simulation, and (c) $\overline{\Gamma}_{ash,\mathrm{En\text{-}Var}}$ of the En-Var experiment. (d,e) display $\left|\overline{\Gamma}_{ash,\mathrm{AHI}} - \overline{\Gamma}_{ash,\mathrm{ctrl}}\right| - \left|\overline{\Gamma}_{ash,\mathrm{AHI}} - \overline{\Gamma}_{ash,\mathrm{En\text{-}Var}}\right|$. Red and blue colors represent an improvement and a decline in the data assimilation experiment, respectively. The difference between (d) and (e) is the ash mask $\overline{\Gamma}_{ash,\mathrm{AHI}} > 0.01\ \mathrm{g\,m^2}$ which is applied in (e). The black triangle marks the location of the Raikoke volcano.

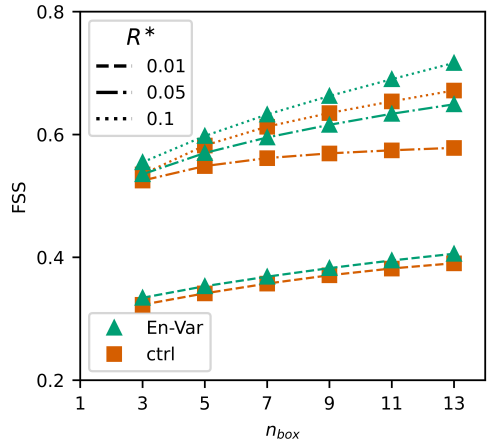

Figure 7.6: Comparison of daily mean column integrated mass of volcanic ash between AHI and the data assimilation experiment on 23 June 2019 using the FSS metric. Each marker represents one FSS value at a evaluation box size n_{box}, a threshold value R^*, and experiment. The colors distinguish between the En-Var experiment (green) and the ctrl simulation (orange). The connecting lines discriminate the different threshold values R^*.

a perfect agreement between model and observation. The location value L is close to zero in both, the ctrl simulation and the En-Var experiment. However, the L value slightly deteriorated in the En-Var experiment compared to the ctrl simulation. The negative amplitude value A indicates that in both, ctrl and En-Var experiment, the ash mass is lower in the simulation compared to the observation. The daily mean column integrated mass in the En-Var experiment also exhibits a worse A value than in the ctrl simulation. In contrast, the structure value S is better in the En-Var experiment than in the ctrl simulation. Figure 7.6 visualizes the result of the FSS analysis. The FSS has been determined for both, En-Var experiment and ctrl simulation. The model results are compared to the daily mean column integrated mass of volcanic ash measured by the AHI on 23 June 2019. I apply the FSS metric with different evaluation box sizes n_{box} and threshold values R^*. The value n_{box} indicates a box size of $n_{box} \times n_{box}$ cells around one grid cell in which fraction values are determined (compare Sect. 5.3.1). The threshold value R^* is needed to determine the necessary binary field for the evaluation. In Fig. 7.6, the different line styles discriminate between the different threshold values R^*. The color coding together with the marker style distinguish between the En-Var experiment and the ctrl simulation. As a reminder, a FSS $= 1$ represents a perfect agreement between observation and model result.

The markers in Fig. 7.6 show that for one value of R^* the FSS is higher for the En-Var experiment than for the ctrl simulation. This is true regardless of the evaluation box size n_{box}. Hence, the daily mean column integrated volcanic ash mass in the En-Var experiment is closer to the AHI observation, according to the FSS metric. The ART En-Var assimilation improves the FSS up to 12%.

On the one hand, the point to point comparison of daily mean column integrated ash mass in Fig. 7.5 did not show an improvement in the simulated column integrated ash mass after the assimilation. On the

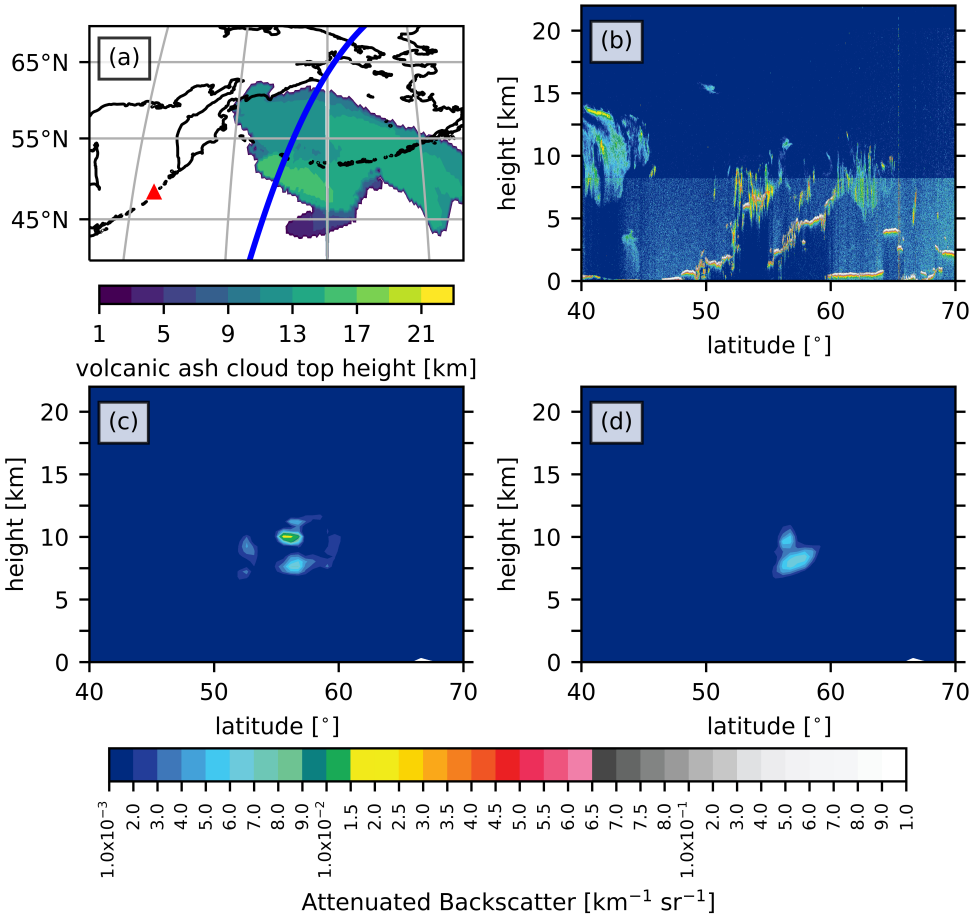

Figure 7.7: (a) CALIPSO ground track on 23 June 2019, around 15:00 UTC in blue color and location of Raikoke volcano as red triangle. The contour map shows the volcanic ash cloud top height in the ctrl simulation. (b) The CALIOP attenuated backscatter at 532 nm for the satellite position between 40° N and 70° N. (c,f) Total attenuated backscatter at 532 nm of volcanic aerosols under the CALIPSO ground track on 23 June 2019, for the 15:00 UTC model output are displayed. (c) shows the result of the ctrl simulation and (d) of the En-Var experiment.

other hand, the FSS and SAL metric indicate at least some improvements. I would like to conclude this section with four remarks on the data assimilation experiment.

First, the horizontal resolution in the ICON-ART simulations of the data assimilation experiment is at $\approx$ 40 km. This resolution is significantly coarser compared to the 13 km used for the simulations in Sect. 7. The horizontal resolution in the data assimilation experiment was limited due to technical reasons. As the newly developed assimilation code is not yet parallelized, it has to run on a single processor. Consequently, the memory is a limiting factor. The coarse resolution, however, strongly influences the volcanic aerosol dispersion in the model. Figure 7.7 (b) shows the total attenuated backscatter at 532 nm measured by the CALIOP instrument on 23 June 2019, around 15:00 UTC. It contains this prominent feature between 49° N and 51° N at a height of around 16 km which has been identified as volcanic aerosol earlier in Sect. 6.3. This feature is visible neither in the ctrl simulation, Fig. 7.7 (c), nor in the data assimilation experiment, Fig. 7.7 (d). This comparison shows that the coarse resolution is not suffi-

cient to reproduce the vertical distribution of volcanic aerosol as it was in the finer resolution shown in Sect. 6.

Second, the quality of the observational data also plays an important role in the evaluation of the data assimilation experiment. The AHI retrieval was chosen, as the instrument is onboard the geostationary Himawari-8 satellite. On the one hand, a geostationary instrument can be beneficial for the assimilation of volcanic aerosol (Plu et al., 2021), as it allows a high spatial and temporal resolution of observations. On the other hand, the AHI instrument has difficulties to detect volcanic ash when it is obscured by water clouds or the ash concentration is low. During and after the Raikoke eruption there were many water clouds over the north Pacific. The patchy AHI retrievals on 23 June 2019 suggest that the instrument did miss some parts of the volcanic ash cloud. Furthermore, I don't have the information of measurements containing zero ash. Both, the patchy retrieval and the missing information on zero ash, increase the uncertainty of the objective evaluation of the data assimilation experiment.

Third, in the scope of this thesis the assimilation setup is constricted to two dimensions. This means, the vertical distribution of volcanic ash is assumed to be correct in the first guess. Hence, during the assimilation, this vertical distribution is not changed. Adjusting the ash concentration in the wrong altitude during the assimilation, could be an explanation for the increased column integrated ash mass around the Raikoke volcano in Fig. 7.5 (c). Future studies, which build on the present thesis, should include some kind of height information. This could be either from remote sensing data or from an ensemble.

Fourth, neither information about the volcanic ash size distribution nor about the mixing state is incorporated into the assimilation in this thesis. This means, the increment that is added to the ash concentration in one model grid cell is distributed among the different ash modes weighted to their concentration in the first guess. This can have a large effect on the forecasted ash concentration. For example, during the assimilation the column integrated ash mass is increased in one model column. The increment is then mainly assigned to the giant mode of ash particles, as these are the prevailing particles in this model column of the first guess. However, the analysis in Sect. 6.3 (compare Fig. 6.7) showed that the giant mode was removed quite rapidly after the volcanic eruption. The opposite is true for accumulation mode ash particles. Consequently, the ash concentration 24 h after the assimilation depends strongly on the assumption of the particle size distribution at time of the assimilation. Incorporating information on the particle size distribution from observations in the assimilation of volcanic aerosol remains an issue for future studies.

The above stated shows that it is difficult to draw a final conclusion on the potential of the ART En-Var method on the volcanic aerosol dispersion forecast. On the one hand, both the qualitative and the point to point evaluation suggest that the En-Var experiment exhibits worse results compared to the ctrl experiment. On the other hand, the SAL and FSS metric indicate some improvements in the forecast of volcanic aerosol dispersion initialized with the ART En-Var assimilation. Before a final conclusion can be drawn, the remaining open issues in the ART En-Var method need to be addressed in future

work. These open issues are the missing information during assimilation of the vertical volcanic aerosol distribution, the aerosol size distribution, and the aerosol mixing state, as presented above. Furthermore, the AHI measurements on 23 June, which are used for validation, have some deficiencies and do not seem to measure the whole volcanic ash cloud. Therefore, additional observational data could be beneficial. A major issue that limits the interpretation of the ctrl and En-Var experiment is the horizontal resolution of ≈ 40 km in the model simulations. At this coarse horizontal resolution, ICON-ART fails to reproduce the vertical distribution of volcanic aerosol. This is contrary to the simulations with finer resolution shown in Sect. 6.

8. Conclusions

The aim of this thesis was the improvement of volcanic aerosol dispersion forecast. Approaches achieving this were twofold. One approach focused on microphysical processes which are neglected in operational volcanic ash dispersion forecasts today. In this context, my particular interest was on aerosol dynamic processes and aerosol–radiation interaction. Both are now integrated in ICON-ART. The second approach was the implementation of an En-Var data assimilation method for volcanic ash. This development was made within the data assimilation framework of DWD.
I tested all extensions and new developments for the case of the Raikoke eruption of June 2019. This recent eruption was one of the largest volcanic eruptions during the last 30 years. Volcanic ash and SO_2 were emitted with an eruption column reaching up to 14 km. The eruption and its aftermath were extensively covered by satellite observations. These measurements were used to validate the new developments qualitatively and quantitatively.
The effect of aerosol dynamic processes and aerosol–radiation interaction on volcanic aerosol dispersion was studied with global ICON-ART simulations on a 13 km grid. A set of seven simulation scenarios gave detailed insights into the contribution of secondary aerosol formation, condensation, coagulation, and aerosol–radiation interaction on the atmospheric transport of volcanic aerosols. The results give an answer to the research questions 1. – 4., posed in Sect. 1:

1. How do aerosol dynamic processes influence the volcanic aerosol dispersion?

   Condensation and coagulation generate internally mixed particles. These mixed particles generally have larger diameters which, therefore, sediment faster. Consequently, aerosol dynamic processes act as a sink for volcanic aerosols. This also influences the vertical distribution, more specifically the downward mixing, of volcanic aerosols. My results suggest that the sedimentation of large particles is responsible for the removal of about 50% of volcanic ash over the first 12 h after the end of the eruption. Aerosol dynamic processes do play an important role in this respect, as in simulations without these processes only about 20% of volcanic ash are removed during the same time period.

2. Which of the aerosol dynamic processes is most relevant and has the largest effect on aerosol dispersion?

   The coagulation of particles in the dense volcanic aerosol cloud in combination with the nucleation of secondary volcanic aerosols (sulfate) is the main driver for the fast removal of volcanic aerosols

during the first 12 h after the end of the Raikoke eruption. In my setup, mainly the mass of coarse mode particles is reduced due to the enhanced sedimentation, whereas mixed accumulation particles mostly remain airborne during the first four days after the eruption. My results suggest that the coagulation between coarse mode ash particles and secondary volcanic aerosols forms internally mixed particles that sediment significantly faster than insoluble coarse mode ash.

3. What is the influence of the interaction between radiation and volcanic aerosols on their transport?

   The interaction of short and long wave radiation with volcanic aerosols already has a strong impact on the aerosol dispersion during the first days after the eruption. Only in simulations that consider this interaction the volcanic aerosol cloud is lifted into altitudes that are measured by multiple satellites. My results suggest that after the Raikoke eruption the volcanic aerosol cloud top rises about 3 km during the first 12 h and reaches a height of around 20 km after four days.

4. Is the combined representation of aerosol dynamic processes and aerosol–radiation interaction beneficial for volcanic aerosol dispersion forecast?

   The comparison of model results with satellite retrievals, especially with CALIOP and AHI, suggests that the combination of aerosol dynamic processes and aerosol–radiation interaction is crucial for a correct volcanic aerosol dispersion forecast. Both processes affect the vertical distribution of aerosols. Consequently, these processes influence in which altitudes the aerosols are transported. This is particularly important during the first days after the eruption and, therefore, for forecasts with leadtimes of few days.

The lifting of aerosol clouds due to the absorption of short and longwave radiation has been described before, however, only for external mixtures of aerosol. In this thesis the lifting is described for internally mixed particles. Nevertheless, I expected a lifting of internally mixed particles beforehand. Similarly, the increased sedimentation due to aerosol aging could be expected to some extent. It is the logical consequence of an increased particle size.

Surprisingly, both effects have only a minor influence on the horizontal distribution of volcanic aerosols during the first four days after the Raikoke eruption 2019. Some differences are visible in the SAL values for different simulation scenarios. Qualitatively, however, simulated column integrated ash masses look similar regardless of the considered processes. A main reason for this behavior can be the short simulated time period. For example, de Leeuw et al. (2021) show that the vertical distribution of SO_2 indeed becomes very important for simulation periods of 2 – 3 weeks.

Also surprising was the fact that the condensation of gaseous species on particles plays only a minor role during the first four days after the Raikoke eruption 2019. During this time period the aerosol dynamic processes were dominated by secondary aerosol formation and coagulation.

The potential of the developed ART En-Var data assimilation method for volcanic aerosol dispersion forecast was investigated with the help of two global ICON-ART simulations on a 40 km grid. A ctrl

simulation was conducted without data assimilation. The other simulation was initialized from the result of the ART En-Var assimilation. The results of both simulations one day after the initialization were compared with AHI measurements. This comparison gives an answer to the remaining research question, posed in Sect. 1:

5. What is the potential of an En-Var method for the assimilation of column integrated ash mass?

   Using an ensemble based data assimilation method is very useful, as the ensemble information constrains the model uncertainty to areas in which at least one of the ensemble members contains volcanic ash. Thereby, some level of quality control for spurious signals in observational data is inherent in the En-Var method. A day after the assimilation the influence of the data assimilation remains visible. The FSS and the SAL metric suggest some improvements in the forecast initialized from the assimilation.

In the scope of this thesis the optical properties were derived offline for spherical particles in a predefined mixing state. Building on my work, future studies can incorporate the temporal changes of the mixing state as well as the non-spherical shape of chemically aged ash particles.
In terms of data assimilation, three developments would be of particular interest for advancing the En-Var method implemented in the scope of this thesis. First, bringing the current 2D approach to full 3D enables the incorporation of information on the vertical distribution of the volcanic cloud. This information can come either from observational data or from the ensemble members. Second, as information on the particle size distribution and the mixing state is not accounted for in the current data assimilation method, incorporating this information from observational data remains an open issue for future studies. Third, the assimilation code should be advanced in a way that it can be run on a parallel computing system. This would allow data assimilation experiments in a higher spatial resolution.

A. Optical Properties of Aerosol Modes

Table A.1: Mass specific extinction coefficient k_e and mass specific backscattering coefficient k_b at $\lambda = 532$ nm for selected volcanic aerosols.

	s_ait	s_acc	i_acc	m_acc	i_coa	m_coa
k_e [$m^2\,kg^{-1}$]	2.48959	1.31627	0.97248	1.33489	0.13881	0.19838
k_b [$m^2\,kg^{-1}$]	0.21806	0.10777	0.09244	0.12636	0.00695	0.01039

Table A.2: Mass specific extinction coefficient k_e for RRTM longwave wavebands in $m^2\,g^{-1}$.

wavenumber [cm^{-1}]								
low	high	s_ait	s_acc	i_acc	m_acc	i_coa	m_coa	giant
10.	350.	0.02871	0.02872	0.05259	0.04731	0.13660	0.13980	0.09196
350.	500.	0.01809	0.01815	0.10150	0.08720	0.15261	0.18195	0.08886
500.	630.	0.06639	0.06673	0.19431	0.18097	0.13696	0.17791	0.08055
630.	700.	0.06385	0.06418	0.10277	0.08664	0.14750	0.17467	0.08660
700.	820.	0.04190	0.04228	0.11910	0.07276	0.17679	0.24752	0.08265
820.	980.	0.10976	0.11113	0.51961	0.41004	0.16921	0.27436	0.08085
980.	1080.	0.20250	0.20611	0.54460	0.50196	0.16103	0.25671	0.07844
1080.	1180.	0.39568	0.40169	0.32293	0.34081	0.13106	0.18340	0.07462
1180.	1390.	0.40459	0.40688	0.09055	0.06058	0.15017	0.17857	0.08577
1390.	1480.	0.13125	0.13265	0.09215	0.05038	0.16522	0.20659	0.08552
1480.	1800.	0.13642	0.13971	0.16407	0.05903	0.18030	0.27097	0.07874
1800.	2080.	0.19499	0.20027	0.23015	0.05723	0.18447	0.30053	0.07773
2080.	2250.	0.19894	0.20658	0.29160	0.06806	0.18296	0.31043	0.07711
2250.	2380.	0.21817	0.22810	0.32684	0.07189	0.18324	0.31451	0.07705
2380.	2600.	0.23121	0.24350	0.41156	0.08792	0.18130	0.32047	0.07636
2600.	3250.	0.30845	0.32553	0.65373	0.21365	0.17188	0.31410	0.07445

Table A.3: Mass specific extinction coefficient k_e for RRTM shortwave wavebands in $m^2\,g^{-1}$.

wavenumber [cm^{-1}]								
low	high	s_ait	s_acc	i_acc	m_acc	i_coa	m_coa	giant
2600.	3250.	0.30845	0.32553	0.65373	0.21365	0.17188	0.31410	0.07445
3250.	4000.	0.10585	0.11875	0.76660	0.11732	0.17242	0.30629	0.07504
4000.	4650.	0.00833	0.03493	0.97555	0.17783	0.16678	0.31355	0.07422
4650.	5150.	0.00529	0.05899	1.18041	0.26975	0.16826	0.30923	0.07310
5150.	6150.	0.00373	0.08270	1.40476	0.42464	0.16364	0.29940	0.07338
6150.	7700.	0.00538	0.20152	1.61062	0.70725	0.16259	0.28861	0.07252
7700.	8050.	0.01560	0.45240	1.67312	0.85086	0.16075	0.29394	0.07114
8050.	12850.	0.02586	0.70334	1.79298	1.93800	0.15459	0.28390	0.07081
12850.	16000.	0.09897	1.77808	1.67589	3.09623	0.15298	0.27662	0.06996
16000.	22650.	0.24575	3.06857	1.60644	4.70122	0.15129	0.26733	0.06923
22650.	29000.	0.60659	5.00644	1.49926	6.01615	0.14943	0.26428	0.06934
29000.	38000.	1.43449	7.36070	1.44206	7.48345	0.14866	0.25868	0.06860
38000.	50000.	4.08078	10.25832	1.43603	7.89588	0.14726	0.25618	0.06856
820.	2600.	0.22117	0.22676	0.41156	0.08792	0.18130	0.32047	0.07636

Table A.4: Single scattering albedo ω for RRTM longwave wavebands.

wavenumber [cm^{-1}]								
low	high	s_ait	s_acc	i_acc	m_acc	i_coa	m_coa	giant
10.	350.	0.00000	0.00015	0.04006	0.00121	0.47743	0.44070	0.47706
350.	500.	0.00002	0.00148	0.06169	0.00219	0.45472	0.41573	0.47017
500.	630.	0.00002	0.00144	0.03602	0.00147	0.36681	0.29348	0.45239
630.	700.	0.00001	0.00095	0.08923	0.00370	0.52128	0.48220	0.51921
700.	820.	0.00004	0.00279	0.27222	0.01553	0.56743	0.59125	0.49079
820.	980.	0.00005	0.00313	0.14415	0.01049	0.41511	0.37717	0.47412
980.	1080.	0.00006	0.00393	0.10740	0.00741	0.40189	0.35010	0.46897
1080.	1180.	0.00004	0.00245	0.05327	0.00334	0.36723	0.28690	0.46946
1180.	1390.	0.00002	0.00137	0.27489	0.02217	0.66563	0.65709	0.60722
1390.	1480.	0.00004	0.00261	0.39957	0.03974	0.71916	0.73068	0.62725
1480.	1800.	0.00013	0.00775	0.61227	0.10533	0.73765	0.78002	0.61125
1800.	2080.	0.00014	0.00864	0.74961	0.20916	0.76397	0.81763	0.63904
2080.	2250.	0.00023	0.01348	0.77353	0.25186	0.75205	0.80947	0.62906
2250.	2380.	0.00029	0.01665	0.79408	0.28820	0.75175	0.81319	0.63021
2380.	2600.	0.00036	0.02028	0.81133	0.34065	0.73536	0.80185	0.61772
2600.	3250.	0.00040	0.02121	0.70444	0.26309	0.60566	0.67223	0.53426

Table A.5: Single scattering albedo ω for RRTM shortwave wavebands.

wavenumber [cm^{-1}]								
low	high	s_ait	s_acc	i_acc	m_acc	i_coa	m_coa	giant
2600.	3250.	0.00040	0.02121	0.70444	0.26309	0.60566	0.67223	0.53426
3250.	4000.	0.00741	0.22991	0.98066	0.92185	0.91288	0.94769	0.83957
4000.	4650.	0.06974	0.74581	0.98649	0.95695	0.92251	0.95384	0.85418
4650.	5150.	0.20538	0.92057	0.98804	0.96946	0.92039	0.95300	0.84836
5150.	6150.	0.45469	0.97199	0.99049	0.98170	0.92658	0.95510	0.85832
6150.	7700.	0.92180	0.99749	0.99121	0.98774	0.92277	0.95282	0.85347
7700.	8050.	0.96070	0.99870	0.99125	0.98920	0.92170	0.95254	0.85058
8050.	12850.	0.99968	0.99999	0.99064	0.99394	0.91454	0.94829	0.84459
12850.	16000.	1.00000	1.00000	0.98988	0.99572	0.91610	0.94652	0.84246
16000.	22650.	1.00000	1.00000	0.98669	0.99619	0.90148	0.93797	0.81888
22650.	29000.	1.00000	1.00000	0.98156	0.99572	0.87338	0.91810	0.77834
29000.	38000.	1.00000	1.00000	0.96690	0.99380	0.81503	0.87297	0.69958
38000.	50000.	1.00000	1.00000	0.96146	0.99278	0.79107	0.85401	0.67458
820.	2600.	0.00014	0.00849	0.81133	0.34065	0.73536	0.80185	0.61772

Table A.6: Asymmetry parameter g for RRTM longwave wavebands.

wavenumber [cm^{-1}]								
low	high	s_ait	s_acc	i_acc	m_acc	i_coa	m_coa	giant
10.	350.	1.00000	0.00056	0.07560	0.02033	0.53160	0.43815	0.69978
350.	500.	1.00000	0.00313	0.11793	0.03435	0.64872	0.54352	0.80666
500.	630.	1.00000	0.00564	0.13537	0.03976	0.74838	0.63807	0.86242
630.	700.	1.00000	0.00706	0.17575	0.05253	0.75548	0.67138	0.85759
700.	820.	0.00014	0.00970	0.23553	0.07783	0.69469	0.61619	0.85526
820.	980.	0.00089	0.01440	0.17171	0.05806	0.78330	0.64937	0.89361
980.	1080.	0.00117	0.01905	0.19280	0.06094	0.81618	0.70029	0.90978
1080.	1180.	0.00115	0.01783	0.28594	0.08656	0.86939	0.81249	0.90971
1180.	1390.	0.00125	0.01880	0.39678	0.13482	0.88900	0.84838	0.92811
1390.	1480.	0.00170	0.02563	0.41799	0.14586	0.87300	0.83660	0.91188
1480.	1800.	0.00228	0.03447	0.48750	0.18695	0.84893	0.81791	0.90146
1800.	2080.	0.00317	0.04591	0.53270	0.22016	0.82494	0.79809	0.88755
2080.	2250.	0.00400	0.05672	0.55838	0.24072	0.82388	0.79584	0.89420
2250.	2380.	0.00463	0.06442	0.57102	0.25214	0.82031	0.79269	0.89407
2380.	2600.	0.00529	0.07217	0.59803	0.27669	0.82378	0.79380	0.90232
2600.	3250.	0.00702	0.08948	0.65298	0.32117	0.88148	0.84011	0.94428

Table A.7: Asymmetry parameter g for RRTM shortwave wavebands.

wavenumber [cm^{-1}]								
low	high	s_ait	s_acc	i_acc	m_acc	i_coa	m_coa	giant
2600.	3250.	0.00702	0.08948	0.65298	0.32117	0.88148	0.84011	0.94428
3250.	4000.	0.01005	0.12143	0.66194	0.37086	0.73400	0.71778	0.81511
4000.	4650.	0.01492	0.16762	0.67549	0.40449	0.73960	0.70060	0.81220
4650.	5150.	0.02098	0.21427	0.69161	0.44083	0.74079	0.71839	0.81600
5150.	6150.	0.02577	0.24542	0.70039	0.48075	0.75837	0.71416	0.82369
6150.	7700.	0.04151	0.32461	0.70707	0.52533	0.76940	0.73644	0.82932
7700.	8050.	0.06290	0.39060	0.71120	0.54137	0.77663	0.73492	0.83346
8050.	12850.	0.08424	0.45659	0.69139	0.60919	0.79756	0.74936	0.84748
12850.	16000.	0.14913	0.56569	0.69478	0.64623	0.81412	0.77653	0.85078
16000.	22650.	0.21072	0.62403	0.68957	0.66742	0.81912	0.80033	0.85824
22650.	29000.	0.28762	0.66664	0.71290	0.68337	0.83439	0.80926	0.87292
29000.	38000.	0.36437	0.68228	0.73915	0.69213	0.85476	0.82814	0.89689
38000.	50000.	0.46741	0.68491	0.75347	0.68718	0.86322	0.83712	0.90543
820.	2600.	0.00272	0.03920	0.59803	0.27669	0.82378	0.79380	0.90232

B. Total Attenuated Backscatter at 532 nm

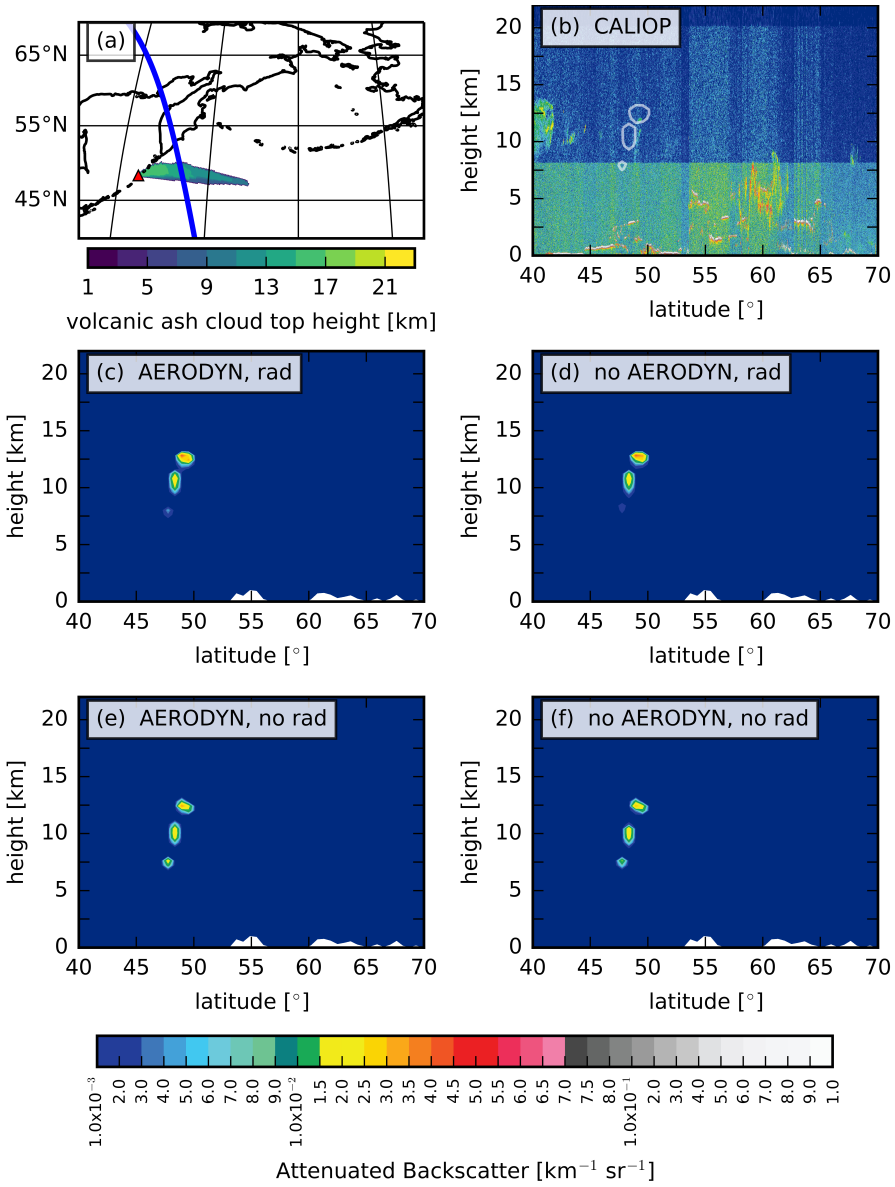

Figure B.1: (a) CALIPSO ground track on 22 June 2019, around 03:00 UTC in blue color and location of Raikoke volcano as red triangle. The contour map shows the volcanic ash cloud top height for the AERODYN-rad scenario. (b) The CALIOP attenuated backscatter for 532 nm for the satellite position between 40° N and 70° N is displayed in the top right panel. The white line shows the 0.002 km^{-1} sr^{-1} contour of AERODYN-rad at 03:00 UTC. (c – f) Total attenuated backscatter for 532 nm of volcanic aerosols under the CALIPSO ground track on 22 June 2019, for the 03:00 UTC model output are displayed. (c) shows the result for AERODYN-rad, (d) for no_AERODYN-rad, (e) for AERODYN-no_rad, and (f) for no_AERODYN-no_rad, respectively. (Muser et al., 2020)

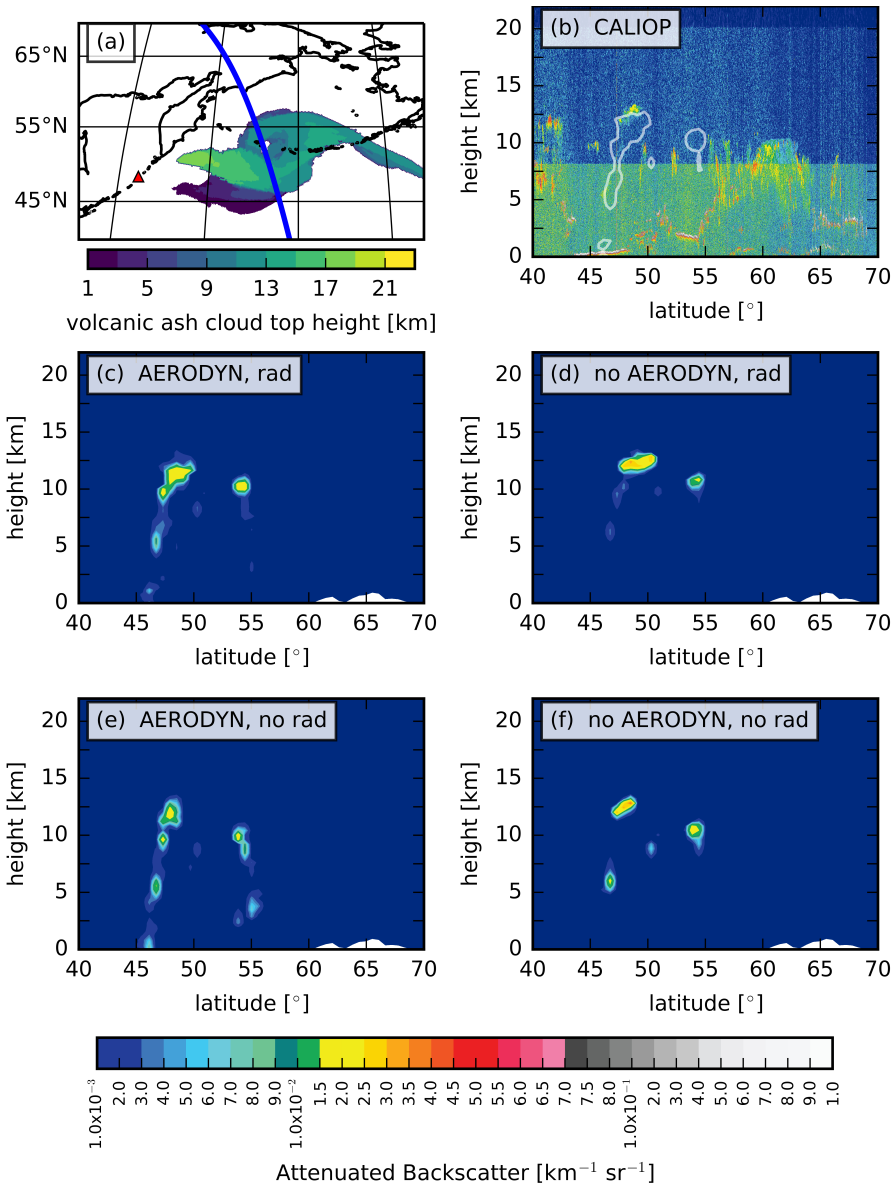

Figure B.2: Same as Fig. B.1 on 23 June 2019, 02:00 UTC.

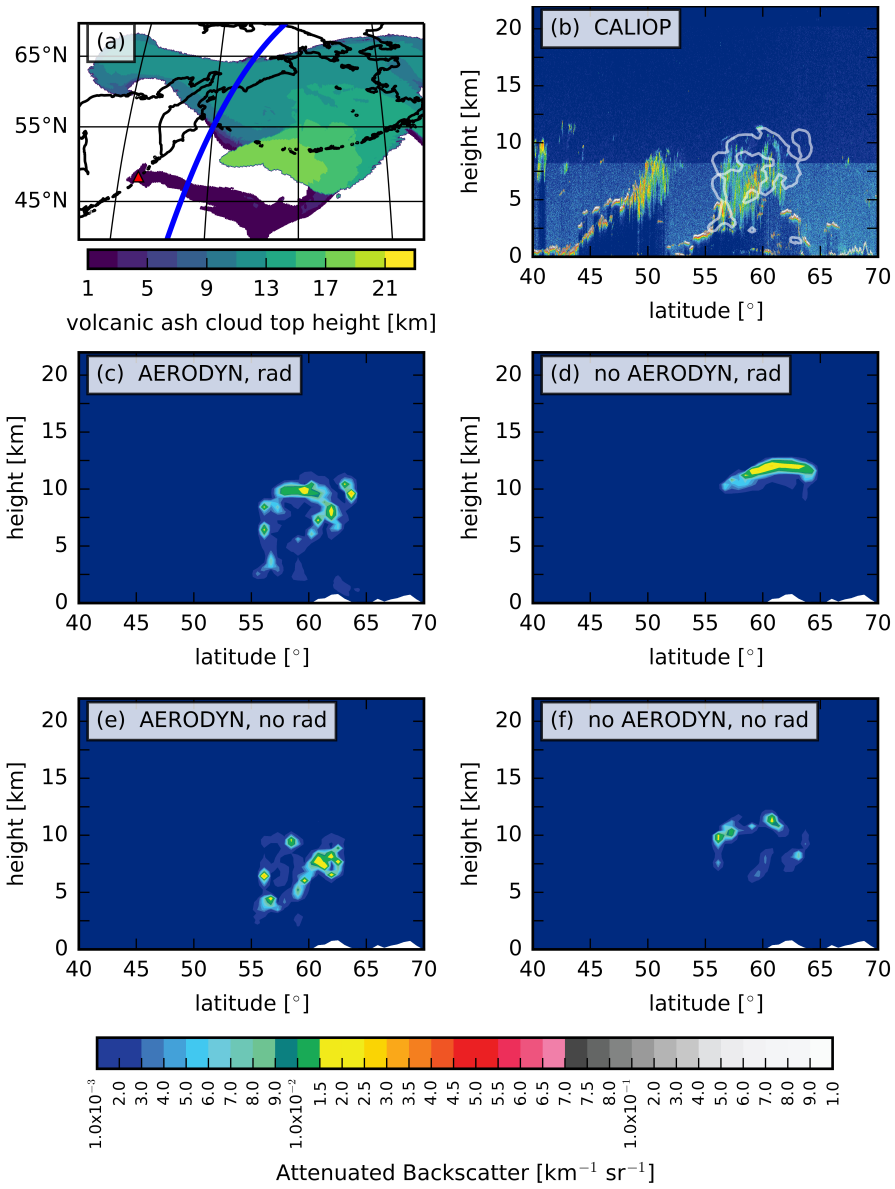

Figure B.3: Same as Fig. B.1 on 24 June 2019, 16:00 UTC.

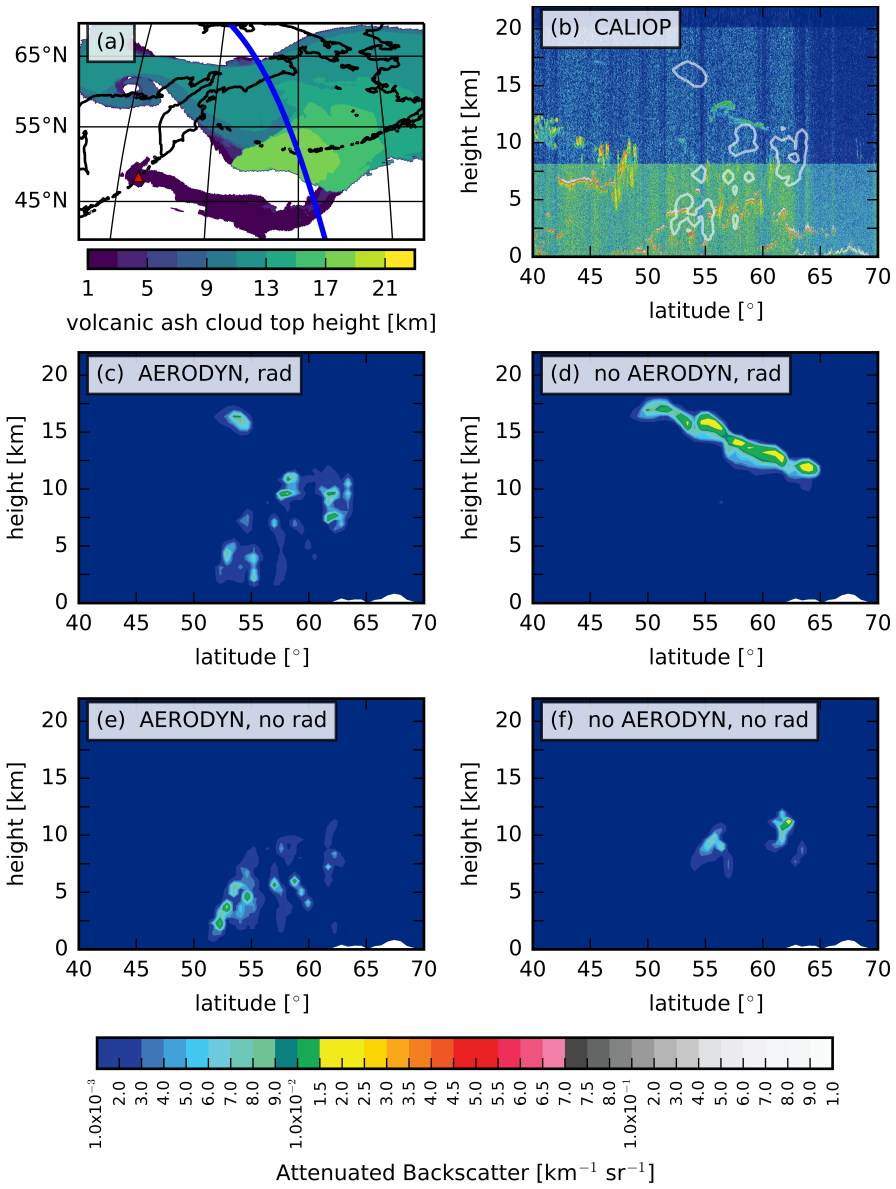

Figure B.4: Same as Fig. B.1 on 25 June 2019, 01:00 UTC.

C. Acronyms

AERODYN	Aerosol dynamics module
AHI	Advanced Himawari imager
AOD	Aerosol optical depth
CALIOP	Cloud-Aerosol Lidar with Orthogonal Polarization
CALIPSO	Cloud-Aerosol Lidar and Infrared Pathfinder Satellite Observation
CCN	Cloud condensation nuclei
CG	Conjugate gradients
DKRZ	Deutsches Klimarechenzentrum
DWD	Deutscher Wetterdienst
EASA	European Union Aviation Safety Agency
FBS	Fractions Brier score
FSS	Fractions skill score
fm	Free-molecular regime
IAU	Incremental analysis update
ICAO	International Civil Aviation Organization
ICON-ART	Icosahedral nonhydrostatic - aerosols and reactive trace gases
IMK	Institute of Meteorology and Climate Research
INP	Ice nucleating particle
IR	Infrared radiation
JAXA	Japanese Space Agency
JMA	Japanese Meteorological Agency

MER	Mass eruption rate
MPI-M	Max Planck Institute for Meteorology
NWP	Numerical weather prediction
nc	Near continuum regime
OMPS-LP	Ozone Mapping and Profiler Suite – Limb Profiler
PDC	Pyroclastic density current
PSAS	Physical Space Assimilation System
RRTM	Rapid Radiative Transfer Model
SAL	Structure Amplitude Location method
TROPOMI	Tropospheric monitoring instrument
UV	Ultraviolet radiation
VAAC	Volcanic Ash Advisory Center
VEI	Volcanic explosivity index

D. Symbols

Physical Variables

A	$[-]$	SAL–amplitude
A_p	$[\mathrm{m}^2]$	Area of particle cross section
α	$[-]$	Accommodation coefficient
B_λ	$[-]$	Spectral complex refractive index
β	$[\mathrm{m}^3\,\mathrm{s}^{-1}]$	Coagulation coefficient
β_a	$[\mathrm{m}^{-1}]$	Volume absorption coefficient
β_b	$[\mathrm{m}^{-1}]$	Volume backscattering coefficient
β_e	$[\mathrm{m}^{-1}]$	Volume extinction coefficient
β_s	$[\mathrm{m}^{-1}]$	Volume scattering coefficient
C_l	$[-]$	Cunningham correction factor for particle with diameter d_l
$Ca_{0,l}$	$[\mathrm{kg}^{-1}\,\mathrm{s}^{-1}]$	Coagulation rate of mass specific number concentration
$Ca_{3,l}$	$[\mathrm{kg\,kg}^{-1}\,\mathrm{s}^{-1}]$	Coagulation rate of mass mixing ratio
$Co_{3,l}$	$[\mathrm{kg\,kg}^{-1}\,\mathrm{s}^{-1}]$	Condensation rate of mass mixing ratio
$\widetilde{C}a_{0,l}$	$[\mathrm{m}^{-3}\,\mathrm{s}^{-1}]$	Coagulation rate of zeroth moment
$\widetilde{C}a_{3,l}$	$[\mathrm{m}^3\,\mathrm{m}^{-3}\,\mathrm{s}^{-1}]$	Coagulation rate of third moment
$\widetilde{C}o_{3,l}$	$[\mathrm{s}^{-1}]$	Condensation rate of third moment
c_{crit}	$[\mathrm{kg\,m}^{-3}]$	Critical concentration for production of sufate particles
$c_{\mathrm{H_2SO_4}}$	$[-]$	Mass mixing ratio of sulfuric acid
$\overline{c}$	$[\mathrm{m\,s}^{-1}]$	Mean thermal velocity of molecules
$\chi(d)$	$[\mathrm{m}^3\,\mathrm{s}^{-1}]$	Particle size dependent term for condensation rate
χ_T	$[-]$	Particle size independent term for condensation rate

D	$[\mathrm{m^2\,s^{-1}}]$	Diffusion coefficient (index indicating species)
$\mathscr{D}$	$[-]$	Domain
$d_{k,l}$	[m]	Median diameter for k^{th} moment of aerosol mode l
d_{max}	[m]	Largest possible distance in domain $\mathscr{D}$
d_p	[m]	Particle diameter
E	$[-]$	Number of ensemble members
$E_{0,l}$	$[\mathrm{kg^{-1}\,s^{-1}}]$	Emission rate of zeroth moment
$E_{3,l}$	$[\mathrm{kg\,kg^{-1}\,s^{-1}}]$	Emission rate of third moment
f_{lrt}	$[-]$	Fraction of particles for long-range transport
$f_{mod,i}$	$[-]$	Fraction at index i of model field
$f_{obs,i}$	$[-]$	Fraction at index i of observation field
f_{SAL}	$[-]$	Fraction for SAL threshold
Γ_l	$[\mathrm{kg\,m^{-2}}]$	Column integrated mass of species l
g	$[-]$	Asymmetry parameter
h	[m]	Height
I_l	$[\mathrm{s^{-1}}]$	Integral for condensation rate of mode l
I_λ	$[\mathrm{W\,m^2\,sr^{-1}}]$	Spectral radiance
Kn	$[-]$	Knudsen number
k_B	$[\mathrm{J\,K^{-1}}]$	Boltzmann constant
k_a	$[\mathrm{m^2\,kg^{-1}}]$	Mass specific absorption coefficient
k_b	$[\mathrm{m^2\,kg^{-1}}]$	Mass specific backscattering coefficient
k_e	$[\mathrm{m^2\,kg^{-1}}]$	Mass specific extinction coefficient
k_s	$[\mathrm{m^2\,kg^{-1}}]$	Mass specific scattering coefficient
L	$[-]$	SAL–location
λ	[m]	Wave length
λ_{air}	[m]	Mean free path of air

M_l	[kg m^{-3}]	Mass concentration of mode l
$M_{k,l}$	[m^k m^{-3}]	k-th moment of particle size distribution of mode l
$M_{H_2SO_4}$	[kg mol^{-1}]	Molar mass of sulfuric acid
$\dot{M}_3$	[s^{-1}]	Production rate of third moment of condensable material
m_{lrt}	[kg]	Mass of particles for long-range transport
μ	[kg m^{-1} s^{-1}]	Dynamic viscosity of air
n_{box}	[−]	FSS box size
n_{cell}	[−]	Number of grid cells
n_{lev}	[−]	Number of vertical levels
n_{obj}	[−]	Number of objects $\mathscr{R}_n$
N	[−]	Total number of particles
N_l	[m^{-3}]	Number concentration of mode l
$Nu_{0,l}$	[kg^{-1} s^{-1}]	Nucleation rate of mass specific number concentration
$Nu_{3,l}$	[kg kg^{-1} s^{-1}]	Nucleation rate of mass mixing ratio
Ω_l	[−]	Coefficient to divide condensable mass
ω	[−]	Single scattering albedo
p_A	[Pa]	Partial pressure of substance A
p_A^s	[Pa]	Saturation vapor pressure of substance A
$\widehat{\Psi}_{0,l}$	[kg^{-1}]	Mass specific number concentration of mode l
$\widehat{\Psi}_{3,l}$	[kg kg^{-1}]	Mass mixing ratio of mode l
$\psi_{0,l}$	[kg^{-1}]	Mass specific number concentration of particles with diameter d_p of mode l
$\psi_{3,l}$	[−]	Mass mixing ratio of particles with diameter d_p of mode l
Q_e	[−]	Extinction Efficiency
Q_{emiss}	[kg s^{-1} m^{-1}]	Emission rate
Q_s	[−]	Scattering Efficiency
q	[m]	Weighted averaged distance

$\mathfrak{R}$	$[\mathrm{J\,K^{-1}\,mol^{-1}}]$	Universal gas constant
$\mathscr{R}_n$	$[-]$	Object with index n
R	$[\mathrm{kg\,m^{-2}}]$	Arbitrary quantity for SAL method
R^*	$[\mathrm{kg\,m^{-2}}]$	Threshold value for evaluation metrics
r_d	[m]	Distance from Lidar instrument
r_e	[m]	Mean Earth radius
RH	[%]	Relative humidity
ρ_a	$[\mathrm{kg\,m^{-3}}]$	Density of dry air
ρ_p	$[\mathrm{kg\,m^{-3}}]$	Density of aerosol particle
S	$[-]$	SAL–structure
s	$[-]$	Saturation ratio
σ_e	$[\mathrm{m^2}]$	Extinction cross section
σ_l	$[-]$	Standard deviation of a mode l
σ_s	$[\mathrm{m^2}]$	Scattering cross section
T	[K]	Temperature
τ	$[-]$	Optical thickness
V	$[-]$	Weighted average of scaled volumes
V_n	$[-]$	Scaled volume of object n
$\mathbf{v}$	$[\mathrm{m\,s^{-1}}]$	Wind vector
$W_{0,l}$	$[\mathrm{kg^{-1}\,s^{-1}}]$	Wet deposition rate of zeroth moment
$W_{3,l}$	$[\mathrm{kg\,kg^{-1}\,s^{-1}}]$	Wet deposition rate of third moment
x	$[-]$	Size parameter
$\upsilon_{sed,k,l}$	$[\mathrm{m\,s^{-1}}]$	Sedimentation velocity for k^{th} moment of mode l
z	[m]	Vertical coordinate
$\mathbf{z}$	[m]	Center of mass

Data Assimilation Variables

$\mathbf{A}$	Matrix in linear equation system
$\mathbf{B}$	Covariance matrix of model errors
$\mathbf{b}$	Right hand side of linear equation system
$\mathbf{C}$	Gaussian matrix for localization
$\mathbf{H}$	Observation operator (linear)
$\mathbf{I}$	Identity matrix
$\mathbf{M}$	Preconditioner matrix
$\mathbf{R}$	Covariance matrix of observation errors
r	Observation error
$\mathbf{X}$	Ensemble matrix
$\overline{\mathbf{x}}$	State vector of ensemble mean
$\mathbf{x_a}$	Analysis model state
$\mathbf{x_b}$	Background model state (first guess)
$\mathbf{y}$	Observations vector
$\mathbf{z}$	Solution of linear equation system

Chemical Components

CH_4	Methane
Ca^{2+}	Calcium
Cl^-	Chlorine
CO	Carbon monoxide
CO_2	Carbon dioxide
H_2O	Water
H_2SO_4	Sulfuric acid
K^+	Potassium
Mg^{2+}	Magnesium
Na^+	Sodium
NH_4^+	Ammonium
NO_3^-	Nitrate
O_3	Ozone
SO_2	Sulfur dioxide
SO_4^{2-}	Sulfate

E. Bibliography

Abdelkader, M., S. Metzger, B. Steil, K. Klingmüller, H. Tost, A. Pozzer, G. Stenchikov, L. Barrie, and J. Lelieveld, 2017: Sensitivity of transatlantic dust transport to chemical aging and related atmospheric processes. *Atmos. Chem. Phys.*, **17 (6)**, 3799–3821. doi:10.5194/acp-17-3799-2017.

Albrecht, B. A., 1989: Aerosols, Cloud Microphysics, and Fractional Cloudiness. *Science*, **245 (4923)**, 1227–1230. doi:10.1126/science.245.4923.1227.

Andersson, S. M., B. G. Martinsson, J.-P. Vernier, J. Friberg, C. A. M. Brenninkmeijer, M. Hermann, P. F. J. van Velthoven, and A. Zahn, 2015: Significant radiative impact of volcanic aerosol in the lowermost stratosphere. *Nat. Commun.*, **6 (1)**. doi:10.1038/ncomms8692.

Arakawa, A. and V. R. Lamb, 1977: Computational Design of the Basic Dynamical Processes of the UCLA General Circulation Model. *General Circulation Models of the Atmosphere*, Chang, J., Ed., Elsevier, Methods in Computational Physics: Advances in Research and Applications, Vol. 17, 173–265. doi:https://doi.org/10.1016/B978-0-12-460817-7.50009-4.

Armienti, P., G. Macedonio, and M. T. Pareschi, 1988: A numerical model for simulation of tephra transport and deposition: Applications to May 18, 1980, Mount St. Helens eruption. *J. Geophys. Res.-Sol. Ea.*, **93 (B6)**, 6463–6476. doi:https://doi.org/10.1029/JB093iB06p06463.

Ayris, P. M. and P. Delmelle, 2012: Volcanic and atmospheric controls on ash iron solubility: A review. *Phys. Chem. Earth*, **45-46**, 103–112. doi:10.1016/j.pce.2011.04.013.

Bagheri, G. and C. Bonadonna, 2016: Aerodynamics of Volcanic Particles: Characterization of Size, Shape, and Settling Velocity. *Volcanic Ash*, Mackie, S., K. Cashman, H. Ricketts, A. Rust, and M. Watson, Eds., Elsevier, 39–52. doi:https://doi.org/10.1016/B978-0-08-100405-0.00005-7.

Bagnato, E., A. Aiuppa, A. Bertagnini, C. Bonadonna, R. Cioni, M. Pistolesi, M. Pedone, and A. Hoskuldsson, 2013: Scavenging of sulphur, halogens and trace metals by volcanic ash: The 2010 Eyjafjallajökull eruption. *Geochim. Cosmochim. Ac.*, **103**, 138–160. doi:10.1016/j.gca.2012.10.048.

Baldauf, M., A. Seifert, J. Förstner, D. Majewski, M. Raschendorfer, and T. Reinhardt, 2011: Operational Convective-Scale Numerical Weather Prediction with the COSMO Model: Description and Sensitivities. *Mon. Weather Rev.*, **139 (12)**, 3887 – 3905. doi:10.1175/MWR-D-10-05013.1.

Barrett, R., M. Berry, T. F. Chan, J. Demmel, J. Donato, J. Dongarra, V. Eijkhout, R. Pozo, C. Romine, and H. van der Vorst, 1994: *Templates for the Solution of Linear Systems: Building Blocks for Iterative Methods*. Society for Industrial and Applied Mathematics, 135 pp., URL `https://epubs.siam.org/doi/abs/10.1137/1.9781611971538`.

Beckett, F. M., C. S. Witham, S. J. Leadbetter, R. Crocker, H. N. Webster, M. C. Hort, A. R. Jones, B. J. Devenish, and D. J. Thomson, 2020: Atmospheric Dispersion Modelling at the London VAAC: A Review of Developments since the 2010 Eyjafjallajökull Volcano Ash Cloud. *Atmosphere-Basel*, **11 (4)**, 352. doi:10.3390/atmos11040352.

Bernard, A. and W. I. Rose, 1990: The injection of sulfuric acid aerosols in the stratosphere by the El Chichón volcano and its related hazards to the international air traffic. *Nat. Hazards*, **3 (1)**, 59–67. doi:10.1007/BF00144974.

Binkowski, F. S. and U. Shankar, 1995: The regional particulate matter model: 1. model description and preliminary results. *J. Geophys. Res.-Atmos.*, **100 (D12)**, 26 191–26 209. doi:https://doi.org/10.1029/95JD02093.

Bloom, S. C., L. L. Takacs, A. M. da Silva, and D. Ledvina, 1996: Data Assimilation Using Incremental Analysis Updates. *Mon. Weather Rev.*, **124 (6)**, 1256 – 1271. doi:10.1175/1520-0493(1996)124<1256:DAUIAU>2.0.CO;2.

Bocquet, M., H. Elbern, H. Eskes, M. Hirtl, R. Žabkar, G. R. Carmichael, J. Flemming, A. Inness, M. Pagowski, J. L. Pérez Camaño, P. E. Saide, R. San Jose, M. Sofiev, J. Vira, A. Baklanov, C. Carnevale, G. Grell, and C. Seigneur, 2015: Data assimilation in atmospheric chemistry models: current status and future prospects for coupled chemistry meteorology models. *Atmos. Chem. Phys.*, **15 (10)**, 5325–5358. doi:10.5194/acp-15-5325-2015.

Bohren, C. F. and D. R. Huffman, 1983: *Absorption and Scattering of Light by Small Particles*. Wiley, New York, 530 pp.

Bonadonna, C. and S. Scollo, 2013: IAVCEI Commission on Tephra Hazard Modelling. URL `http://www.ct.ingv.it/iavcei/results.htm`, last access: 03 September 2020.

Bond, T. C., G. Habib, and R. W. Bergstrom, 2006: Limitations in the enhancement of visible light absorption due to mixing state. *J. Geophys. Res.-Atmos.*, **111 (D20)**. doi:10.1029/2006JD007315.

Boucher, O., 2015: *Atmospheric Aerosols*. Springer, Netherlands, 311 pp.

Boucher, O., D. Randall, P. Artaxo, C. Bretherton, G. Feingold, P. Forster, V.-M. Kerminen, Y. Kondo, H. Liao, U. Lohmann, P. Rasch, S. K. Satheesh, S. Sherwood, B. Stevens, and X. Y. Zhang, 2013: Clouds and aerosols. *Climate Change 2013: The Physical Science Basis. Contribution*

of Working Group I to the Fifth Assessment Report of the Intergovernmental Panel on Climate Change, Stocker, T. F., D. Qin, G.-K. Plattner, M. Tignor, S. K. Allen, J. Doschung, A. Nauels, Y. Xia, V. Bex, and P. M. Midgley, Eds., Cambridge University Press, Cambridge, UK, 571–657. doi:10.1017/CBO9781107415324.016.

Brown, R. J., C. Bonadonna, and A. J. Durant, 2012: A review of volcanic ash aggregation. *Phys. Chem. Earth*, **45-46**, 65–78. doi:10.1016/j.pce.2011.11.001.

Bruckert, J., G. A. Hoshyaripour, A. Horváth, L. Muser, F. J. Prata, C. Hoose, and B. Vogel, 2021: Online treatment of eruption dynamics improves the volcanic ash and SO_2 dispersion forecast: case of the Raikoke 2019 eruption. *Atmos. Chem. Phys. Discussions*, **2021**, 1–23. doi:10.5194/acp-2021-459.

Budd, L., S. Griggs, D. Howarth, and S. Ison, 2011: A Fiasco of Volcanic Proportions? Eyjafjallajökull and the Closure of European Airspace. *Mobilities*, **6 (1)**, 31–40. doi:10.1080/17450101.2011.532650.

Caldas-Alvarez, A., S. Khodayar, and P. Knippertz, 2021: The impact of GPS and high-resolution radiosonde nudging on the simulation of heavy precipitation during HyMeX IOP6. *Weather Clim. Dynam.*, **2 (3)**, 561–580. doi:10.5194/wcd-2-561-2021.

Cantor, R., 1998: Complete avoidance of volcanic ash is only procedure that guarantees flight safety. *ICAO Journal*, **53 (7)**, 18–19. URL `https://www.icao.int/publications/journalsreports/1998/5307.djvu`.

Carboni, E., R. G. Grainger, T. A. Mather, D. M. Pyle, G. E. Thomas, R. Siddans, A. J. A. Smith, A. Dudhia, M. E. Koukouli, and D. Balis, 2016: The vertical distribution of volcanic SO_2 plumes measured by IASI. *Atmos. Chem. Phys.*, **16 (7)**, 4343–4367. doi:10.5194/acp-16-4343-2016.

Carn, S. A., A. J. Krueger, N. A. Krotkov, K. Yang, and K. Evans, 2008: Tracking volcanic sulfur dioxide clouds for aviation hazard mitigation. *Nat. Hazards*, **51 (2)**, 325–343. doi:10.1007/s11069-008-9228-4.

Carrassi, A., M. Bocquet, L. Bertino, and G. Evensen, 2018: Data assimilation in the geosciences: An overview of methods, issues, and perspectives. *WIREs Clim. Change*, **9 (5)**, e535. doi:https://doi.org/10.1002/wcc.535.

Casadevall, T. J., 1994: Volcanic ash and aviation safety: Proceedings of the first international symposium on volcanic ash and aviation safety. Tech. rep., US Geological Survey, URL `https://pubs.er.usgs.gov/publication/b2047`, doi:10.3133/b2047.

Casadevall, T. J., P. J. D. Reyes, and D. J. Schneider, 1996: The 1991 Pinatubo Eruptions and Their Effects on Aircraft Operations. *Fire and Mud: Eruptions and Lahars of Mount Pinatubo, Philippines*, 625 – 636.

Clarisse, L., D. Hurtmans, A. J. Prata, F. Karagulian, C. Clerbaux, M. De Mazière, and P.-F. Coheur, 2010: Retrieving radius, concentration, optical depth, and mass of different types of aerosols from high-resolution infrared nadir spectra. *Appl. Optics*, **49 (19)**, 3713–3722. doi:10.1364/AO.49.003713.

Clarisse, L. and F. Prata, 2016: Infrared sounding of volcanic ash. *Volcanic Ash*, Mackie, S., K. Cashman, H. Ricketts, A. Rust, and M. Watson, Eds., Elsevier, 189–215. doi:https://doi.org/10.1016/B978-0-08-100405-0.00017-3.

Colella, P. and P. R. Woodward, 1984: The piecewise parabolic method (ppm) for gas-dynamical simulations. *J. Comput. Phys.*, **54 (1)**, 174–201. doi:https://doi.org/10.1016/0021-9991(84)90143-8.

Conjugate gradient method, 2021: Conjugate gradient method. URL `https://en.wikipedia.org/w/index.php?title=Conjugate_gradient_method&oldid=1043940413`, last access: 27 October 2021.

de Leeuw, J., A. Schmidt, C. S. Witham, N. Theys, I. A. Taylor, R. G. Grainger, R. J. Pope, J. Haywood, M. Osborne, and N. I. Kristiansen, 2021: The 2019 Raikoke volcanic eruption – Part 1: Dispersion model simulations and satellite retrievals of volcanic sulfur dioxide. *Atmos. Chem. Phys.*, **21 (14)**, 10 851–10 879. doi:10.5194/acp-21-10851-2021.

Dee, D. P., S. M. Uppala, A. J. Simmons, P. Berrisford, P. Poli, S. Kobayashi, U. Andrae, M. A. Balmaseda, G. Balsamo, P. Bauer, P. Bechtold, A. C. M. Beljaars, L. van de Berg, J. Bidlot, N. Bormann, C. Delsol, R. Dragani, M. Fuentes, A. J. Geer, L. Haimberger, S. B. Healy, H. Hersbach, E. V. Hólm, L. Isaksen, P. Kållberg, M. Köhler, M. Matricardi, A. P. McNally, B. M. Monge-Sanz, J.-J. Morcrette, B.-K. Park, C. Peubey, P. de Rosnay, C. Tavolato, J.-N. Thépaut, and F. Vitart, 2011: The ERA-Interim reanalysis: configuration and performance of the data assimilation system. *Q. J. Roy. Meteor. Soc.*, **137 (656)**, 553–597. doi:10.1002/qj.828.

Deetz, K., H. Vogel, S. Haslett, P. Knippertz, H. Coe, and B. Vogel, 2018: Aerosol liquid water content in the moist southern west african monsoon layer and its radiative impact. *Atmos. Chem. Phys.*, **18 (19)**, 14 271–14 295. doi:10.5194/acp-18-14271-2018.

Dellino, P., M. T. Gudmundsson, G. Larsen, D. Mele, J. A. Stevenson, T. Thordarson, and B. Zimanowski, 2012: Ash from the Eyjafjallajökull eruption (Iceland): Fragmentation processes and aerodynamic behavior. *J. Geophys. Res.-Sol. Ea.*, **117 (B9)**. doi:https://doi.org/10.1029/2011JB008726.

Delmelle, P., M. Lambert, Y. Dufrêne, P. Gerin, and N. Óskarsson, 2007: Gas/aerosol-ash interaction in volcanic plumes: New insights from surface analyses of fine ash particles. *Earth Planet Sc. Lett.* doi:10.1016/j.epsl.2007.04.052.

Dingwell, A., A. Rutgersson, B. Claremar, S. Arellano, M. M. Yalire, and B. Galle, 2016: Seasonal and diurnal patterns in the dispersion of so2 from mt. nyiragongo. *Atmos. Environ.*, **132**, 19–29. doi:https://doi.org/10.1016/j.atmosenv.2016.02.030.

Doyle, G. J., 1961: Self-nucleation in the sulfuric acid-water system. *J. Chem. Phys.*, **35 (3)**, 795–799. doi:10.1063/1.1701218.

Durant, A. J., C. Bonadonna, and C. J. Horwell, 2010: Atmospheric and environmental impacts of volcanic particulates. *Elements*, **6 (4)**, 235–240. doi:10.2113/gselements.6.4.235.

EASA SIB No.: 2010-17R7, 2015: 2010-17R7: [Correction] Flight in Airspace with Contamination of Volcanic Ash. Tech. rep., European Aviation Safety Agency, URL `https://ad.easa.europa.eu/ad/2010-17R7#download`, last access: 01 November 2021.

Eckhardt, S., A. J. Prata, P. Seibert, K. Stebel, and A. Stohl, 2008: Estimation of the vertical profile of sulfur dioxide injection into the atmosphere by a volcanic eruption using satellite column measurements and inverse transport modeling. *Atmos. Chem. Phys.*, **8 (14)**, 3881–3897. doi:10.5194/acp-8-3881-2008.

Eliaz, N., G. Shemesh, and R. Latanision, 2002: Hot corrosion in gas turbine components. *Eng. Fail. Anal.*, **9 (1)**, 31 – 43. doi:https://doi.org/10.1016/S1350-6307(00)00035-2.

Flemming, J. and A. Inness, 2013: Volcanic sulfur dioxide plume forecasts based on UV satellite retrievals for the 2011 grímsvötn and the 2010 eyjafjallajökull eruption. *J. Geophys. Res.-Atmos.*, **118 (17)**, 10,172–10,189. doi:10.1002/jgrd.50753.

Folch, A., A. Costa, and G. Macedonio, 2016: FPLUME-1.0: An integral volcanic plume model accounting for ash aggregation. *Geosci. Model Dev.*, **9 (1)**, 431–450. doi:10.5194/gmd-9-431-2016.

Fountoukis, C. and A. Nenes, 2007: ISORROPIA II: a computationally efficient thermodynamic equilibrium model for K^+–Ca^{2+}–Mg^{2+}–NH_4^+–Na^+–SO_4^{2-}–NO_3^-–Cl^-–H_2O aerosols. *Atmos. Chem. Phys.*, **7**, 4639–4659. doi:10.5194/acp-7-4639-2007.

Fu, G., A. Heemink, S. Lu, A. Segers, K. Weber, and H.-X. Lin, 2016: Model-based aviation advice on distal volcanic ash clouds by assimilating aircraft in situ measurements. *Atmos. Chem. Phys.*, **16 (14)**, 9189–9200. doi:10.5194/acp-16-9189-2016.

Fuchs, N. and A. Sutugin, 1971: High-dispersed aerosols. *Topics in Current Aerosol Research*, HIDY, G. and J. BROCK, Eds., Pergamon, International Reviews in Aerosol Physics and Chemistry, 1. doi:https://doi.org/10.1016/B978-0-08-016674-2.50006-6.

Gasch, P., 2016: Numerical simulations of an exceptional dust event in the Eastern Mediterranean including the mineral dust radiative feedback. Master's thesis, Institute of Meteorology and Climate Research, Karlsruhe Institute of Technology.

Gasch, P., D. Rieger, C. Walter, P. Khain, Y. Levi, P. Knippertz, and B. Vogel, 2017: Revealing the meteorological drivers of the September 2015 severe dust event in the Eastern Mediterranean. *Atmos. Chem. Phys.*, **17 (22)**, 13 573–13 604. doi:10.5194/acp-17-13573-2017.

Gassmann, A. and H.-J. Herzog, 2008: Towards a consistent numerical compressible non-hydrostatic model using generalized Hamiltonian tools. *Q. J. Roy. Meteor. Soc.*, **134 (635)**, 1597–1613. doi:https://doi.org/10.1002/qj.297.

Giorgetta, M. A., R. Brokopf, T. Crueger, M. Esch, S. Fiedler, J. Helmert, C. Hohenegger, L. Kornblueh, M. Köhler, E. Manzini, T. Mauritsen, C. Nam, T. Raddatz, S. Rast, D. Reinert, M. Sakradzija, H. Schmidt, R. Schneck, R. Schnur, L. Silvers, H. Wan, G. Zängl, and B. Stevens, 2018: ICON-A, the Atmosphere Component of the ICON Earth System Model: I. Model Description. *J. Adv. Model. Earth Sy.*, **10 (7)**, 1613–1637. doi:10.1029/2017MS001242.

Gordon, I. E., L. S. Rothman, C. Hill, R. V. Kochanov, Y. Tan, P. F. Bernath, M. Birk, V. Boudon, A. Campargue, K. V. Chance, B. J. Drouin, J. M. Flaud, R. R. Gamache, J. T. Hodges, D. Jacquemart, V. I. Perevalov, A. Perrin, K. P. Shine, M. A. Smith, J. Tennyson, G. C. Toon, H. Tran, V. G. Tyuterev, A. Barbe, A. G. Császár, V. M. Devi, T. Furtenbacher, J. J. Harrison, J. M. Hartmann, A. Jolly, T. J. Johnson, T. Karman, I. Kleiner, A. A. Kyuberis, J. Loos, O. M. Lyulin, S. T. Massie, S. N. Mikhailenko, N. Moazzen-Ahmadi, H. S. Müller, O. V. Naumenko, A. V. Nikitin, O. L. Polyansky, M. Rey, M. Rotger, S. W. Sharpe, K. Sung, E. Starikova, S. A. Tashkun, J. V. Auwera, G. Wagner, J. Wilzewski, P. Wcisło, S. Yu, and E. J. Zak, 2017: The HITRAN2016 molecular spectroscopic database. *J. Quant. Spectrosc. Ra.*, **203**, 3–69. doi:10.1016/j.jqsrt.2017.06.038.

Gouhier, M., J. Eychenne, N. Azzaoui, A. Guillin, M. Deslandes, M. Poret, A. Costa, and P. Husson, 2019: Low efficiency of large volcanic eruptions in transporting very fine ash into the atmosphere. *Sci. Rep.-UK*, **9 (1)**, 1–12. doi:10.1038/s41598-019-38595-7.

Grainger, R. G., D. M. Peters, G. E. Thomas, A. J. A. Smith, R. Siddans, E. Carboni, and A. Dudhia, 2013: Measuring volcanic plume and ash properties from space. *Geol. Soc. Spec. Publ.*, **380 (1)**, 293–320. doi:10.1144/SP380.7.

Grell, G. A., S. E. Peckham, R. Schmitz, S. A. McKeen, G. Frost, W. C. Skamarock, and B. Eder, 2005: Fully coupled "online" chemistry within the WRF model. *Atmos. Environ.*, **39 (37)**, 6957–6975. doi:https://doi.org/10.1016/j.atmosenv.2005.04.027.

Gruber, S., U. Blahak, F. Haenel, C. Kottmeier, T. Leisner, H. Muskatel, T. Storelvmo, and B. Vogel, 2019: A Process Study on Thinning of Arctic Winter Cirrus Clouds With High-Resolution ICON-ART Simulations. *J. Geophys. Res.-Atmos.*, **124 (11)**, 5860–5888. doi:https://doi.org/10.1029/2018JD029815.

Gudmundsson, M. T., T. Thordarson, A. Höskuldsson, G. Larsen, H. Björnsson, F. J. Prata, B. Oddsson, E. Magnússon, T. Högnadóttir, G. N. Petersen, C. L. Hayward, J. A. Stevenson, and I. Jónsdóttir, 2012: Ash generation and distribution from the April-May 2010 eruption of Eyjafjallajökull, Iceland. *Sci. Rep.-UK*, **2 (572)**. doi:https://doi.org/10.1038/srep00572.

Guffanti, M., T. Casadevall, and K. Budding, 2010: Encounters of aircraft with volcanic ash clouds: A compilation of known incidents, 1953-2009. *U.S. Geological Survey Data Series 545*, **1.0**, 12. URL `http://pubs.usgs.gov/ds/545`.

Guth, J., B. Josse, V. Marécal, M. Joly, and P. Hamer, 2016: First implementation of secondary inorganic aerosols in the MOCAGE version R2.15.0 chemistry transport model. *Geosci. Model Dev.*, **9 (1)**, 137–160. doi:10.5194/gmd-9-137-2016.

Harvey, N. J., N. Huntley, H. F. Dacre, M. Goldstein, D. Thomson, and H. Webster, 2018: Multi-level emulation of a volcanic ash transport and dispersion model to quantify sensitivity to uncertain parameters. *Nat. Hazard. Earth Sys.*, **18 (1)**, 41–63. doi:10.5194/nhess-18-41-2018.

Heaviside, C., C. Witham, and S. Vardoulakis, 2021: Potential health impacts from sulphur dioxide and sulphate exposure in the UK resulting from an Icelandic effusive volcanic eruption. *Sci. Total Environ.*, **774**, 145 549. doi:https://doi.org/10.1016/j.scitotenv.2021.145549.

Heinze, R., A. Dipankar, C. C. Henken, C. Moseley, O. Sourdeval, S. Trömel, X. Xie, P. Adamidis, F. Ament, H. Baars, C. Barthlott, A. Behrendt, U. Blahak, S. Bley, S. Brdar, M. Brueck, S. Crewell, H. Deneke, P. Di Girolamo, R. Evaristo, J. Fischer, C. Frank, P. Friederichs, T. Göcke, K. Gorges, L. Hande, M. Hanke, A. Hansen, H.-C. Hege, C. Hoose, T. Jahns, N. Kalthoff, D. Klocke, S. Kneifel, P. Knippertz, A. Kuhn, T. van Laar, A. Macke, V. Maurer, B. Mayer, C. I. Meyer, S. K. Muppa, R. A. J. Neggers, E. Orlandi, F. Pantillon, B. Pospichal, N. Röber, L. Scheck, A. Seifert, P. Seifert, F. Senf, P. Siligam, C. Simmer, S. Steinke, B. Stevens, K. Wapler, M. Weniger, V. Wulfmeyer, G. Zängl, D. Zhang, and J. Quaas, 2017: Large-eddy simulations over Germany using ICON: a comprehensive evaluation. *Q. J. Roy. Meteor. Soc.*, **143 (702)**, 69–100. doi:10.1002/qj.2947.

Hestenes, M. and E. Stiefel, 1952: Methods of conjugate gradients for solving linear systems. *J. Res. Nat. Bur. Stand.*, **49**, 409–435. URL `https://nvlpubs.nist.gov/nistpubs/jres/049/jresv49n6p409_A1b.pdf`.

Hirtl, M., M. Stuefer, D. Arnold, G. Grell, C. Maurer, S. Natali, B. Scherllin-Pirscher, and P. Webley, 2019: The effects of simulating volcanic aerosol radiative feedbacks with WRF-Chem during the Eyjafjallajökull eruption, April and May 2010. *Atmos. Environ.*, **198**, 194–206. doi:https://doi.org/10.1016/j.atmosenv.2018.10.058.

Hopkins, A. T. and C. J. Bridgman, 1985: A volcanic ash transport model and analysis of Mount St. Helens ashfall. *J. Geophys. Res.-Atmos.*, **90 (D6)**, 10 620–10 630. doi:https://doi.org/10.1029/JD090iD06p10620.

Hoshyaripour, G. A., V. Bachmann, J. Förstner, A. Steiner, H. Vogel, F. Wagner, C. Walter, and B. Vogel, 2019: Effects of Particle Non-Sphericity on Dust Optical Properties in a Forecast System: Implications for Model-Observation Comparison. *J. Geophys. Res.-Atmos.* doi:10.1029/2018JD030228.

Hoshyaripour, G. a., M. Hort, and B. Langmann, 2015: Ash iron mobilization through physicochemical processing in volcanic eruption plumes: a numerical modeling approach. *Atmos. Chem. Phys.*, **15 (16)**, 9361–9379. doi:10.5194/acp-15-9361-2015.

Hoyle, C. R., V. Pinti, A. Welti, B. Zobrist, C. Marcolli, B. Luo, A. Höskuldsson, H. B. Mattsson, O. Stetzer, T. Thorsteinsson, G. Larsen, and T. Peter, 2011: Ice nucleation properties of volcanic ash from Eyjafjallajökull. *Atmos. Chem. Phys.*, **11 (18)**, 9911–9926. doi:10.5194/acp-11-9911-2011.

Jaecker-Voirol, A. and P. Mirabel, 1989: Heteromolecular nucleation in the sulfuric acid-water system. *Atmos. Environ.*, **23 (9)**, 2053–2057. doi:https://doi.org/10.1016/0004-6981(89)90530-1.

Johnson, B., K. Turnbull, P. Brown, R. Burgess, J. Dorsey, A. Baran, H. Webster, J. Haywood, R. Cotton, Z. Ulanowski, E. Hesse, A. Woolley, and P. Rosenberg, 2012: In situ observations of volcanic ash clouds from the FAAM aircraft during the eruption of Eyjafjallajokull in 2010. *J. Geophys. Res.-Atmos.*, **117 (D20)**. URL `https://eprints.whiterose.ac.uk/79060/`.

Jones, A., D. Thomson, M. Hort, and B. Devenish, 2007: The u.k. met office's next-generation atmospheric dispersion model, NAME III. *Air Pollution Modeling and Its Application XVII*, Springer, Boston, MA, 580–589. doi:10.1007/978-0-387-68854-1_62.

Kaiser, J. C., J. Hendricks, M. Righi, N. Riemer, R. A. Zaveri, S. Metzger, and V. Aquila, 2014: The MESSy aerosol submodel MADE3 (v2.0b): Description and a box model test. *Geosci. Model Dev.*, **7 (3)**, 1137–1157. doi:10.5194/gmd-7-1137-2014.

Kazakov, A. and M. Frenklach, 1998: Dynamic modeling of soot particle coagulation and aggregation: Implementation with the method of moments and application to high-pressure laminar premixed flames. *Combust. Flame*, **114**, 484–501. doi:https://doi.org/10.1016/S0010-2180(97)00322-2.

Kerminen, V.-M., J. V. Niemi, H. Timonen, M. Aurela, A. Frey, S. Carbone, S. Saarikoski, K. Teinilä, J. Hakkarainen, J. Tamminen, J. Vira, M. Prank, M. Sofiev, and R. Hillamo, 2011: Characterization of a volcanic ash episode in southern Finland caused by the Grimsvötn eruption in Iceland in May 2011. *Atmos. Chem. Phys.*, **11 (23)**, 12 227–12 239. doi:10.5194/acp-11-12227-2011.

Kerminen, V.-M. and A. S. Wexler, 1995: The interdependence of aerosol processes and mixing in point source plumes. *Atmos. Environ.*, **29 (3)**, 361 – 375. doi:https://doi.org/10.1016/1352-2310(94)00262-J.

Khaykin, S. M., S. Godin-Beekmann, P. Keckhut, A. Hauchecorne, J. Jumelet, J.-P. Vernier, A. Bourassa, D. A. Degenstein, L. A. Rieger, C. Bingen, F. Vanhellemont, C. Robert, M. DeLand, and P. K. Bhartia, 2017: Variability and evolution of the midlatitude stratospheric aerosol budget from 22 years of ground-based lidar and satellite observations. *Atmos. Chem. Phys.*, **17 (3)**, 1829–1845. doi:10.5194/acp-17-1829-2017.

Kipling, Z., P. Stier, C. E. Johnson, G. W. Mann, N. Bellouin, S. E. Bauer, T. Bergman, M. Chin, T. Diehl, S. J. Ghan, T. Iversen, A. Kirkevåg, H. Kokkola, X. Liu, G. Luo, T. van Noije, K. J. Pringle, K. von Salzen, M. Schulz, Ø. Seland, R. B. Skeie, T. Takemura, K. Tsigaridis, and K. Zhang, 2016: What controls the vertical distribution of aerosol? Relationships between process sensitivity in HadGEM3–UKCA and inter-model variation from AeroCom Phase II. *Atmos. Chem. Phys.*, **16 (4)**, 2221–2241. doi:10.5194/acp-16-2221-2016.

Kristiansen, N. I., A. Stohl, A. J. Prata, A. Richter, S. Eckhardt, P. Seibert, A. Hoffmann, C. Ritter, L. Bitar, T. J. Duck, and K. Stebel, 2010: Remote sensing and inverse transport modeling of the kasatochi eruption sulfur dioxide cloud. *J. Geophys. Res.-Atmos.*, **115 (D2)**. doi:https://doi.org/10.1029/2009JD013286.

Kulmala, M. and A. Laaksonen, 1990: Binary nucleation of water–sulfuric acid system: Comparison of classical theories with different H2SO4 saturation vapor pressures. *J. Chem. Phys.*, **93 (1)**, 696–701. doi:10.1063/1.459519.

Kylling, A., M. Kahnert, H. Lindqvist, and T. Nousiainen, 2014: Volcanic ash infrared signature: porous non-spherical ash particle shapes compared to homogeneous spherical ash particles. *Atmos. Meas. Tech.*, **7 (4)**, 919–929. doi:10.5194/amt-7-919-2014.

Leuenberger, D., M. Koller, O. Fuhrer, and C. Schär, 2010: A generalization of the sleve vertical coordinate. *Mon. Weather Rev.*, **138 (9)**, 3683 – 3689. doi:10.1175/2010MWR3307.1.

Liu, Y.-A., Z. Li, and M. Huang, 2019: Towards a data-derived observation error covariance matrix for satellite measurements. *Remote Sens.*, **11 (15)**. doi:10.3390/rs11151770.

Lohmann, U. and J. Feichter, 2001: Can the direct and semi-direct aerosol effect compete with the indirect effect on a global scale? *Geophys. Res. Lett.*, **28 (1)**, 159–161. doi:https://doi.org/10.1029/2000GL012051.

Lu, S., H. X. Lin, A. Heemink, A. Segers, and G. Fu, 2016: Estimation of volcanic ash emissions through assimilating satellite data and ground-based observations. *J. Geophys. Res.-Atmos.*, **121 (18)**, 10,971–10,994. doi:https://doi.org/10.1002/2016JD025131.

Mackie, S. and M. Watson, 2014: Probabilistic detection of volcanic ash using a bayesian approach. *J. Geophys. Res.-Atmos.*, **119 (5)**, 2409–2428. doi:10.1002/2013JD021077.

Malinina, E., 2019: Retrieval of stratospheric aerosol characteristics from spaceborne limb sounders. Ph.D. thesis, University of Bremen. URL http://nbn-resolving.de/urn:nbn:de:gbv:46-00107153-12.

Malinina, E., A. Rozanov, U. Niemeier, S. Wallis, C. Arosio, F. Wrana, C. Timmreck, C. von Savigny, and J. P. Burrows, 2021: Changes in stratospheric aerosol extinction coefficient after the 2018 Ambae eruption as seen by OMPS-LP and MAECHAM5-HAM. *Atmos. Chem. Phys.*, **21 (19)**, 14 871–14 891. doi:10.5194/acp-21-14871-2021.

Marti, A., A. Folch, O. Jorba, and Z. Janjic, 2017: Volcanic ash modeling with the online NMMB-MONARCH-ASH v1.0 model: model description, case simulation, and evaluation. *Atmos. Chem. Phys.*, **17 (6)**, 4005–4030. doi:10.5194/acp-17-4005-2017.

Mastin, L., M. Guffanti, R. Servranckx, P. Webley, S. Barsotti, K. Dean, A. Durant, J. Ewert, A. Neri, W. Rose, D. Schneider, L. Siebert, B. Stunder, G. Swanson, A. Tupper, A. Volentik, and C. Waythomas, 2009: A multidisciplinary effort to assign realistic source parameters to models of volcanic ash-cloud transport and dispersion during eruptions. *J. Volcanol. Geoth. Res.*, **186 (1-2)**, 10–21. doi:10.1016/j.jvolgeores.2009.01.008.

Mastin, L. G., 2007: A user-friendly one-dimensional model for wet volcanic plumes. *Geochem. Geophy. Geosy.*, **8 (3)**. doi:10.1029/2006GC001455.

Mather, T. A., 2008: Volcanism and the atmosphere: the potential role of the atmosphere in unlocking the reactivity of volcanic emissions. *Philos. T. R. Soc. A*, **366 (1885)**, 4581–4595. doi:10.1098/rsta.2008.0152.

Mätzler, C., 2002: MATLAB Functions for Mie Scattering and Absorption. Tech. rep., University of Bern, URL https://boris.unibe.ch/146551/1/201-1.pdf, last access: 03 December 2021.

Mazzocchi, M., F. Hansstein, and M. Ragona, 2010: The 2010 volcanic ash cloud and its financial impact on the european airline industry. *CESifo Forum*, **11 (2)**, 92–100. URL http://hdl.handle.net/10419/166397.

Mie, G., 1908: Beiträge zur Optik trüber Medien, speziell kolloidaler Metallösungen. *Ann. Phys.*, **330 (3)**, 377–445. doi:https://doi.org/10.1002/andp.19083300302.

Mishchenko, M. I., 2014: *Electromagnetic scattering by particles and particle groups : an introduction*. Cambridge University Press, Cambridge [u.a.], 377 pp.

Mishchenko, M. I., A. A. Lacis, B. E. Carlson, and L. D. Travis, 1995: Nonsphericity of dust-like tropospheric aerosols: Implications for aerosol remote sensing and climate modeling. *Geophys. Res. Lett.*, **22 (9)**, 1077–1080. doi:https://doi.org/10.1029/95GL00798.

Mishchenko, M. I., L. D. Travis, R. A. Kahn, and R. A. West, 1997: Modeling phase functions for dustlike tropospheric aerosols using a shape mixture of randomly oriented polydisperse spheroids. *J. Geophys. Res.-Atmos.*, **102 (D14)**, 16 831–16 847. doi:https://doi.org/10.1029/96JD02110.

Miura, H., 2007: An upwind-biased conservative advection scheme for spherical hexagonal–pentagonal grids. *Mon. Weather Rev.*, **135 (12)**, 4038 – 4044. doi:10.1175/2007MWR2101.1.

Mlawer, E. J., S. J. Taubman, P. D. Brown, M. J. Iacono, and S. A. Clough, 1997: Radiative transfer for inhomogeneous atmospheres: RRTM, a validated correlated-k model for the longwave. *J. Geophys. Res.-Atmos.*, **102 (D14)**, 16 663–16 682. doi:10.1029/97jd00237.

Montoya, O. L. Q., E. D. Niño-Ruiz, and N. Pinel, 2020: On the mathematical modelling and data assimilation for air pollution assessment in the tropical andes. *Environ. Sci. Pollut. R.*, **27 (29)**, 35 993–36 012. doi:10.1007/s11356-020-08268-4.

Morcrette, J.-J., H. W. Barker, J. N. S. Cole, M. J. Iacono, and R. Pincus, 2008: Impact of a New Radiation Package, McRad, in the ECMWF Integrated Forecasting System. *Mon. Weather Rev.*, **136 (12)**, 4773 – 4798. doi:10.1175/2008MWR2363.1.

Moxnes, E. D., N. I. Kristiansen, A. Stohl, L. Clarisse, A. Durant, K. Weber, and A. Vogel, 2014: Separation of ash and sulfur dioxide during the 2011 Grímsvötn eruption. *J. Geophys. Res.-Atmos.*, **119 (12)**, 7477–7501. doi:10.1002/2013jd021129.

Muser, L. O., G. A. Hoshyaripour, J. Bruckert, A. Horváth, E. Malinina, S. Wallis, F. J. Prata, A. Rozanov, C. von Savigny, H. Vogel, and B. Vogel, 2020: Particle aging and aerosol–radiation interaction affect volcanic plume dispersion: evidence from the Raikoke 2019 eruption. *Atmos. Chem. Phys.*, **20 (23)**, 15 015–15 036. doi:10.5194/acp-20-15015-2020.

Muth, L. J., 2019: Simulation of primary and secondary aerosols of the Mt. Pinatubo eruption 1991 and their radiative effects. Master's thesis, Institute of Meteorology and Climate Research, Karlsruhe Institute of Technology.

Nakamura, G. and R. Potthast, 2015: *Inverse Modeling*. 2053-2563, Institute of Physics Publishing, 509 pp., URL `http://dx.doi.org/10.1088/978-0-7503-1218-9`.

Navon, I. M., D. N. Daescu, and Z. Liu, 2005: The impact of background error on incomplete observations for 4d-var data assimilation with the fsu gsm. *Computational Science – ICCS 2005*, Springer Berlin Heidelberg, Berlin, Heidelberg, 837–844. doi:10.1007/11428848_107.

Nenes, A., S. Pandis, and C. Pilinis, 1998: Isorropia: A new thermodynamic equilibrium model for multiphase multicomponent inorganic aerosols. *Aquat. Geochem.*, **4**, 123–152. doi:10.1023/A:1009604003981.

Newhall, C. G. and S. Self, 1982: The volcanic explosivity index (VEI) an estimate of explosive magnitude for historical volcanism. *J. Geophys. Res.-Oceans*, **87 (C2)**, 1231–1238. doi:https://doi.org/10.1029/JC087iC02p01231.

Niemeier, U. and H. Schmidt, 2017: Changing transport processes in the stratosphere by radiative heating of sulfate aerosols. *Atmos. Chem. Phys.*, **17 (24)**, 14 871–14 886. doi:10.5194/acp-17-14871-2017.

Niemeier, U., C. Timmreck, H.-F. Graf, S. Kinne, S. Rast, and S. Self, 2009: Initial fate of fine ash and sulfur from large volcanic eruptions. *Atmos. Chem. Phys.*, **9 (22)**, 9043–9057. doi:10.5194/acp-9-9043-2009.

Noppel, M., H. Vehkamäki, and M. Kulmala, 2002: An improved model for hydrate formation in sulfuric acid–water nucleation. *J. Chem. Phys.*, **116 (1)**, 218–228. doi:10.1063/1.1423333.

Osores, S., J. Ruiz, A. Folch, and E. Collini, 2020: Volcanic ash forecast using ensemble-based data assimilation: an ensemble transform Kalman filter coupled with the FALL3D-7.2 model (ETKF–FALL3D version 1.0). *Geosci. Model Dev.*, **13 (1)**, 1–22. doi:10.5194/gmd-13-1-2020.

Oxford Economics, 2010: The Economic Impacts of Air Travel Restrictions Due to Volcanic Ash. Tech. rep., Oxford Economics, URL `https://www.oxfordeconomics.com/my-oxford/projects/129051`, last access: 29 September 2021.

O'Dowd, C., D. Ceburnis, J. Ovadnevaite, G. Martucci, J. Bialek, C. Monahan, H. Berresheim, A. Vaishya, T. Grigas, S. G. Jennings, P. McVeigh, S. Varghese, R. Flanagan, D. Martin, E. Moran, K. Lambkin, T. Semmler, C. Perrino, and R. McGrath, 2012: The Eyjafjallajökull ash plume – Part I: Physical, chemical and optical characteristics. *Atmos. Environ.*, **48**, 129–142. doi:https://doi.org/10.1016/j.atmosenv.2011.07.004.

Palacios-Peña, L., P. Stier, R. Lorente-Plazas, and P. Jiménez-Guerrero, 2020: Quantifying the sensitivity of aerosol optical properties to the parameterizations of physico-chemical processes during the 2010 Russian wildfires and heatwave. *Atmos. Chem. Phys.*, **20 (16)**, 9679–9700. doi:10.5194/acp-20-9679-2020.

Pardini, F., S. Corradini, A. Costa, T. Esposti Ongaro, L. Merucci, A. Neri, D. Stelitano, and M. de' Michieli Vitturi, 2020: Ensemble-Based Data Assimilation of Volcanic Ash Clouds from Satellite Observations: Application to the 24 December 2018 Mt. Etna Explosive Eruption. *Atmosphere-Basel*, **11 (4)**, 359. doi:10.3390/atmos11040359.

Pardini, F., A. Spanu, M. de' Michieli Vitturi, M. V. Salvetti, and A. Neri, 2016: Grain size distribution uncertainty quantification in volcanic ash dispersal and deposition from weak plumes. *J. Geophys. Res.-Sol. Ea.*, **121 (2)**, 538–557. doi:https://doi.org/10.1002/2015JB012536.

Perrotta, A. and C. Scarpati, 2003: Volume partition between the plinian and co-ignimbrite air fall deposits of the Campanian Ignimbrite eruption. *Miner. Petrol.*, **79**, 67–78. doi:https://doi.org/10.1007/s00710-003-0002-8.

Peterson, P. K., D. Pöhler, H. Sihler, J. Zielcke, S. General, U. Frieß, U. Platt, W. R. Simpson, S. V. Nghiem, P. B. Shepson, B. H. Stirm, S. Dhaniyala, T. Wagner, D. R. Caulton, J. D. Fuentes, and K. A. Pratt, 2017: Observations of bromine monoxide transport in the arctic sustained on aerosol particles. *Atmos. Chem. Phys.*, **17 (12)**, 7567–7579. doi:10.5194/acp-17-7567-2017.

Petty, G., 2006: *A First Course in Atmospheric Radiation*. Sundog Pub., Madison, Wisconsin, 452 pp.

Pisso, I., E. Sollum, H. Grythe, N. I. Kristiansen, M. Cassiani, S. Eckhardt, D. Arnold, D. Morton, R. L. Thompson, C. D. Groot Zwaaftink, N. Evangeliou, H. Sodemann, L. Haimberger, S. Henne, D. Brunner, J. F. Burkhart, A. Fouilloux, J. Brioude, A. Philipp, P. Seibert, and A. Stohl, 2019: The Lagrangian particle dispersion model FLEXPART version 10.4. *Geosci. Model Dev.*, **12 (12)**, 4955–4997. doi:10.5194/gmd-12-4955-2019.

Pitari, G., G. Di Genova, E. Mancini, D. Visioni, I. Gandolfi, and I. Cionni, 2016: Stratospheric Aerosols from Major Volcanic Eruptions: A Composition-Climate Model Study of the Aerosol Cloud Dispersal and e-folding Time. *Atmosphere–Basel*, **7 (6)**. doi:10.3390/atmos7060075.

Plu, M., G. Bigeard, B. Sič, E. Emili, L. Bugliaro, L. El Amraoui, J. Guth, B. Josse, L. Mona, and D. Piontek, 2021: Modelling the volcanic ash plume from Eyjafjallajökull eruption (May 2010) over Europe: evaluation of the benefit of source term improvements and of the assimilation of aerosol measurements. *Natural Hazards and Earth System Sciences Discussions*, **2021**, 1–24. doi:10.5194/nhess-2021-97.

Polavarapu, S., S. Ren, A. M. Clayton, D. Sankey, and Y. Rochon, 2004: On the Relationship between Incremental Analysis Updating and Incremental Digital Filtering. *Mon. Weather Rev.*, **132 (10)**, 2495 – 2502. doi:10.1175/1520-0493(2004)132<2495:OTRBIA>2.0.CO;2.

Prata, A., 1989: Infrared radiative transfer calculations for volcanic ash clouds. *Geophys. Res. Lett.*, **16 (11)**, 1293–1296. doi:https://doi.org/10.1029/GL016i011p01293.

Prata, A. and A. Prata, 2012: Eyjafjallajökull volcanic ash concentrations determined using spin enhanced visible and infrared imager measurements. *J. Geophys. Res.-Atmos.*, **117 (D6)**. doi:https://doi.org/10.1029/2011JD016800.

Prata, A., W. Rose, S. Self, and D. O'Brien, 2004: Global, long-term sulphur dioxide measurements from tovs data: A new tool for studying explosive volcanism and climate. *Volcanism and the Earth's Atmosphere*, American Geophysical Union (AGU), 75–92. doi:https://doi.org/10.1029/139GM05.

Prata, A. T., H. F. Dacre, E. A. Irvine, E. Mathieu, K. P. Shine, and R. J. Clarkson, 2019: Calculating and communicating ensemble-based volcanic ash dosage and concentration risk for aviation. *Meteorol. Appl.*, **26 (2)**, 253–266. doi:10.1002/met.1759.

Prata, F., G. Bluth, B. Rose, D. Schneider, and A. Tupper, 2001: Comments on "Failures in detecting volcanic ash from a satellite-based technique". *Remote Sens. Environ.*, **78 (3)**, 341–346. doi:https://doi.org/10.1016/S0034-4257(01)00231-0.

Prata, F. and M. Lynch, 2019: Passive Earth Observations of Volcanic Clouds in the Atmosphere. *Atmosphere–Basel*, **10 (4)**. doi:10.3390/atmos10040199.

Prather, M. J., 2015: Photolysis rates in correlated overlapping cloud fields: Cloud-J 7.3c. *Geosci. Model Dev.*, **8 (8)**, 2587–2595. doi:10.5194/gmd-8-2587-2015.

Pratsinis, S. E., 1988: Simultaneous nucleation, condensation, and coagulation in aerosol reactors. *J. Colloid Interf. Sci.*, **124 (2)**, 416–427. doi:https://doi.org/10.1016/0021-9797(88)90180-4.

Pruppacher, H. and J. Klett, 2010: *Microphysics of Clouds and Precipitation*. Springer, Dordrecht, 954 pp.

Raes, F., R. Van Dingenen, E. Vignati, J. Wilson, J.-P. Putaud, J. H. Seinfeld, and P. Adams, 2000: Formation and cycling of aerosols in the global troposphere. *Atmos. Environ.*, **34 (25)**, 4215–4240. doi:https://doi.org/10.1016/S1352-2310(00)00239-9.

Randall, D., R. Wood, S. Bony, R. Colman, T. Fichefet, J. Fyfe, V. Kattsov, A. Pitman, J. Shukla, J. Srinivasan, R. Stouffer, A. Sumi, and K. Taylor, 2007: Cilmate models and their evaluation. *Climate Change 2007: The Physical Science Basis. Contribution of Working Group I to the Fourth Assessment Report of the Intergovernmental Panel on Climate Change*, Solomon, S., D. Qin, M. Manning, Z. Chen, M. Marquis, K. Averyt, M. Tignor, and H. Miller, Eds., Cambridge University Press, Cambridge, UK and New York, NY, USA, 590–662. doi:10.1017/CBO9781107415324.016.

Rieger, D., 2017: Der Einfluss von natürlichem Aerosol auf Wolken über Mitteleuropa. Ph.D. thesis, Karlsruher Institut für Technologie (KIT). doi:10.5445/IR/1000061642.

Rieger, D., M. Bangert, I. Bischoff-Gauss, J. Förstner, K. Lundgren, D. Reinert, J. Schröter, H. Vogel, G. Zängl, R. Ruhnke, and B. Vogel, 2015: ICON–ART 1.0 – a new online-coupled model system from the global to regional scale. *Geosci. Model Dev.*, **8 (6)**, 1659–1676. doi:10.5194/gmd-8-1659-2015.

Rieger, L. A., E. P. Malinina, A. V. Rozanov, J. P. Burrows, A. E. Bourassa, and D. A. Degenstein, 2018: A study of the approaches used to retrieve aerosol extinction, as applied to limb observations made by OSIRIS and SCIAMACHY. *Atmos. Meas. Tech. Discussions*, **2018**, 1–21. doi:10.5194/amt-2017-446.

Riemer, N., 2002: Numerische Simulationen zur Wirkung des Aerosols auf die troposphärische Chemie und die Sichtweite. Ph.D. thesis, Universität Karlsruhe (TH). doi:10.5445/IR/2212002.

Roberts, N., 2008: Assessing the spatial and temporal variation in the skill of precipitation forecasts from an NWP model. *Meteorol. Appl.*, **15 (1)**, 163–169. doi:https://doi.org/10.1002/met.57.

Roberts, N. M. and H. W. Lean, 2008: Scale-Selective Verification of Rainfall Accumulations from High-Resolution Forecasts of Convective Events. *Mon. Weather Rev.*, **136 (1)**, 78 – 97. doi:10.1175/2007MWR2123.1.

Robock, A., 2000: Volcanic eruptions and climate. *Rev. Geophys.*, **38 (2)**, 191–219. doi:10.1029/1998RG000054.

Rose, W. and A. Durant, 2009: Fine ash content of explosive eruptions. *J. Volcanol. Geoth. Res.*, **186 (1)**, 32 – 39. doi:https://doi.org/10.1016/j.jvolgeores.2009.01.010.

Rosen, J. M., 1971: The boiling point of stratospheric aerosols. *J. Appl. Meteorol. Clim.*, **10 (5)**, 1044 – 1046. doi:10.1175/1520-0450(1971)010<1044:TBPOSA>2.0.CO;2.

Schmehl, K. J., S. E. Haupt, and M. Pavolonis, 2011: A genetic algorithm variational approach to data assimilation and application to volcanic emissions. *Pure Appl. Geophys.*, **169**, 519–537. doi:https://doi.org/10.1007/s00024-011-0385-0.

Schmidt, A., C. S. Witham, N. Theys, N. A. D. Richards, T. Thordarson, K. Szpek, W. Feng, M. C. Hort, A. M. Woolley, A. R. Jones, A. L. Redington, B. T. Johnson, C. L. Hayward, and K. S. Carslaw, 2014: Assessing hazards to aviation from sulfur dioxide emitted by explosive icelandic eruptions. *J. Geophys. Res.-Atmos.*, **119 (24)**, 14,180–14,196. doi:10.1002/2014jd022070.

Schmincke, H.-U., 2004: *Volcanism*. Springer-Verlag Berlin Heidelberg, 324 pp.

Schröter, J., D. Rieger, C. Stassen, H. Vogel, M. Weimer, S. Werchner, J. Förstner, F. Prill, D. Reinert, G. Zängl, M. Giorgetta, R. Ruhnke, B. Vogel, and P. Braesicke, 2018: ICON-ART 2.1: a flexible tracer framework and its application for composition studies in numerical weather forecasting and climate simulations. *Geosci. Model Dev.*, **11 (10)**, 4043–4068. doi:10.5194/gmd-11-4043-2018.

Schumann, U., B. Weinzierl, O. Reitebuch, H. Schlager, A. Minikin, C. Forster, R. Baumann, T. Sailer, K. Graf, H. Mannstein, C. Voigt, S. Rahm, R. Simmet, M. Scheibe, M. Lichtenstern, P. Stock, H. Rüba, D. Schäuble, A. Tafferner, M. Rautenhaus, T. Gerz, H. Ziereis, M. Krautstrunk, C. Mallaun, J.-F. Gayet, K. Lieke, K. Kandler, M. Ebert, S. Weinbruch, A. Stohl, J. Gasteiger, S. Groß, V. Freudenthaler, M. Wiegner, A. Ansmann, M. Tesche, H. Olafsson, and K. Sturm, 2011: Airborne observations of the Eyjafjalla volcano ash cloud over Europe during air space closure in April and May 2010. *Atmos. Chem. Phys.*, **11 (5)**, 2245–2279. doi:10.5194/acp-11-2245-2011.

Sears, T. M., G. E. Thomas, E. Carboni, A. J. A. Smith, and R. G. Grainger, 2013: SO_2 as a possible proxy for volcanic ash in aviation hazard avoidance. *J. Geophys. Res.-Atmos.*, **118 (11)**, 5698–5709. doi:https://doi.org/10.1002/jgrd.50505.

Seinfeld, J. H. and S. N. Pandis, 2016: *Atmospheric Chemistry and Physics*. Wiley John + Sons, Inc., Hoboken, New Jersey, 1152 pp.

Sennert, S., 2019: Global Volcanism Program, 2019, Report on Raikoke (Russia), Weekly Volcanic Activity Report, 26 June-2 July 2019. Tech. rep., Smithsonian Institution and US Geological Survey., URL `https://volcano.si.edu/showreport.cfm?doi=GVP.WVAR20190619-290250`, last access: 03 December 2021.

Simonin, D., C. Pierce, N. Roberts, S. P. Ballard, and Z. Li, 2017: Performance of Met Office hourly cycling NWP-based nowcasting for precipitation forecasts. *Q. J. Roy. Meteor. Soc.*, **143 (708)**, 2862–2873. doi:https://doi.org/10.1002/qj.3136.

Sič, B., L. El Amraoui, V. Marécal, B. Josse, J. Arteta, J. Guth, M. Joly, and P. D. Hamer, 2015: Modelling of primary aerosols in the chemical transport model MOCAGE: development and evaluation of aerosol physical parameterizations. *Geosci. Model Dev.*, **8 (2)**, 381–408. doi:10.5194/gmd-8-381-2015.

Skamarock, W. C., J. B. Klemp, J. Dudhia, D. O. Gill, D. Barker, M. G. Duda, X.-Y. Huang, W. Wang, and J. G. Powers, 2008: A Description of the Advanced Research WRF Version 3. Tech. rep., University Corporation for Atmospheric Research, URL `http://opensky.ucar.edu/islandora/object/technotes:500`, last access: 03 December 2021.

Skok, G. and N. Roberts, 2016: Analysis of Fractions Skill Score properties for random precipitation fields and ECMWF forecasts. *Q. J. Roy. Meteor. Soc.*, **142 (700)**, 2599–2610. doi:https://doi.org/10.1002/qj.2849.

Smoluchowski, M., 1927: Drei Vorträge über Diffusion, Brownsche Molekularbewegung und Koagulation von Kolloidteilchen. *Pisma Mariana Smoluchowskiego*, **2 (1)**, 530–594. URL `http://eudml.org/doc/215805`.

Stein, A. F., R. R. Draxler, G. D. Rolph, B. J. B. Stunder, M. D. Cohen, and F. Ngan, 2015: NOAA's HYSPLIT Atmospheric Transport and Dispersion Modeling System. *B. Am. Meteorol. Soc.*, **96 (12)**, 2059 – 2077. doi:10.1175/BAMS-D-14-00110.1.

Steinke, I., O. Möhler, A. Kiselev, M. Niemand, H. Saathoff, M. Schnaiter, J. Skrotzki, C. Hoose, and T. Leisner, 2011: Ice nucleation properties of fine ash particles from the Eyjafjallajökull eruption in April 2010. *Atmos. Chem. Phys.*, **11 (24)**, 12 945–12 958. doi:10.5194/acp-11-12945-2011.

Stevenson, J. A., S. C. Millington, F. M. Beckett, G. T. Swindles, and T. Thordarson, 2015: Big grains go far: understanding the discrepancy between tephrochronology and satellite infrared measurements of volcanic ash. *Atmos. Meas. Tech.*, **8 (5)**, 2069–2091. doi:10.5194/amt-8-2069-2015.

Stewart, L. M., S. L. Dance, and N. K. Nichols, 2013: Data assimilation with correlated observation errors: experiments with a 1-d shallow water model. *Tellus A*, **65 (1)**, 19 546. doi:10.3402/tellusa.v65i0.19546.

Stockwell, W. R. and J. G. Calvert, 1983: The mechanism of the HO-SO2 reaction. *Atmos. Environ.*, **17 (11)**, 2231 – 2235. doi:https://doi.org/10.1016/0004-6981(83)90220-2.

Stohl, A., M. Hittenberger, and G. Wotawa, 1998: Validation of the lagrangian particle dispersion model FLEXPART against large-scale tracer experiment data. *Atmos. Environ.*, **32 (24)**, 4245–4264. doi:https://doi.org/10.1016/S1352-2310(98)00184-8.

Tabazadeh, a. and R. P. Turco, 1993: Stratospheric Chlorine Injection by Volcanic Eruptions: HCI Scavenging and Implications for Ozone. *Science*, **260 (5111)**, 1082–6. doi:10.1126/science.260.5111.1082.

Tarcea, N., 2004: Light as a universal tool : Microcapsule sizing by elastic light scattering and mineral investigation by in situ Raman spectroscopy. Ph.D. thesis, Universität Würzburg. URL `https://opus.bibliothek.uni-wuerzburg.de/opus4-wuerzburg/frontdoor/deliver/index/docId/806/file/Dissertation_NicolaeTarcea.pdf`.

Textor, C., H. F. Graf, M. Herzog, J. M. Oberhuber, W. I. Rose, and G. G. Ernst, 2006a: Volcanic particle aggregation in explosive eruption columns. Part I: Parameterization of the microphysics of hydrometeors and ash. *J. Volcanol. Geoth. Res.*, **150 (4)**, 359–377. doi:https://doi.org/10.1016/j.jvolgeores.2005.09.007.

Textor, C., H. F. Graf, M. Herzog, J. M. Oberhuber, W. I. Rose, and G. G. J. Ernst, 2006b: Volcanic particle aggregation in explosive eruption columns. Part II: Numerical experiments. *J. Volcanol. Geoth. Res.*, **150 (4)**, 378–394. doi:10.1016/j.jvolgeores.2005.09.008.

Textor, C., H.-F. Graf, C. Timmreck, and A. Robock, 2004: Emissions from volcanoes. *Emissions of Atmospheric Trace Compounds*, Granier, C., P. Artaxo, and C. E. Reeves, Eds., Springer Netherlands, Dordrecht, 269–303. doi:10.1007/978-1-4020-2167-1_7.

Theys, N., I. De Smedt, H. Yu, T. Danckaert, J. van Gent, C. Hörmann, T. Wagner, P. Hedelt, H. Bauer, F. Romahn, M. Pedergnana, D. Loyola, and M. Van Roozendael, 2017: Sulfur dioxide retrievals from TROPOMI onboard Sentinel-5 Precursor: algorithm theoretical basis. *Atmos. Meas. Tech.*, **10 (1)**, 119–153. doi:10.5194/amt-10-119-2017.

Theys, N., P. Hedelt, I. De Smedt, C. Lerot, H. Yu, J. Vlietinck, M. Pedergnana, S. Arellano, B. Galle, D. Fernandez, C. Carlito, C. Barrington, B. Taisne, H. Delgado Granados, D. Loyola, and

M. Van Roozendael, 2019: Global monitoring of volcanic SO2 degassing with unprecedented resolution from TROPOMI onboard Sentinel-5 Precursor. *Sci. Rep.-UK*, **9**. doi:10.1038/s41598-019-39279-y.

Timmreck, C., 2012: Modeling the climatic effects of large explosive volcanic eruptions. *Wires. Clim. Change*, **3 (6)**, 545–564. doi:https://doi.org/10.1002/wcc.192.

Toon, O. B. and T. P. Ackerman, 1981: Algorithms for the calculation of scattering by stratified spheres. *Appl. Optics*, **20 (20)**, 3657–3660. doi:10.1364/AO.20.003657.

Twomey, S., 1974: Pollution and the planetary albedo. *Atmos. Environ.*, **8 (12)**, 1251–1256. doi:https://doi.org/10.1016/0004-6981(74)90004-3.

Van Eaton, A. R., L. G. Mastin, M. Herzog, H. F. Schwaiger, D. J. Schneider, K. L. Wallace, and A. B. Clarke, 2015: Hail formation triggers rapid ash aggregation in volcanic plumes. *Nat. Commun.*, **6 (August)**, 1–7. doi:10.1038/ncomms8860.

van Kempen, T. A., R. M. van Hees, P. J. J. Tol, I. Aben, and R. W. M. Hoogeveen, 2019: In-flight calibration and monitoring of the Tropospheric Monitoring Instrument (TROPOMI) short-wave infrared (SWIR) module. *Atmos. Meas. Tech.*, **12 (12)**, 6827–6844. doi:10.5194/amt-12-6827-2019.

Vaughan, M. A., S. A. Young, D. M. Winker, K. A. Powell, A. H. Omar, Z. Liu, Y. Hu, and C. A. Hostetler, 2004: Fully automated analysis of space-based lidar data: an overview of the CALIPSO retrieval algorithms and data products. *Laser Radar Techniques for Atmospheric Sensing*, Singh, U. N., Ed., International Society for Optics and Photonics, SPIE, Vol. 5575, 16 – 30. doi:10.1117/12.572024.

Vernier, J.-P., T. D. Fairlie, T. Deshler, M. Natarajan, T. Knepp, K. Foster, F. G. Wienhold, K. M. Bedka, L. Thomason, and C. Trepte, 2016: In situ and space-based observations of the Kelud volcanic plume: The persistence of ash in the lower stratosphere. *J. Geophys. Res.-Atmos.*, **121 (18)**, 11,104–11,118. doi:10.1002/2016JD025344.

Vogel, A., S. Diplas, A. J. Durant, A. S. Azar, M. F. Sunding, W. I. Rose, A. Sytchkova, C. Bonadonna, K. Krüger, and A. Stohl, 2017: Reference data set of volcanic ash physicochemical and optical properties. *J. Geophys. Res.-Atmos.* doi:https://doi.org/10.1002/2016JD026328.

von Savigny, C., C. Timmreck, S. Buehler, J. Burrows, M. Giorgetta, G. Hegerl, A. Horvath, G. A. Hoshyaripour, C. Hoose, J. Quaas, E. Malinina, A. Rozanov, H. Schmidt, L. Thomason, M. Toohey, and B. Vogel, 2020: The Research Unit VolImpact: Revisiting the volcanic impact on atmosphere and climate – preparations for the next big volcanic eruption. *Meteorol. Z.*, **29 (1)**, 3–18. doi:10.1127/metz/2019/0999.

Walter, C., 2019: Simulationen der Ausbreitung von Vulkanasche unter expliziter Berücksichtigung der optischen Eigenschaften der Aschepartikel. Ph.D. thesis, Karlsruher Institut für Technologie (KIT). doi:10.5445/KSP/1000095717.

Weimer, M., J. Schröter, J. Eckstein, K. Deetz, M. Neumaier, G. Fischbeck, L. Hu, D. B. Millet, D. Rieger, H. Vogel, B. Vogel, T. Reddmann, O. Kirner, R. Ruhnke, and P. Braesicke, 2017: An emission module for ICON-ART 2.0: implementation and simulations of acetone. *Geosci. Model Dev.*, **10 (6)**, 2471–2494. doi:10.5194/gmd-10-2471-2017.

Weingartner, E., H. Burtscher, and U. Baltensperger, 1997: Hygroscopic properties of carbon and diesel soot particles. *Atmos. Environ.*, **31 (15)**, 2311 – 2327. doi:https://doi.org/10.1016/S1352-2310(97)00023-X.

Wen, S. and W. I. Rose, 1994: Retrieval of sizes and total masses of particles in volcanic clouds using avhrr bands 4 and 5. *J. Geophys. Res.-Atmos.*, **99 (D3)**, 5421–5431. doi:https://doi.org/10.1029/93JD03340.

Wernli, H., C. Hofmann, and M. Zimmer, 2009: Spatial Forecast Verification Methods Intercomparison Project: Application of the SAL Technique. *Weather Forecast.*, **24 (6)**, 1472–1484. doi:10.1175/2009WAF2222271.1.

Wernli, H., M. Paulat, M. Hagen, and C. Frei, 2008: SAL – A Novel Quality Measure for the Verification of Quantitative Precipitation Forecasts. *Mon. Weather Rev.*, **136 (11)**, 4470–4487. doi:10.1175/2008MWR2415.1.

Western, L. M., M. I. Watson, and P. N. Francis, 2015: Uncertainty in two-channel infrared remote sensing retrievals of a well-characterised volcanic ash cloud. *B. Volcanol.*, **77 (8)**, 67. URL `https://doi.org/10.1007/s00445-015-0950-y`.

Whitby, E. R., P. H. McMurry, U. Shankar, and F. S. Binkowski, 1991: Modal aerosol dynamics modeling. Tech. rep., EPA report for contract no. 68-01-7365, URL `https://nepis.epa.gov/Exe/ZyNET.exe/9100JZV8.TXT?ZyActionD=ZyDocument&Client=EPA&Index=1991+Thru+1994&Docs=&Query=&Time=&EndTime=&SearchMethod=1&TocRestrict=n&Toc=&TocEntry=&QField=&QFieldYear=&QFieldMonth=&QFieldDay=&IntQFieldOp=0&ExtQFieldOp=0&XmlQuery=&File=D%3A%5Czyfiles%5CIndex%20Data%5C91thru94%5CTxt%5C00000024%5C9100JZV8.txt&User=ANONYMOUS&Password=anonymous&SortMethod=h%7C-&MaximumDocuments=1&FuzzyDegree=0&ImageQuality=r75g8/r75g8/x150y150g16/i425&Display=hpfr&DefSeekPage=x&SearchBack=ZyActionL&Back=ZyActionS&BackDesc=Results%20page&MaximumPages=1&ZyEntry=1&SeekPage=x&ZyPURL`, last access: 03 December 2021.

Whitby, K. T., 1978: The physical characteristics of sulfur aerosols. *Atmos. Environ.*, **12 (1)**, 135–159. doi:https://doi.org/10.1016/0004-6981(78)90196-8.

Wilkins, K., S. Mackie, M. Watson, H. Webster, D. Thomson, and H. Dacre, 2015: Data insertion in volcanic ash cloud forecasting. *Ann. Geophys.-Italy*, **57 (0)**. doi:10.4401/ag-6624.

Wilkins, K. L., I. M. Watson, N. I. Kristiansen, H. N. Webster, D. J. Thomson, H. F. Dacre, and A. J. Prata, 2016: Using data insertion with the NAME model to simulate the 8 May 2010 Eyjafjallajökull volcanic ash cloud. *J. Geophys. Res.-Atmos.*, **121 (1)**, 306–323. doi:https://doi.org/10.1002/2015JD023895.

Wilson, L. and T. Huang, 1979: The influence of shape on the atmospheric settling velocity of volcanic ash particles. *Earth Planet. Sc. Lett.*, **44 (2)**, 311–324. doi:https://doi.org/10.1016/0012-821X(79)90179-1.

Yu, P., O. B. Toon, C. G. Bardeen, Y. Zhu, K. H. Rosenlof, R. W. Portmann, T. D. Thornberry, R.-S. Gao, S. M. Davis, E. T. Wolf, J. de Gouw, D. A. Peterson, M. D. Fromm, and A. Robock, 2019: Black carbon lofts wildfire smoke high into the stratosphere to form a persistent plume. *Science*, **365 (6453)**, 587–590. doi:10.1126/science.aax1748.

Zhu, Y., O. B. Toon, E. J. Jensen, C. G. Bardeen, M. J. Mills, M. A. Tolbert, P. Yu, and S. Woods, 2020: Persisting volcanic ash particles impact stratospheric SO_2 lifetime and aerosol optical properties. *Nat. Commun.*, **11 (1)**. doi:10.1038/s41467-020-18352-5.

Zängl, G., D. Reinert, P. Rípodas, and M. Baldauf, 2015: The ICON (ICOsahedral Non-hydrostatic) modelling framework of DWD and MPI-M: Description of the non-hydrostatic dynamical core. *Q. J. Roy. Meteor. Soc.*, **141 (687)**, 563–579. doi:10.1002/qj.2378.

F. List of Figures

G. List of Tables

Danksagung

Diese Arbeit wurde durch das Bundesministerium für Digitales und Verkehr (BMVI) gefördert (Fördernummer: FE-Nr. 50.0368/2017).

Diese Arbeit wäre nicht möglich gewesen ohne die großartige Unterstützung meiner Betreuer, Kolleg*innen, Freund*innen und Familie über die vergangenen Jahre. Die fachlichen Diskussionen, die konstruktiven Kritiken, die aufmunternden Worte, die interessierten Nachfragen und die zerstreuenden Freizeitaktivitäten haben die Dissertation immer vorangebracht und mir Durchhaltevermögen und Rückhalt gegeben.

Für die Betreuung sowie die Begutachtung der Arbeit möchte ich mich herzlich bei Prof. Christoph Kottmeier bedanken. Ihre konstruktiven Anmerkungen, Anregungen und Ratschläge waren mir immer eine wichtige Orientierung.

Besonderer Dank gilt auch Prof. Roland Potthast für die Übernahme des Korreferats sowie die intensive Betreuung in allen Belangen der Datenassimilation. Deine ausführlichen Erklärungen und vielzähligen Beispielskripte haben den Einbau der En-Var Assimilation in meine Arbeit erst möglich gemacht. Deine fachliche Kompetenz und dein ansteckender Enthusiasmus werden mir immer als Vorbild dienen.

Ein besonders großer Dank geht an Dr. Bernhard Vogel, der mir von Beginn an das nötige Vertrauen entgegenbrachte, mir die Freiheiten ließ meinen eigenen Weg zu gehen, die Richtung wies, wenn ich nicht weiter wusste, und für wissenschaftliche Diskussionen oder Ratschläge jederzeit zur Verfügung stand. Die Zeit in deiner Arbeitsgruppe war sehr lehrreich und ich fand es immer sehr bereichernd, dass es dir ein Anliegen war, dass wir auch über unseren Tellerrand blicken. Vielen Dank lieber Bernhard für jegliche Unterstützung während der vergangenen Jahre und im Besonderen während der letzten Monate.

Natürlich wäre die Arbeit nicht in diesem Maße erfolgreich gewesen ohne die vielfältige Unterstützung durch Kolleginnen und Kollegen. Hier gilt mein Dank im besonderen Dr. Heike Vogel für jegliche Hilfe mit den Eigenheiten und Tücken ICON-ARTs sowie für deine pragmatischen Lösungsansätze für Probleme aller Art. Ebenso danke ich Dr. Ali Hoshyaripour für die großartige Unterstützung nicht nur zu meiner ersten Publikation sondern auch in allen anderen wissenschaftlichen Belangen, für die unzähligen Gespräche über Vulkanausbrüche und -asche sowie deine herzliche und offene Art. Ich habe sehr viel von dir über vulkanische Aerosole und deren Strahlungswechselwirkung gelernt und im Zweifel konntest du mich immer an das richtige Paper verweisen. Der gesamten Arbeitsgruppe *Spurenstoffmodellierung und Klimaprozesse* danke ich für die angenehme Atmosphäre, die wissenschaftlichen Diskussionen, das Anhören von Probevorträgen, die produktiven Hackathons und den guten Zusammenhalt in der Gruppe. Es ist mir immer eine Freude mit euch zusammen zu arbeiten. Im besonderen möchte ich dir, liebe Ani-

ka, danken, für deine Hilfsbereitschaft, deine Unterstützung in allen Belangen und dass du immer ein offenes Ohr hattest. Du warst eine große Konstante während der gesamten Dauer meiner Promotion, ich bin sehr froh, dich als Kollegin zu haben und hoffe auch in Zukunft so freundschaftlich mit dir verbunden zu bleiben. Vanessa Bachmann, dir bin ich sehr für die angenehme Zusammenarbeit bei der Entwicklung der Datenassimilationsroutine sowie für deine Unterstützung bei der Einarbeitung in bacy und datools dankbar. Deine eigene Arbeit, auf welche ich aufbauen konnte, sowie der gegenseitige Austausch haben meinen Fortschritt sehr beschleunigt. Gabi Klinck möchte ich für die stete Hilfe bei IT-Fragen, die Pflege meiner Büropflanze und die aufmunternden Worte danken, wann immer der Arbeitstag mal etwas länger dauerte als geplant.

Ein großer Dank gilt der gesamten ICON(-ART) community innerhalb der IMKs, am SCC, beim DWD, am DKRZ und MPI-M sowie im Speziellen Sven Werchner, für deinen unermüdlichen Einsatz unseren Code fehlerfrei und lauffähig zu halten. Meine technischen Weiterentwicklungen in ICON-ART wären ohne diese Unterstützung sowie den Austausch über Fehler im Modell und deren Behebung nicht möglich gewesen.

Ich möchte mich herzlich bei allen aktuellen und ehemaligen Mitarbeitenden der IMKs bedanken, welche mich beruflich, aber auch privat begleitet haben. Die Arbeitsatmosphäre war immer sehr angenehm und der persönliche Austausch, auch über die Departementsgrenzen hinweg, bedeutet mir viel. Ein besonderer Dank gilt hierbei Alberto, Sebastian, Philipp, Shweta, Dominik, Marleen, Amelie, Karmen, Moritz, Sera, Simone, Nicole, Marlon und den Turmbergschnecken für die vorpandemischen Mittags- und Kaffeepausen, unvergessliche Seminar- und Konferenzbesuche, Feierabendsport und Wochenendunternehmungen.

Ein fettes Dankeschön gilt den unermüdlichen Korrekturleser*innen Alberto, Anika, Doro, Julia, Kerstin, Marleen und Philipp, welche mich während der intensiven finalen Schreibphase tatkräftig unterstützt haben.

Die Kombination aus Pandemie und Endphase der Doktorarbeit hatte die sozialen Kontakte während der vergangenen zwei Jahre für mich drastisch reduziert. Umso dankbarer bin ich für alle Freund*innen, die mich trotz der Umstände und der teilweise recht großen räumlichen Distanz unterstützt haben und nach wie vor zu mir halten. Ein großes Dankeschön gebührt außerdem meinem lieben Mitbewohner, dank dem die diversen Ausgangssperren erträglich wurden und dadurch die Arbeitsmoral nie zu tief sank.

Der größte Dank gilt meiner Familie. Ihr wart mir immer ein große Stütze, habt mir Rückhalt gegeben, an mich geglaubt und gezeigt, dass es auch wichtigere Dinge im Leben gibt als die Arbeit.